

**MULTI-DEGREE OF FREEDOM POSITION SENSOR
FOR PLANAR MOTORS**

by

Keir Maguire

B.A.Sc., The University of British Columbia, 2012

A THESIS SUBMITTED IN PARTIAL FULFILLMENT OF
THE REQUIREMENTS FOR THE DEGREE OF

MASTER OF APPLIED SCIENCE

in

THE FACULTY OF GRADUATE AND POSTDOCTORAL STUDIES
(Mechanical Engineering)

THE UNIVERSITY OF BRITISH COLUMBIA

(Vancouver)

August 2015

© Keir Maguire, 2015

Abstract

This thesis presents the development and verification of a multi-degree of freedom (DOF), non-contact position sensor for a magnetically levitated planar motor. Planar motors are intended to replace X-Y stages in various manufacturing processes resulting in higher accuracy, higher speed, and no friction. To obtain position feedback, previous planar motors have used laser interferometers, planar encoders, stereo vision, capacitive sensors, and Hall sensor arrays. For applications requiring micrometre-level precision, Hall sensor arrays are cost-effective, absolute, high bandwidth, can be integrated into the stator, and are capable of sensing multiple movers in 6-DOF over large stroke and rotation. However, previous Hall sensor arrays suffered from excessive error, low bandwidth, absolute position only within one pitch of the magnet array, modifications to the mover, lack of 6-DOF or multi-mover capability, or limited range.

A 2-D Hall sensor array was developed. There are three sensors per wavelength of the magnetic field, which decouples sensor outputs for orthogonal 1-D Halbach magnet arrays. The position in 2-DOF, X and Z, is calculated for a 1-D Halbach array. The position in 6-DOF can be calculated for a planar motor mover composed of four orthogonal Halbach arrays. This sensor solution measures absolute position and is high bandwidth, multi-mover capable, and scalable with stroke.

A prototype was designed, consisting of a Hall sensor array, summing amplifiers, and signal processing electronics. The prototype was tested in 2-DOF using a CNC to move a Halbach array to discrete points. Position error is approximately 200 μm peak to peak; however, the error is

periodic and can be compensated. Resolution is 5 μm . Due to redundancy and averaging, improved accuracy and resolution is expected for 6-DOF sensing of the planar motor.

Variation in sensor gain is a common cause of error in previous Hall sensor arrays. Previous Hall sensor arrays have only achieved good accuracy by using laser interferometers for error mapping or individual differential amplifiers to control each sensor's gain. A sensor sorting setup was designed, built, and used to sort more than 12,000 sensors based on gain. The sorted sensors can be used for a sensor array with micrometre-level accuracy.

Preface

The principle of the sensor solution (Chapter 2) was developed by Dr. Xiaodong Lu, with help from Rui Chen on algorithm development. The Hall sensor array and summing circuit in the PCB prototype (Chapter 3) were designed by Dr. Lu and myself, the supporting electronics and FPGA logic were designed by Dr. Lu, and the FPGA PCB was designed by Eric Buckley. The experiment set up, execution, and analysis (Chapter 4) were carried out by myself with guidance from Dr. Lu and Irfan-ur-rab Usman. The sensor sorting system (Chapter 5) was envisioned by Dr. Lu and designed by myself under his guidance. Mark Dyck suggested the final kinematic coupling geometry. The 12,700 sorted sensors were sorted by Jian Gao and myself.

Table of Contents

Abstract.....	ii
Preface.....	iv
Table of Contents	v
List of Tables	viii
List of Figures.....	ix
List of Abbreviations	xiii
Acknowledgements	xiv
Dedication	xvi
Chapter 1: Introduction	1
1.1 Planar Motor	1
1.2 Sensor Requirements	3
1.3 Existing Metrology Solutions	7
1.3.1 Laser Interferometry	7
1.3.2 Surface Encoder	8
1.3.3 Capacitive Sensor.....	9
1.3.4 Stereo Vision.....	10
1.3.5 Hall Sensor Array	12
1.3.5.1 4-DOF Hall Sensor Array with Filtering of 1 st Spatial Harmonic	13
1.3.5.2 3-DOF Sensor Using 2-Axis Hall Sensors with Curve Fitting.....	15
1.3.5.3 3-DOF Hall Sensor Array with Filtering of 1 st and 2 nd Spatial Harmonic.....	19
1.3.5.4 Areas for Improvement	22

1.4	Proposed Sensor Solution	24
1.5	Chapter Descriptions.....	27
Chapter 2: Principle and Theory of Magnetic Position Sensor.....		28
2.1	Magnetic Field	28
2.2	Sensor Placement	30
2.3	2-DOF Principle.....	33
2.4	Position Calculation	34
2.5	6-DOF Principle.....	37
2.6	Error Modelling	38
2.6.1	Magnetic Interference from Stator.....	41
2.6.2	Magnetic Field Temperature Dependence	43
2.6.3	Gain Error	44
Chapter 3: Prototype Design.....		47
3.1	Hall Effect Sensor Selection	47
3.2	Summing Amplifier	49
3.3	PCB Layout.....	51
Chapter 4: Experiment.....		53
4.1	Experiment Set Up.....	53
4.2	Experiment Results	55
Chapter 5: Sensor Sorting.....		64
5.1	Motivation.....	64
5.2	Test Circuit Design	65
5.3	Zero Magnetic Field Reference	68

5.4	Magnetic Field	69
5.4.1	Design	69
5.4.2	Assembly.....	79
5.5	Kinematic Coupling	85
5.6	Software	87
5.7	Work Flow	88
5.8	Results.....	89
5.8.1	Repeatability	90
Chapter 6: Conclusions		94
6.1	Future Work.....	97
Bibliography		98

List of Tables

Table 1-1 – Requirements of the position sensor.....	7
Table 3-1 – AD22151 sensor specifications	48
Table 5-1 - Results of repeatability test for sensor sorting	90
Table 6-1 - Requirements achieved	96

List of Figures

Figure 1-1 – Existing optical metrology system for planar motor	11
Figure 1-2 – 4-DOF Hall sensor array over 2-D Halbach array	14
Figure 1-3 – Two 2-axis sensors and their relative distance.....	16
Figure 1-4 – X axis of Hall sensors measuring X component of magnetic field.....	17
Figure 1-5 – 1-D Hall sensor array below checkerboard magnet array	20
Figure 1-6 – 2-D Hall sensor array above checkerboard magnet array	21
Figure 1-7 – Hall element principle	25
Figure 2-1 – Z component of magnetic field below 1-D Halbach array.....	28
Figure 2-2 – 1-D array of Hall sensors below Halbach array	31
Figure 2-3 – 2-D array of Hall sensors below Halbach array	33
Figure 2-4 – Three sensor measurements resolved to two measurements 90 degrees apart.....	36
Figure 2-5 – Direction of magnetic field generated by trace at Hall sensor location	42
Figure 2-6 – Plot of maximum position error possible due to +/- 10% gain variation	46
Figure 3-1 – AD22151 and external components	49
Figure 3-2 – 3x3 Hall sensor array with summing amplifier for one column	50
Figure 3-3 – Hall sensor array prototype (fixed to CNC table for testing).....	52
Figure 4-1 – Prototype fixed to CNC table with magnet array positioned using CNC spindle....	53
Figure 4-2 – Error in X and Z for sweep in X at 4.2 mm flying height.....	55
Figure 4-3 – Error in X and Z for two sweeps in X to show repeatability	56
Figure 4-4 – Voltage output for decoupled sensor row during sweep in X.....	57
Figure 4-5 – Error in X and Z for sweep in X at 5.2 mm flying height.....	58

Figure 4-6 – Error in X and Z for sweep in Y at 4.2 mm flying height.....	59
Figure 4-7 – Error in X and Z for sweep in Z, showing saturation.....	60
Figure 4-8 – Error in X and Z for sweep in Z.....	61
Figure 4-9 – Variation in X position for 20 measurements to show X position resolution.....	62
Figure 4-10 – Variation in Z position for 20 measurements to show Z position resolution.....	63
Figure 5-1 – Gain determined by sampling the sensor voltage in two known magnetic reference fields.....	65
Figure 5-2 – Sensor sorting PCB attached to aluminum base	67
Figure 5-3 – Zero magnetic field reference consisting of mu-metal wrapped around a plastic tube	68
Figure 5-4 - Magnetic flux lines for magnet-opposite-gap configuration	71
Figure 5-5 - Normal magnetic flux density distribution along line through gap for magnet-opposite-gap configuration	71
Figure 5-6 - Magnetic flux lines for magnet-near-gap configuration.....	72
Figure 5-7 - Normal magnetic flux density distribution along line through gap for magnet-near-gap configuration	72
Figure 5-8 - Magnetic flux lines for magnet-near-gap configuration with high-permeability sheets.....	73
Figure 5-9 - Normal magnetic flux density distribution along line through gap for magnet-near-gap configuration with high-permeability sheets.....	73
Figure 5-10 - COMSOL model of magnetic field source	74
Figure 5-11 - Vertical component of magnetic field in the gap along X.....	75
Figure 5-12 - Vertical component of magnetic field in the gap along Y	76

Figure 5-13 - Vertical component of magnetic field in the gap along Z	76
Figure 5-14 - Vertical component of magnetic field at the sensor location for different socket positions in X	77
Figure 5-15 - Vertical component of magnetic field at the sensor location for different socket positions in Y	78
Figure 5-16 - Vertical component of magnetic field at the sensor location for different socket positions in Z.....	78
Figure 5-17 - Machined components for magnetic field source	79
Figure 5-18 - Magnetic field source prior to inserting magnets	80
Figure 5-19 - Temporary wooden guides for inserting the magnets into the magnetic field source	81
Figure 5-20 - First magnet approaching the final resting place	82
Figure 5-21 - Wooden guides in place for second magnet insertion	83
Figure 5-22 - Magnets fully inserted into the magnetic field source	84
Figure 5-23 - Original kinematic coupling geometry, using magnetic attraction of steel disc for preload.....	85
Figure 5-24 - Improved kinematic coupling geometry, using gravity for preload	86
Figure 5-25 - Bottom view of PCB assembly showing vee grooves and steel disc in PCB base.	87
Figure 5-26 - Side view of PCB base showing ball and grooves for kinematic coupling	87
Figure 5-27 - Inverted vee groove and two balls for kinematic coupling inside receptacle.....	87
Figure 5-28 - PCB assembly inserted into aluminum receptacle.....	87
Figure 5-29 - Work station layout for sensor sorting.....	89
Figure 5-30 - Sensor A voltage difference measured at different times	91

Figure 5-31 - Reference sensor voltage measured simultaneously with sensor A voltage..... 92

Figure 5-32 - Sensor B voltage difference measured at different times 92

Figure 5-33 - Reference sensor voltage measured simultaneously with sensor B voltage..... 93

List of Abbreviations

1-D	One Dimensional
2-D	Two Dimensional
3-D	Three Dimensional
ADC	Analog to Digital Converter
CNC	Computer Numerical Control (machine)
DOF	Degree Of Freedom
FPGA	Field-Programmable Gate Array
GLSDC	Gaussian Least Squares Differential Correction
GUI	Graphical User Interface
ID	Identifier
INA	Instrumentation Amplifier
LED	Light Emitting Diode
PCB	Printed Circuited Board
RMS	Root Mean Square
SOIC	Small Outline Integrated Circuit
VHDL	VHSIC Hardware Description Language
VHSIC	Very High Speed Integrated Circuit
X	X direction (typically a planar direction)
Y	Y direction (typically a planar direction, orthogonal to X)
Z	Z direction (typically a vertical direction, orthogonal to X and Y)

Acknowledgements

Thank you very much to Dr. Xiaodong Lu for his guidance, teaching, and patience. He is always available to answer questions and assist with hands-on research. His explanations of mechatronic principles are intuitive. And he always knows the best lunch spots on campus.

Thank you to my labmates, past and present: Eric Buckley, Fan Chen, Rui Chen, Mark Dyck, Jian Gao, Irfan-ur-rab Usman, and Kevin Xiao, for their assistance and comradery. Eric is the lab expert on PCB design, VHDL logic, EtherCAT, and socialism. Fan is an expert on both machining controls and salsa dancing. Rui is carrying the torch on the planar motor, and supplies us with cheap meals. Mark showed us all how to excel academically and still be home for supper time. Jian didn't complain once when he sorted half of the 12,700 sensors, nor on the camping trip. Irfan is always keen to share his knowledge on all things mechatronic and cheerleading. Kevin gave me a crash course on EtherCAT. Irfan and Fan were also my TA's during undergrad, and got me interested in the research of the Precision Mechatronics Lab, while Eric and Mark have been my classmates since 2008.

Thank you to the UBC professors for their teaching and time, especially the Mechatronic professors for sharing their tradecraft. As well, thank you to the staff at UBC, including the purchasers, machinists, technicians, office staff, custodians, and all others.

Thank you to my wonderful girlfriend Kayli, for keeping my spirits up and my stress levels down, and sacrificing so much free time the last month to help me finish this thesis. Thank you

to Jan and Terry, for being fantastic and supportive parents and encouraging me in my studies and life in general. Thank you to Eleanor and Fred, for feeding a hungry grad student. Thank you to Keltie and Chris, for putting up with this eternal student, and Danny, for sending me my logbooks during crunch time.

Thank you to the NSERC CANRIMT Research Network for funding this research.

For Kona

Chapter 1: Introduction

The goal of this thesis is to present the development and verification of a multi-degree of freedom (DOF), non-contact position sensor for a magnetically levitated planar motor. The position sensor consists of a 2-D Hall sensor array to sense the position of moving Halbach magnet arrays. A prototype has been designed and tested.

In addition, a sensor sorting setup was designed, built, and used to sort 12,700 sensors based on gain. Variation in sensor gain is a common cause of position error in previous Hall sensor arrays.

1.1 Planar Motor

A planar motor is a direct drive multi-degree of freedom motion stage. To be considered a planar motor, the minimum controllable degrees of freedom (DOF) are X and Y planar motion, but a planar motor can have up to six controllable DOF, three translations and three rotations.

Actuation in existing planar motors is achieved through magnetic reluctance, moving coils, or moving magnets. Levitation is possible, through air bearings, fluid bearings, or magnetic levitation. A planar motor is considered direct drive because actuating forces are applied directly to the moving stage without intervening bearing and transmission elements. In comparison, a serial architecture uses single-DOF actuators, typically linear motors or lead screws, stacked in series to achieve each degree of freedom, or to achieve fine (high precision, short stroke) and coarse (low precision, long stroke) motion for a single DOF.

The potential applications for planar motors include manufacturing processes such as assembly, inspection, lithography, and machining. Many manufacturing machines currently use X-Y tables

or gantries for planar motion, both examples of serial architectures. In the semi-conductor industry, high accuracy and speed is required for wafer steppers, and small displacement in Z would be beneficial. As well, applications currently relying on linear motion could benefit from direct-drive planar motion. For example, with multiple moving stages, a planar motor system could replace a conveyor in an assembly line, allowing high-speed moving stages to overtake each other, assemble in groups, or move laterally to work stations. This would provide flexibility and opportunities for optimization in factory automation design.

The advantages of planar motors derive from their direct drive architecture. Serial architectures require five passively constrained DOF for each actuator, resulting in decreased mechanical stiffness for the mover and increased accumulation of position error. The stacked actuators result in multiple moving masses, which limit the acceleration, speed and bandwidth, and increases working volume. In contrast, direct drive architectures have potential for high stiffness, high precision, and zero backlash due to the direct force and lack of bearing elements. The single moving mass allows for high acceleration, speed, and bandwidth, and simplified controls. The overall structure is lightweight and the compact working volume can scale with stroke. As a result, the cost can be reduced.

Magnetic levitation provides further advantages due to the non-contact nature, including isolation from ground vibration, zero friction, no lubrication, as well as increases in speed, acceleration, and accuracy. With no friction, the position error can be minimized within the resolution and accuracy of the position sensor. No lubrication, due to no mechanical bearings, is particularly suitable for vacuum conditions, as lubrication might pollute a vacuum.

Xiaodong Lu and Irfan Usman recently developed a novel six-DOF magnetically levitating planar motor [1] [2]. The stage has long, linearly scalable stroke in directions X and Y. The moving stage, or mover, developed by Lu and Usman is a levitating, untethered mass embedded with four 1-D four-segment-per-period Halbach permanent magnet arrays. A Halbach array consists of individual magnets with a spatially rotating pattern of magnetization, and is described in more detail in Section 2.1. The stator consists of multiple layers of electrical coils fabricated using a printed circuit board process.

The novel design of this planar motor results in multiple advantages compared to other planar motors. The long, linearly scalable stroke in X and Y directions allows new applications for planar motors without increasing system complexity. The six controllable DOF, including magnetic levitation, provide the benefits of non-contact motion as well as high stiffness in all DOF. The mover does not require a tether, unlike moving coil planar motors which require cooling and/or electricity. The tether limits stroke and adds a force disturbance to the mover. Multiple stages are possible, enabling higher throughput for manufacturing processes, as well as enabling conveying applications. The control and commutation is easy to implement due to the linear and position-independent force distribution, and lack of force coupling, coil end effects, and magnetic field edge effects. The stator has a high coil filling factor resulting in large force density and high acceleration, and is mass producible with current PCB manufacturing processes.

1.2 Sensor Requirements

The unconstrained mover is unstable unless controlled in a closed loop with real-time position feedback. Because of the lack of mechanical constraints, the mover stiffness derives from the

sensor position feedback. The precision of the planar motor is only limited by the resolution of the sensor solution. Other benefits of closed loop control compared to open loop control include higher speed, bandwidth, accuracy, and repeatability. Therefore, a position sensor is required.

To maintain the non-contact benefits of the planar motor, the sensor also needs to be non-contact.

Because the mover is a single mass as opposed to stacked stages, and because six DOF are controlled, the system must sense six DOF simultaneously. An indirect kinematic chain of single-axis sensors would mechanically interfere with the mover and have significant error accumulation, negating the non-contact and direct drive benefits.

Absolute measurement, as opposed to incremental measurement, is required because at start-up, the mover will not be levitating. To achieve levitation and control, current commutation is required, which depends on the position of the mover. An incremental sensor requires the mover to be placed at a starting position, which is very undesirable after a temporary stop in work. As well, for manufacturing tasks such as microassembly, repeatable motions are required, which is best achieved by an absolute sensor. In addition to the need for a precise starting position to achieve repeatable motions, an incremental sensor can “lose count”.

The long stroke benefit of the planar motor of interest cannot be realized without position feedback over the whole stroke, on the scale of several metres or more in X and Y. The planar motor has an approximate working range of 10 mm in Z.

The ability to control multiple movers will enable higher throughput for manufacturing processes, as well as enable conveying applications. Therefore, the sensor should be capable of sensing multiple movers simultaneously.

Many industrial applications rely on an overhead structure, including pick and place, optical inspection, and photolithography machines,. As a result, the sensor should not require unobstructed space above the mover.

An advantage of the planar motor of interest is that the mover does not require power or communications. The sensor should therefore not require power or communications supplied to the mover. Power would need to be supplied by a battery, which requires wireless charging or periodic stopping for charging, or a tether. Communications would need to be provided by a tether or wirelessly, which could reduce the bandwidth. These and other modifications would add weight and/or add a force or torque disturbance. Preferably, no modifications are required for the mover.

Because the planar motor is non-contact, all stiffness comes from sensor feedback. Static stiffness is infinite within the sensor resolution and actuator force limits, but the dynamic stiffness of the mover depends on the sensor bandwidth. Any frequencies beyond the sensor bandwidth cannot be actively damped. As well, the response time and trajectory accuracy depends on the bandwidth. A sensor bandwidth of several kHz is sufficient to ensure the sensor is not a limiting factor for the closed loop system bandwidth. As well, the higher the bandwidth, the lower the position uncertainty during high speeds.

The performance of the sensor should not degrade at high speeds and accelerations for the mover. In addition to a high bandwidth, effects due to the moving magnet such as eddy current need to be considered.

Industrial adaptation of planar motors for some applications is prevented by a lack of economical solutions for multi-axis position feedback over long strokes. One multi-DOF metrology solution is laser interferometry, which is very expensive. Reducing cost compared to laser interferometers will encourage industrial adoption of the planar motor for new applications.

Micrometre-level resolution and error is adequate for many automation applications, including assembly, conveying, and machining. The static stiffness is limited by the sensor resolution.

Micrometre-level resolution and error is not adequate for photolithography, but the proposed sensor could be used as a backup in case a higher precision sensor such a laser interferometer fails, or for coarse motion over long stroke between high precision work stations, where a higher precision sensor assumes position feedback over a small range.

These requirements are summarized in Table 1-1.

Table 1-1 – Requirements of the position sensor

#	Requirement
1.	Non-contact
2.	6-DOF capable
3.	Absolute measurement
4.	Metre-level range in X and Y range
5.	10 mm range in Z
6.	Sense multiple movers
7.	Require no unobstructed space overhead
8.	Require no power or communications supplied to the mover
9.	High bandwidth, several kHz
10.	No performance degradation at high speed/acceleration (m/s, dozens of m/s ²)
11.	Cost-effective
12.	Micrometre-level resolution and error, or better

1.3 Existing Metrology Solutions

Existing solutions for multi-DOF, non-contact position measurement of planar motors include: laser interferometry, surface encoders, capacitive sensors, stereo vision, and Hall sensor arrays.

1.3.1 Laser Interferometry

A common method of multi-DOF, non-contact position measurement for planar motors is a laser interferometric system [3] [4] [5] [6] [7] [8]. Laser interferometers have nanometre-level accuracy and resolution. They are typically only used to measure planar position and rotation,

and combined with capacitive or other sensors for the out-of-plane DOFs, although 6-DOF is possible when using six laser interferometers [8]. Rotational range is typically limited to the milliradian-level, because rotations cause the laser beam to miss the detector. However, Zhang and Menq [8] achieved a rotational range of ± 8 degrees, by combining retroreflectors, which have a poor translational range, with plane mirrors, which have a poor rotational range.

Large mirrors are necessary for large translational range, which results in increased weight for the mover. Laser interferometers are not absolute sensors, so additional sensors are necessary to determine position on start-up, in order to achieve current commutation necessary for levitation. The metrology system cannot be integrated with the stator and a separate metrology frame may be needed, obscuring work space. The wavelength of the laser, which is the reference scale, is sensitive to environmental conditions, and environmental control is necessary to maintain the nanometre-level accuracy. The cost of a laser interferometric system is prohibitive for many applications, especially those not requiring nanometre-level precision.

1.3.2 Surface Encoder

Surface encoders, utilizing a surface grid and encoder head, can provide multi-axis position feedback for planar motors. Different configurations can measure 3 lateral DOF (X, Y, and yaw) [9], 3 translational DOF (X, Y, and Z) [10], 5DOF (not Z) [11], and 6-DOF. 6-DOF is possible by combining a 3-D displacement sensor with a 3-D angle sensor [12] or by using multiple 2-DOF encoders [13]. Resolution ranges from micrometre to nanometre-level, and subnanometre resolution is possible [10]. Grids need to be diamond turned or fabricated with lithography using processes still in development [14]. As a result, the availability is minimal, the cost is currently

expensive, and the range is limited to around 100 mm or less. Typically, these passive encoders are incremental, but absolute measurement is possible with a complex and expensive scale which uses optical pattern recognition [15].

Active encoders measuring 3 lateral DOF using commercially available displays and cameras [16] or CCD sensors [17] have also been developed. These active encoders can achieve absolute measurement. The active encoder using a camera achieves nanometre-level resolution but has a slow bandwidth and is bulky, while the encoder using CCD sensors has submicrometre resolution, fast bandwidth and is compact. The inclusion of a display increases the required air gap and reduces efficiency for the planar motor.

All the surface encoders require modifications to the mover. Typically the mover contains the bulky encoder head which is not desirable due to space constraints and the need for an umbilical. The grid may also be placed on the mover, but this limits the range significantly, and the encoder head would interfere with the stator for the planar motor of interest.

1.3.3 Capacitive Sensor

Typically, capacitive sensors are only used for out-of-plane position measurements, in combination with a planar sensor such as laser interferometers [3] [4] [6]. Capacitive sensors typically have high resolution and low range, which makes them suitable for this purpose.

Planar capacitive sensors have been developed to measure 2-DOF planar motion over tens of millimetres with submicrometre resolution [18] [19] [20] [21]. Z position has also be detected,

but only for gaps less than 10 μm and while the mover is stationary [19]. Ahn et al. have developed a 5DOF disc-type capacitive sensor [22], but this topology is not suitable for planar motors.

1.3.4 Stereo Vision

Lu, Rao and Usman achieved six DOF absolute position feedback for the planar motor of interest through the use of stereo optical metrology [23]. As shown in Figure 1-1, two cameras mounted one metre above the Planar Motor monitor the position of four infrared LED's on the Mover.

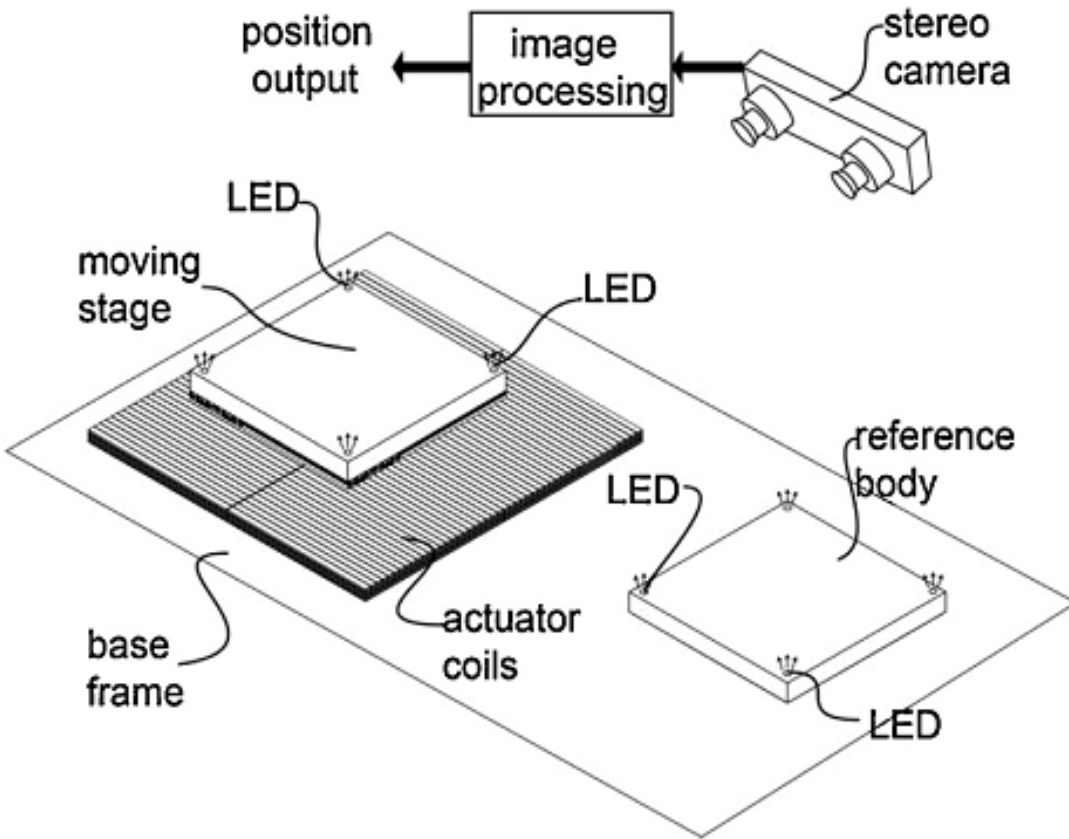


Figure 1-1 – Existing optical metrology system for planar motor¹

The cameras measure 6-DOF for multiple bodies simultaneously. This avoids the problems of sequential measurements, including error due to movement and reduced sampling rate. The cameras also image a reference body, shown in Figure 1-1, to decouple the effect of camera mounting structure vibration. The sampling rate is 8 kHz, which enables high dynamic stiffness, high bandwidth, and fast response. After calibration, the error for a single LED has zero mean and RMS values of 3.1 μm in X, 5.4 μm in Y, and 13.8 μm in Z. The RMS resolution is 0.6 μm

¹ Reprinted from [23], Copyright 2013, with permission from Elsevier

in X and Y, 0.9 μm in Z, 2.1” in Rx, 2.2” in Ry, and 0.5” in Rz. The working volume is 400 mm x 400 mm x 15 mm in X, Y, and Z respectively, with the cameras positioned 960 mm above the stator.

There are drawbacks that limit some industrial applications for this sensing solution. The most significant is that this method requires a metre of unobstructed space above the Mover to maintain line of sight. However, for many industrial applications, this space is difficult to achieve throughout the work volume. For example, many machines, including pick and place, optical inspection, and photolithography machines, rely on an overhead structure. As well, a workpiece on the mover must not obscure the LEDs, and the LEDs must be kept clean from dust and dirt. While the optical metrology system functions with partial obstruction of view, a more robust solution would function regardless the overhead operation of the machine. To extend the range of the planar motor, more cameras are needed, and reference bodies must be located beside the stator at repeated intervals to decouple the structure vibration. This limits the maximum 2-D range possible, unless “islands” for the reference bodies are incorporated or the structure vibration is minimized with a different method. Lastly, the mover requires power from a battery for the LEDs, which would require intermittent interruptions in each mover’s availability to allow time for battery charging or replacement, or implementation of a wireless charging system.

1.3.5 Hall Sensor Array

Several researchers have used Hall sensors to sense position for a planar motor by measuring the magnetic field of the magnet array. For applications requiring micrometre-level accuracy and resolution, Hall sensor arrays are a cost-effective method because the planar motor already

makes use of a periodic magnet matrix. Hall sensors are absolute, which is required for levitation upon start-up. Although not true for all of the previously developed Hall sensor arrays, they are high bandwidth, can be integrated into the stator to avoid interfering with the mover or working area, and are capable of sensing multiple movers in 6-DOF over long range and large rotations.

1.3.5.1 4-DOF Hall Sensor Array with Filtering of 1st Spatial Harmonic

Frissen et al. [24] [25] used arrays of Hall sensors to measure the position of at least four DOF for their moving coil planar motor. Their planar motor has a stationary magnet array which is a 2-D Halbach array. The magnetic field is a superposition of sine waves with X and Y spatial frequencies. The coils and sensors are rotated 45 degrees with respect to the magnet array orientation, minimizing the harmonics after spatial integration.

The hall sensor array and 2-D Halbach array are shown in Figure 1-2.

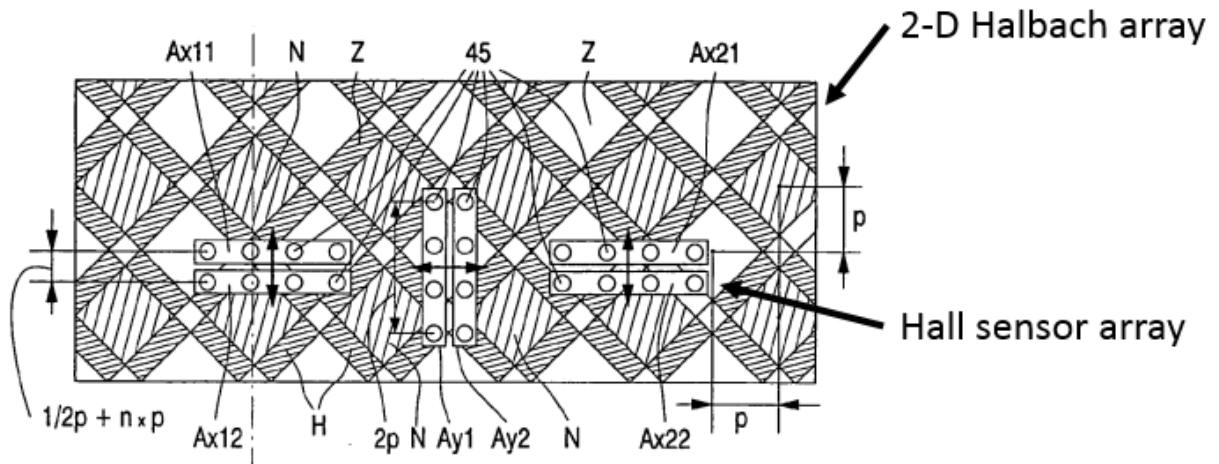


Figure 1-2 – 4-DOF Hall sensor array over 2-D Halbach array²

A linear array of four Hall sensors was used to measure translation orthogonal to the direction of array extension, and to decouple from translation along the direction of array extension. The average value of the four sensors is constant except for a ripple when the mover translates along the direction of array extension. The average is obtained by using a summing amplifier for the outputs of the four sensors.

λ , or $2p$ in Figure 1-2, is the wavelength of the magnetic field. By using two linear arrays separated by $\lambda/4$, quadrature is possible and the position orthogonal to the direction of array extension can be calculated. Instead of two linear arrays, they suggest that one linear array of 2-axis sensors (with axes 90 degrees apart) could be used instead. To measure the orthogonal

² Reprinted from [24]

translation motion, an identical set of arrays is used but rotated 90 degrees. The vertical distance is calculated from the amplitude of the magnetic field. They measure rotation by using two sets of arrays separated by a distance along the direction of array extension. The rotation can be calculated by the difference in the position measured by these two arrays.

They suggest the sensors can be placed equal distances from the sides of the rectangular coil in the mover in order to minimize the magnetic interference generated by the electric coils. Also, any remaining magnetic interference can be compensated because it is known.

The accuracy is limited by offset and gain errors of the Hall elements. To compensate for gain errors, they use individual differential amplifiers so the gain can be adjusted. They achieve an absolute accuracy of 1% of the half wavelength, or around 300 μm .

1.3.5.2 3-DOF Sensor Using 2-Axis Hall Sensors with Curve Fitting

Kawato and W.-J. Kim [26] used Hall sensors to measure the position of their moving coil planar motor, with the intention of unrestricted range in X, Y, and yaw, as opposed to laser interferometers. The remaining DOFs were constrained by an air bearing.

Their planar motor has a 2-D Halbach magnet array, although they claim their principle works for various magnet arrays. The largest harmonic of the magnet array, after the fundamental harmonic, is the 5th harmonic. Because the coils and sensor arrays are not rotated 45 degrees with respect to the magnet array, unlike [24] this harmonic is significant for the sensor array.

To measure 3-DOF, their principle requires a set of two 2-axis sensors, as shown in Figure 1-3.

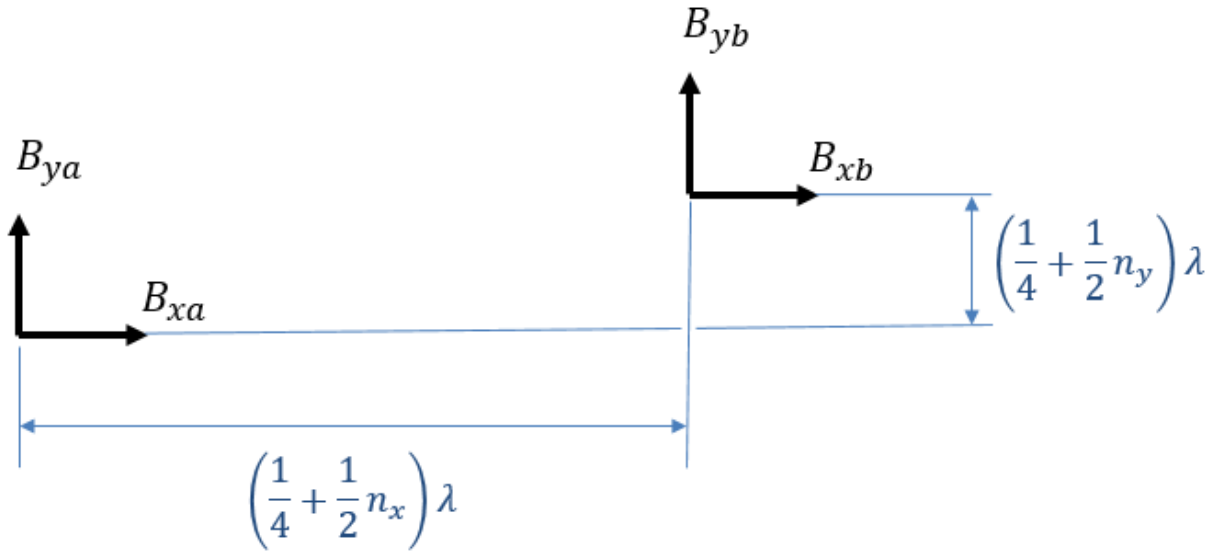


Figure 1-3 – Two 2-axis sensors and their relative distance

However, they found three sensors were necessary to avoid instability due to error and noise.

The X (and Y) component of the magnetic field of the magnet array only depends on the X (and Y) position. By measuring the X component of the magnetic field, the position in the X direction can be measured, as shown in Figure 1-4.

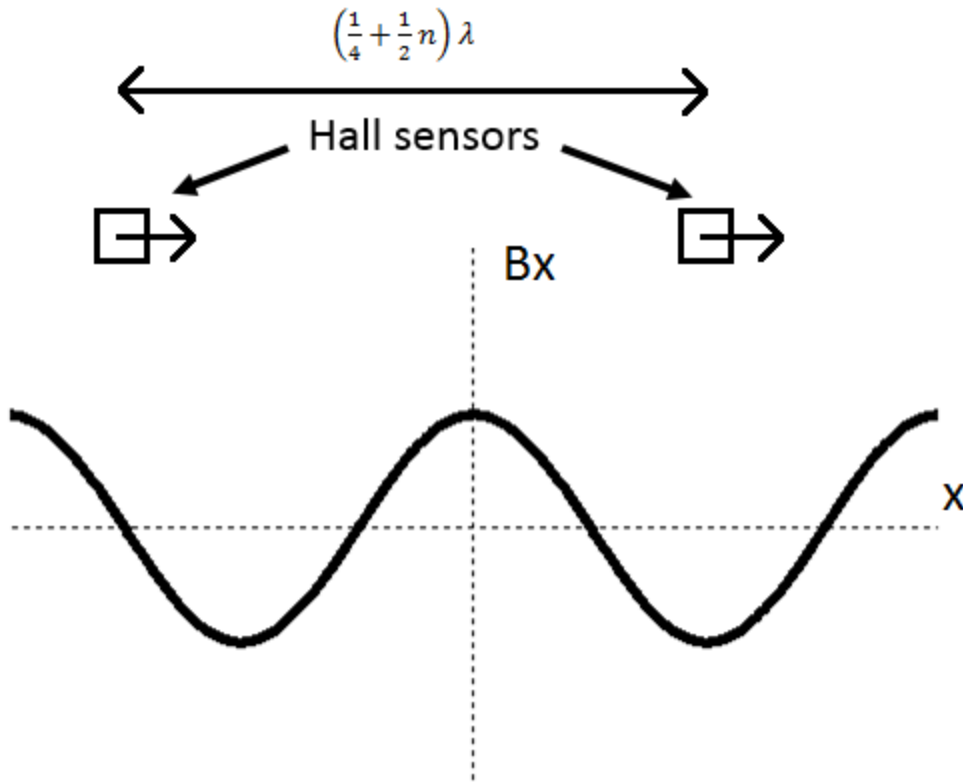


Figure 1-4 – X axis of Hall sensors measuring X component of magnetic field

Each sensor can measure both the X and Y component of a magnetic field. Therefore, the position in X and Y can be measured. As there are redundant measurements, the yaw rotation can also be determined from the difference in the measurements. The pitch of their sensors is $(\frac{1}{4} + \frac{1}{2}n)\lambda$, where n is an integer, so that one sensor is always located where the gradient of the magnetic field is large, in order to maximize sensitivity. They use a current source to drive the Hall sensors, an operational amplifier circuit for gain, and an anti-aliasing filter with a 200 Hz corner frequency.

Using laser interferometer measurements over a zig zag trajectory, the Hall sensor outputs are curve fit to the model parameters for the fundamental and 5th harmonic using batch least squares.

Gaussian Least Squares Differential Correction (GLSDC) is used for the nonlinear mapping during operation. The GLSDC operates with 800 Hz sampling frequency and takes 3 loops to converge, or 3.75 milliseconds. Digital lead lag compensators were implemented with phase crossover frequencies of 10 Hz for X and Y, and 20 Hz for θ_z , so the sampling frequency is sufficient.

The position sensor has 10 μm translation resolution and 100 μrad rotation resolution, 16 degree rotational range, and 1.4 mm translational error prior to calibration, which is unacceptable for most applications. To improve the accuracy, error-mapping with a laser interferometer and linear interpolation is required. This improves the error by a factor of 20 to less than 100 μm . However, error mapping for rotation was not implemented because rotation beyond a few milliradians could not be measured with laser interferometers.

They recommend sensor calibration and redundant sensors to reduce the error. They propose that the sources of error include fabrication error of the magnet array, variations in magnet material properties including magnetization direction and remanence, modeling error of magnet array using batch least squares, sensor rotational misalignment, error in sensor location, external magnetic field interference, and sensor noise.

Kawato and W.-J. Kim also propose that 6-DOF can be measured with a minimum of three sensors. One sensor would measure the X and Y component of magnetic field, one sensor would measure the X and Z component of magnetic field, and one sensor would measure the Y and Z component of magnetic field. However, more sensors are likely necessary to ensure stability.

1.3.5.3 3-DOF Hall Sensor Array with Filtering of 1st and 2nd Spatial Harmonic

Ahn and K. R. Kim [27] [28] used an array of Hall sensors to measure the X and Y position of their planar motor. Yaw is not measured. Air bearings constrain the remaining DOFs.

The planar motor has a moving checkerboard magnet array, using only north and south (i.e. vertically) oriented magnets. Similar to a 2-D Halbach array, the magnetic field is a superposition of sine waves with X and Y spatial frequencies. However, in addition to the fundamental component, there are 2nd, 4th... harmonics, that is, every (2n)th harmonic.

They demonstrate that by summing the outputs of a 1-D (linear) Hall sensor array, they can filter out harmonic signals with a spatial frequency along the direction of array extension. The pattern of Hall sensors must be repeated every $\lambda/2$ in order to remove the desired harmonic signal with wavelength λ . To filter out n harmonic components, 2^n sensors are necessary. Therefore, a 1-D sensor array as shown in Figure 1-5, extending along X with four sensors $\lambda/4$ apart, is decoupled from fundamental and 2nd order X spatial harmonics.

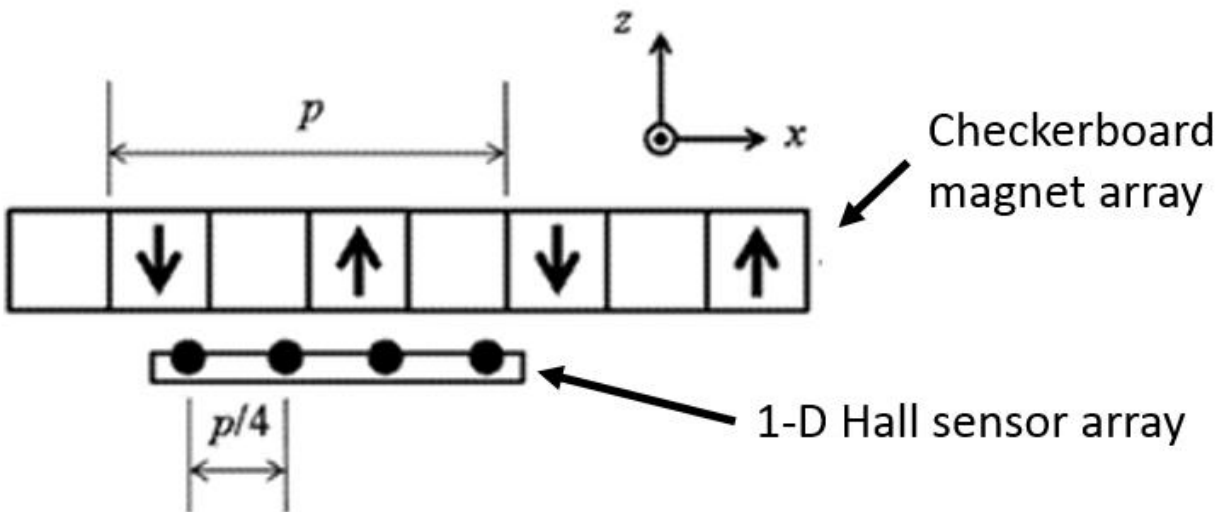


Figure 1-5 – 1-D Hall sensor array below checkerboard magnet array³

By spacing two 1-D sensor arrays $\lambda/4$ apart, quadrature is achieved. For two 1-D arrays extending in X, the X fundamental and 2nd spatial harmonics are filtered out and the position in Y is calculated from the sine and cosine outputs. By doing the same with an array identical in spacing but rotated 90 degrees, the Y fundamental and 2nd spatial harmonics are filtered and the position in X is calculated. Thus, X and Y position can be detected and yet are decoupled. These arrays can overlap; four sensors can be used for both sets of arrays, as shown in Figure 1-6.

³ Reprinted from [27]

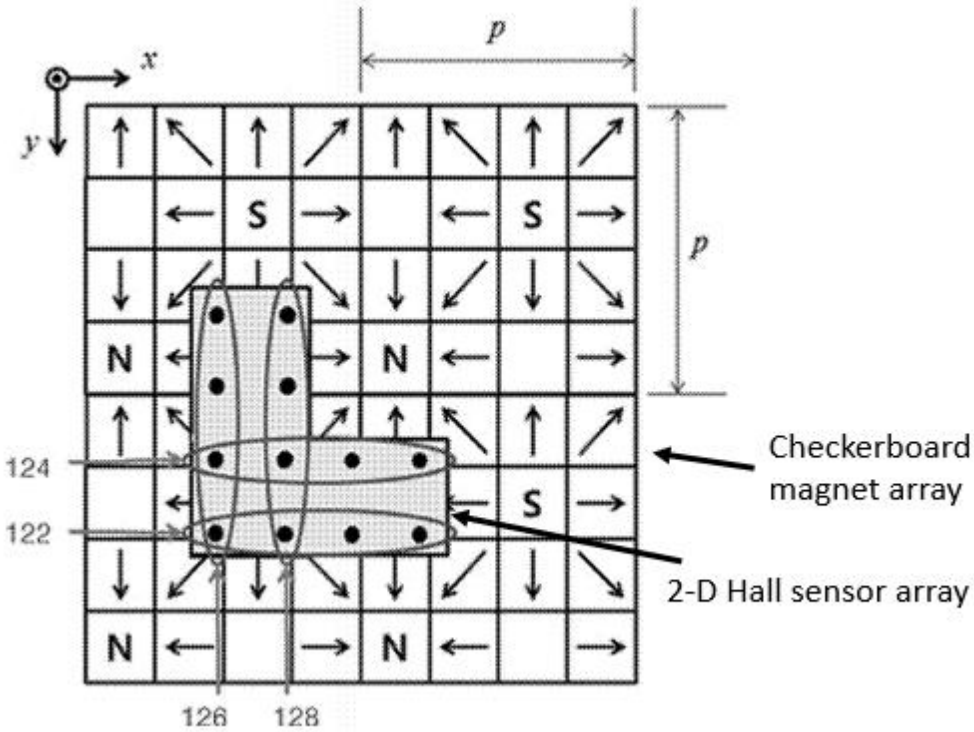


Figure 1-6 – 2-D Hall sensor array above checkerboard magnet array⁴

Operational amplifiers are used for summation of Hall outputs and adjustment of gain and offset. Height Z can be calculated by taking the root mean square of the sine and cosine output to determine the amplitude of the magnetic field, which is height dependent.

Using an X-Y linear motion stage, tests were done at 1, 3, 5, and 8 mm heights. The Hall sensor saturates at 1 mm height as the sensor has a magnetic field range of approximately +/- 0.2T.

From 1 to 5 mm, the 4th harmonic is present. Eight sensors would be needed to remove this. At 8 mm, the sine wave is relatively pure, but the position measurement still has 1 mm error. Ahn

⁴ Reprinted from [27]

and K. R. Kim suggest the error is due to manufacturing tolerances and magnet or Hall sensor variation. For improved accuracy, they suggest using a Halbach magnet array for a more sinusoidal field with fewer harmonics, more sensors, and an error mapping technique similar to that done by Kawato and W.-J. Kim.

1.3.5.4 Areas for Improvement

Frissen et al. measured 4-DOF, X, Y, Z, and yaw, and their set up could be used to measure 6-DOF. Kawato and Kim measured 3-DOF, X, Y, and yaw, and explained how 6-DOF can be obtained, but their presented experimental set up does not allow for it. Ahn and Kim's presented prototype can only measure 3-DOF, X, Y, and Z. The planar motors for Kawato and Kim and Ahn and Kim both use air bearings, so 6-DOF is not necessary. For 6-DOF control of a magnetically levitating mover, 6-DOF sensing is required.

Because Compter et al. and Kawato and Kim have moving coil planar motors, each mover with its own sensor array, the range is not limited by the sensor, and they can have multiple movers. Ahn and Kim have range limited to the size of the mover, and cannot have multiple movers, because the sensor array is smaller in area than the moving magnet array.

Information on the bandwidth is not provided by Compter et al. or Ahn and Kim. Kawato and Kim have a sampling rate of 800 Hz for the GLSDC and a 200 Hz anti-aliasing filter. The GLSDC is computationally intensive and can go unstable. A bandwidth of several kHz would be preferable.

Compter et al. have 300 μm error, Kawato and Kim have 1.4 mm error prior to error mapping, and less than 100 μm error after error mapping, and Ahn and Kim have 1 mm error. For many manufacturing applications, millimetre order error is not sufficient. Compter et al. achieve their accuracy by using a differential amplifier for each Hall sensor to individually adjust gain. This requires individual sensor calibration in a magnetic field, and specific hardware or software values custom to each sensor, difficult to achieve for a large quantity of sensors. Error mapping using laser interferometers as done by Kawato and Kim is not easy for all 6-DOF. In a mass production setting, every planar motor would require calibration through 6-DOF with a high precision sensor or high precision calibration jig. Use of a Halbach array would improve the results for Ahn and Kim.

Compter et al. and Kawato and Kim's Hall sensor arrays only measure absolute local position, within one period of the magnetic field, not absolute global position, because the stationary magnet array pattern repeats. At start-up, movers will have enough position information for current commutation because they are moving coil, but they will not know their global position and cannot execute global trajectories unless range is restricted to one pitch of the magnet array. Ahn and Kim's Hall sensor array can also only measure absolute local position even though their planar motor is moving magnet, because the sensor array is much smaller than the magnet array. However, because of the moving magnet design, there is not enough position information to achieve electrical commutation.

Compter et al. and Kawato and Kim place sensors on their movers, which affects the design of the mover, and requires a tether for electricity and communications. However, the movers already require electricity because they are moving coil.

The design of a Hall sensor array presented in this thesis will attempt to improve on these issues.

1.4 Proposed Sensor Solution

A 2-D Hall effect sensor array is proposed as the sensor solution, since the mover has a large, well-characterized, sinusoidal magnetic field. A Hall sensor is the best magnetic field sensor for this purpose because of the large, linear, bipolar magnetic range. A Hall element, the basic building block of a Hall sensor, is a small, thin sheet of material that outputs a voltage in proportion to the product of the current through the element and the magnetic field normal to the surface of the element.

A Hall element is depicted in Figure 1-7.

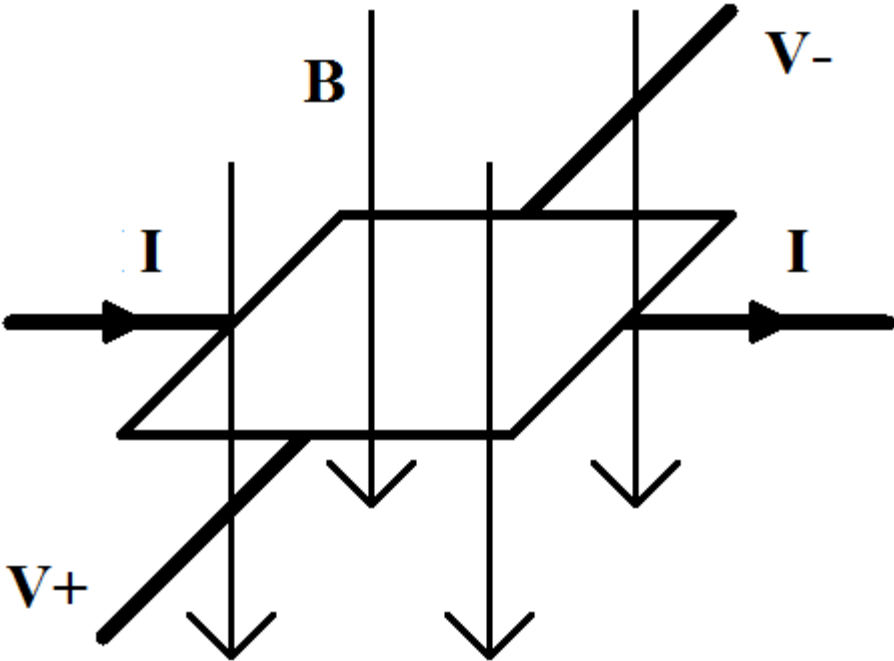


Figure 1-7 – Hall element principle

The equation for the Hall voltage is:

$$V = kIB_{\perp} \tag{1-1}$$

Where k is gain in units of Volts per Amp·Tesla, I is current in Amps, and B_{\perp} is the component of the magnetic field orthogonal to the Hall element plane in Tesla. The Hall element plane is oriented with the mover motion plane for the Hall sensor array.

By measuring the magnetic field in a 2-D sensor array across the planar motor, the magnetic field generated by the mover can be located. The position in two DOF for each magnet array in the mover can be determined. The mover consists of four magnet arrays. Using the eight measurements, the position in six DOF for the mover can be determined.

A Hall sensor array is expected to be able to meet all the requirements. Hall sensors are non-contact because they measure the magnetic field. 6-DOF is achieved by measuring 2-DOF for each magnet array in the mover. Because the position sensor consists of multiple sensors at known locations throughout the measurement range, absolute measurement is possible. The range in X and Y can be extended to whatever range is needed by increasing the size of the Hall sensor array. The magnetic field decays with height but is still at 10% strength at 10 mm, so 10 mm range in Z should be possible. The Hall sensor array will be positioned below the movers and can therefore sense multiple movers. The sensor array will be integrated with the stator PCB for a compact, self-contained design. As a result, no unobstructed space above the mover is required. No modifications or electrical power are required for the mover as it already has the target magnet. A high bandwidth is expected as the sampling rate will only depend on the processing electronics (several kHz or higher); the Hall element bandwidth is not a limiting factor (MHz region). The effect of the moving magnet array is not tested in this thesis and will be explored in future work. Low cost is possible because Hall sensors are available at low cost and the magnet target already exists. This thesis will explore the possible accuracy and resolution of a Hall sensor array.

1.5 Chapter Descriptions

Chapter 2 explains the principle of the position sensor and discusses sources of error.

Chapter 3 outlines the design of a prototype.

Chapter 4 describes the experiment set up and presents and analyzes the results.

Chapter 5 presents a sensor sorting method for ensuring uniform sensor gain.

Chapter 6 concludes with an overview of the thesis, discussion on the research significance and contribution, and identification of future work.

Chapter 2: Principle and Theory of Magnetic Position Sensor

2.1 Magnetic Field

Consider a four-segment-per-period 1-D Halbach array, as shown in Figure 2-1, composed of four individual magnets per period with a spatially rotating pattern of magnetization, i.e. the magnetization of each subsequent magnet is rotated 90 degrees.

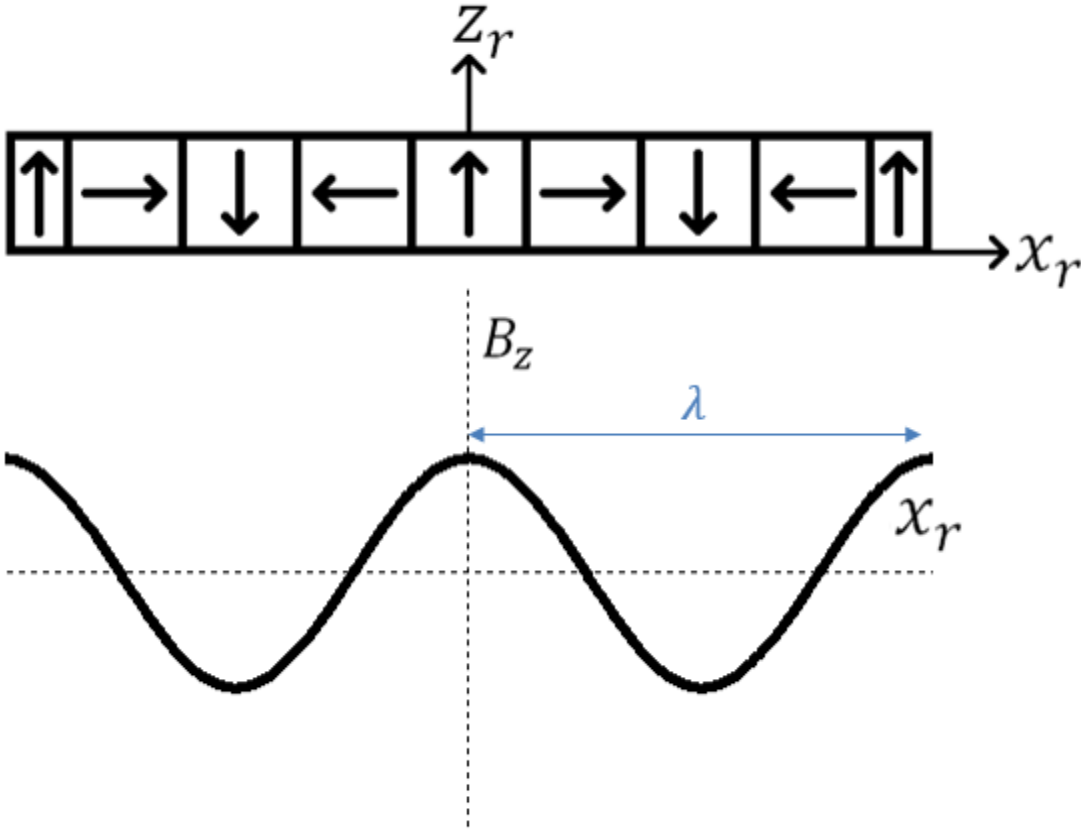


Figure 2-1 – Z component of magnetic field below 1-D Halbach array

The X direction extends along the direction of magnetization rotation and the Z direction extends orthogonal to the array, i.e. vertical. The magnetic field below the Halbach array is periodic in

the X direction and decays exponentially in the negative Z direction. The magnetic field has a fundamental harmonic with a period equal to λ . Because there are four segments per period, the 5th, 9th... harmonics, that is, every $(1+4n)$ th harmonic, are non-zero and all other harmonics are zero [29]. In addition to fewer harmonics compared to a conventional periodic array with alternating vertical magnetization, the advantage of a Halbach array is that the magnetic field below the array is 40% stronger and the magnetic field above the array is near-zero.

The fundamental X and Z components of the magnetic field, B_x and B_z , ignoring boundary effects, are given in [1] as Equation 2-1 and Equation 2-2 respectively.

$$B_z = 0.71B_r \cos\left(\frac{x_r}{\lambda_c}\right) e^{\frac{z_r}{\lambda_c}} \quad 2-1$$

$$B_x = -0.71B_r \sin\left(\frac{x_r}{\lambda_c}\right) e^{\frac{z_r}{\lambda_c}} \quad 2-2$$

B_r is the magnetic remanence, x_r is the position in X relative to the magnet array centre, z_r is the position in Z relative to the bottom of the magnet array, and λ_c is the characteristic spatial wavelength of the magnet, equal to $\lambda/2\pi$.

It is only necessary to measure B_z to determine the position. As well, many Hall sensors are only sensitive to a magnetic field in the vertical direction. Typically, the Hall element is a plane oriented with the orthogonal in the vertical direction. It therefore only generates a voltage due to a magnetic field in the Z direction.

The equation for the Z component of the 5th harmonic is given in [30] as:

$$B_z = -0.14B_r \cos\left(\frac{5x_r}{\lambda_c}\right) e^{\frac{5z_r}{\lambda_c}} \quad 2-3$$

The magnetic field for higher harmonics decay faster than for the fundamental harmonic. For example, at z_r equal to $-\lambda_c/2$, the fundamental harmonic decays 39%, and the 5th harmonic decays 92%. Magnetic harmonics will result in position error as the position calculation assumes only the fundamental component exists.

The mover consists of four 1-D Halbach arrays: two oriented with periodicity along X, called “X-oriented arrays”, and two oriented with periodicity along Y, called “Y-oriented arrays”. The magnetic field for the whole mover is simply the superposition of the magnetic field for the individual Halbach arrays. There are therefore Z components dependent on X position, known as “X directional Z components”, and Z components dependent on Y position, known as “Y directional Z components”.

2.2 Sensor Placement

Consider a 1-D array of Hall sensors extending along X, as shown in Figure 2-2, with a pitch of $\lambda/3$ below an X-oriented Halbach array with wavelength λ .

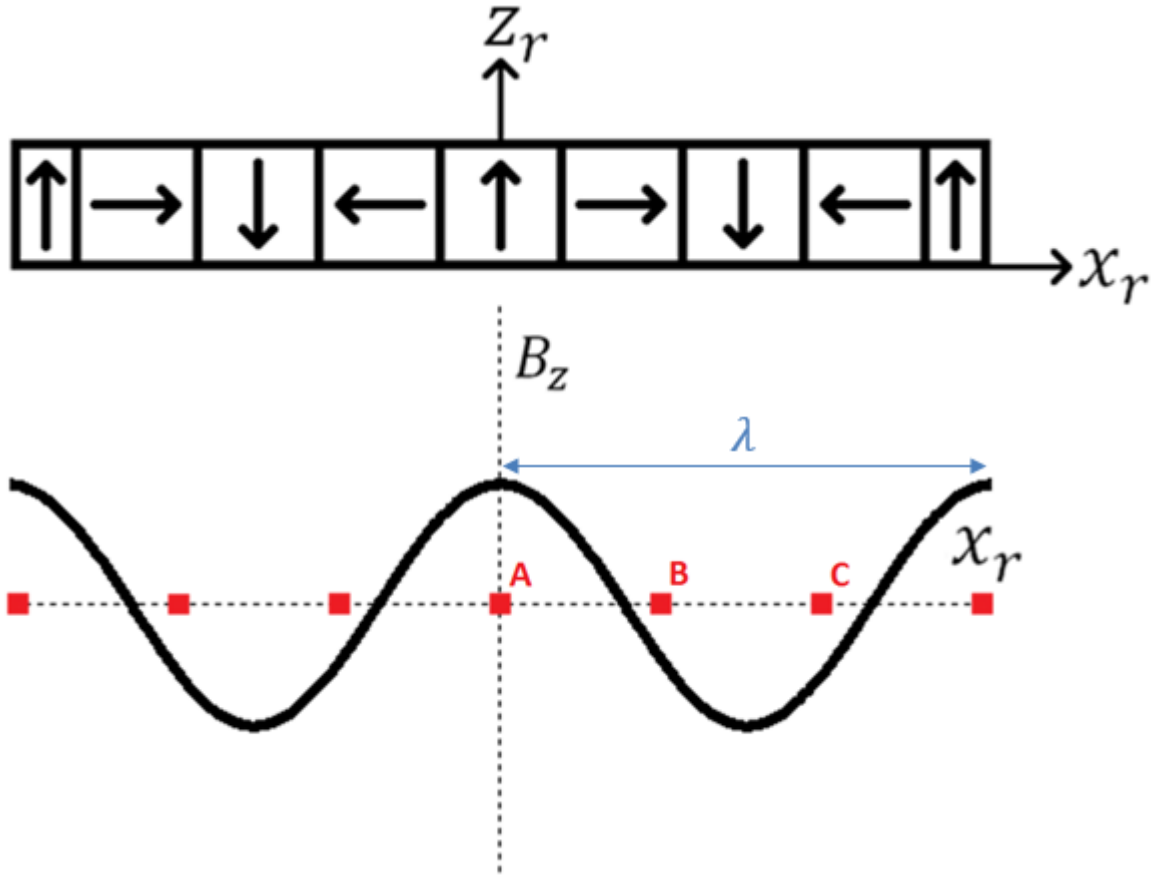


Figure 2-2 – 1-D array of Hall sensors below Halbach array

The fundamental X directional Z component of the magnetic field sensed by three sensors within one period, e.g. sensors A, B, and C in Figure 2-2, is:

$$B_a = 0.71B_r \cos\left(\frac{x_a - x_m}{\lambda_c}\right) e^{\frac{z_r}{\lambda_c}} \quad 2-4$$

$$B_b = 0.71B_r \cos\left(\frac{x_b - x_m}{\lambda_c}\right) e^{\frac{z_r}{\lambda_c}} = 0.71B_r \cos\left(\frac{x_a - x_m}{\lambda_c} + \frac{2\pi}{3}\right) e^{\frac{z_r}{\lambda_c}} \quad 2-5$$

$$B_c = 0.71B_r \cos\left(\frac{x_c - x_m}{\lambda_c}\right) e^{\frac{z_r}{\lambda_c}} = 0.71B_r \cos\left(\frac{x_a - x_m}{\lambda_c} + \frac{4\pi}{3}\right) e^{\frac{z_r}{\lambda_c}} \quad 2-6$$

x_a , x_b , and x_c are the X position of the three sensors A, B, and C. x_m is the X position of the centre of the magnet array.

The sum of the fundamental X directional Z component of the magnetic field sensed by the three sensors is:

$$B_a + B_b + B_c = 0.71B_r e^{\frac{z_r}{\lambda_c}} \left(\cos(\theta_a) + \cos\left(\theta_a + \frac{2\pi}{3}\right) + \cos\left(\theta_a + \frac{4\pi}{3}\right) \right) \quad 2-7$$

Where the angle θ_a is introduced and is equal to:

$$\theta_a = \frac{x_a - x_m}{\lambda_c} \quad 2-8$$

Equation 2-7 is equal to zero, regardless of the position of the magnet array. Therefore, the sum of the sensor outputs in a 1-D array extending along X is insensitive to the fundamental X directional Z component of the magnetic field. Similarly, the sum of sensor outputs in a 1-D array extending along Y is insensitive to the fundamental Y directional Z component of the magnetic field.

Ahn and K. R. Kim use a pitch of $\lambda/4$ to cancel the fundamental component and the second harmonic component of a checkerboard magnet array. However, since the magnetic field below a

Halbach array does not have a second harmonic component, no benefit is gained by using a pitch of $\lambda/4$ as opposed to $\lambda/3$, except redundancy. Using a pitch of $\lambda/3$ instead of $\lambda/4$ sensors requires 7/16 fewer sensors for a 2-D array.

2.3 2-DOF Principle

Consider a single λ -wide X-oriented Halbach array positioned above a 2-D Hall sensor array, as shown in Figure 2-3, with spacing $\lambda/3$ between sensors in both the X and Y directions.

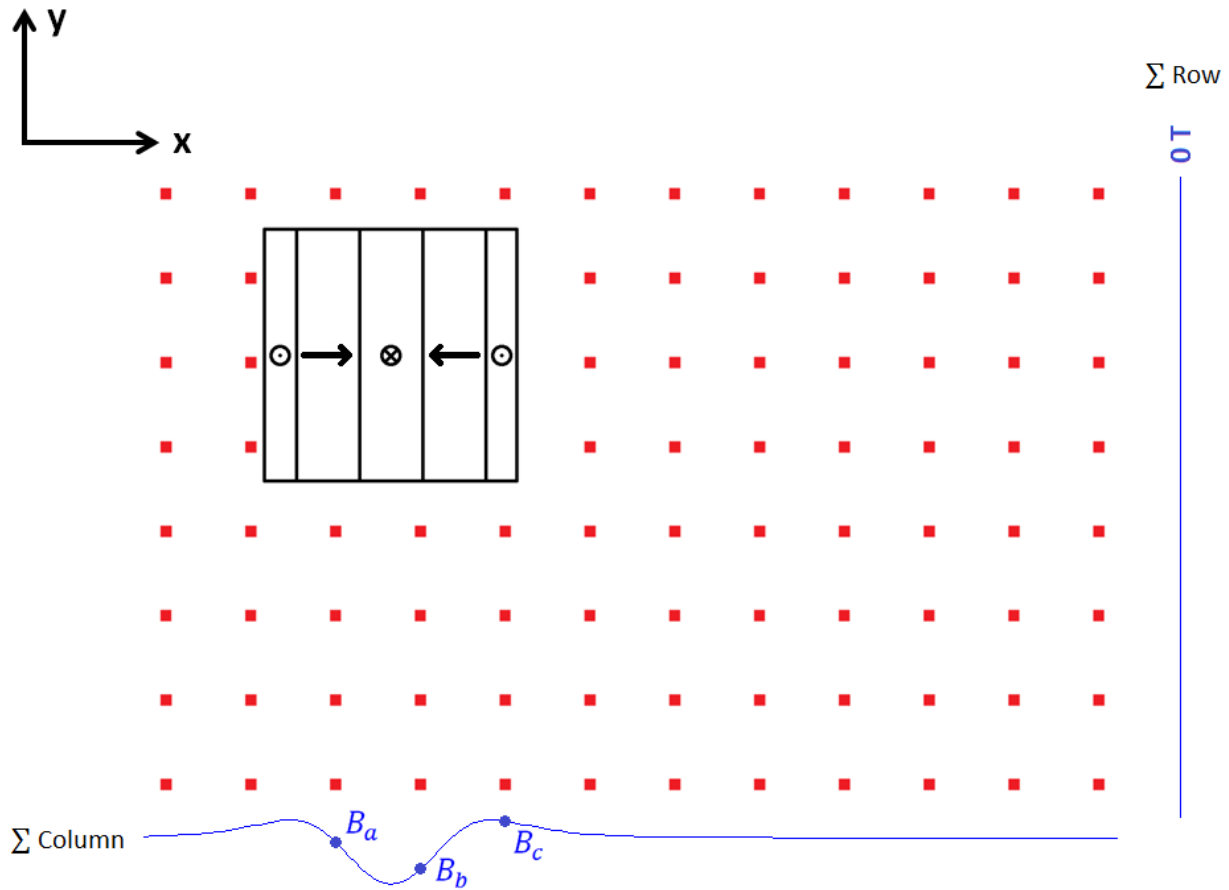


Figure 2-3 – 2-D array of Hall sensors below Halbach array

The outputs for each row (along X) and column (along Y) of sensors is summed. The output of each row is zero as shown previously. The output of each column is insensitive to position of the Halbach array in Y. The output of the columns changes with position of the Halbach array in X. The magnitude of the output increases or decreases with the position of the Halbach array in Z.

Therefore, for an X-oriented Halbach array, the sensor array is only sensitive to position in X and Z, detected by the sum of the sensors in each column. Similarly, for a Y-oriented Halbach array, the sensor array is only sensitive to position in Y and Z, detected by the sum of the sensors in each row.

2.4 Position Calculation

The position in Z can be determined from the amplitude of the magnetic field. The sum of the squares of the magnetic field sensed by sensors A, B, and C in Figure 2-2 is:

$$B_a^2 + B_b^2 + B_c^2 = 0.50B_r^2 e^{\frac{2z_r}{\lambda_c}} \left(\cos^2(\theta_a) + \cos^2\left(\theta_a + \frac{2\pi}{3}\right) + \cos^2\left(\theta_a + \frac{4\pi}{3}\right) \right) \quad 2-9$$

In equation 2-9, the common factors were factored out. Using the following trigonometric identity, equation 2-9 can be rewritten as equation 2-11.

$$\cos^2 \theta = \frac{1}{2} + \frac{\cos(2\theta)}{2} \quad 2-10$$

$$B_a^2 + B_b^2 + B_c^2 = 0.50B_r^2 e^{\frac{2z_r}{\lambda_c}} \left(\frac{3}{2} + \frac{\cos(2\theta_a)}{2} + \frac{\cos\left(2\theta_a + \frac{4\pi}{3}\right)}{2} + \frac{\cos\left(2\theta_a + \frac{8\pi}{3}\right)}{2} \right) \quad 2-11$$

Note that:

$$\cos\left(2\theta_a + \frac{8\pi}{3}\right) = \cos\left(2\theta_a + \frac{2\pi}{3}\right) \quad 2-12$$

Therefore, the cosine terms add up to zero, and the result is:

$$B_a^2 + B_b^2 + B_c^2 = 0.75B_r^2 e^{\frac{2z_r}{\lambda_c}} \quad 2-13$$

This equation can be rearranged for z_r , the vertical position of the sensor relative to the bottom of the magnet array.

$$z_r = \frac{\lambda_c}{2} \ln\left(\frac{1.32}{B_r^2} (B_a^2 + B_b^2 + B_c^2)\right) \quad 2-14$$

If z_a is the Z position of the sensor, the Z position of the magnet array, z_m , is equal to:

$$z_m = z_a - \frac{\lambda_c}{2} \ln\left(\frac{1.32}{B_r^2} (B_a^2 + B_b^2 + B_c^2)\right) \quad 2-15$$

To calculate the position in X, the magnetic field sensed by the three sensors is resolved into two vectors 90 degrees apart, B_x and B_y , as shown in Figure 2-4.

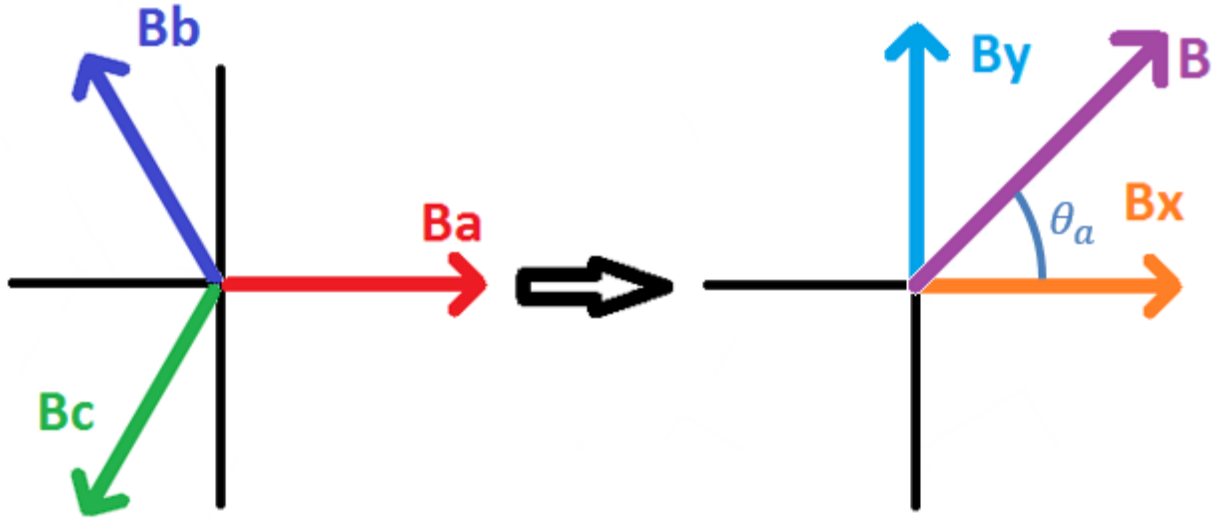


Figure 2-4 – Three sensor measurements resolved to two measurements 90 degrees apart

Equations 2-16 and 2-17 are used to calculate B_x and B_y . Then, the angle, as defined in equation 2-8, can be calculated by using arctangent function. As a result, the X position of the magnet array, x_m , is given by equation 2-18.

$$B_x = \sqrt{\frac{2}{3}} \left(B_a + \cos\left(-\frac{2\pi}{3}\right) B_b + \cos\left(\frac{2\pi}{3}\right) B_c \right) \quad 2-16$$

$$B_y = \sqrt{\frac{2}{3}} \left(-\sin\left(-\frac{2\pi}{3}\right) B_b - \sin\left(\frac{2\pi}{3}\right) B_c \right) \quad 2-17$$

$$x_m = x_a - \lambda_c \operatorname{atan}\left(\frac{B_y}{B_x}\right) \quad 2-18$$

Therefore, for a single X-oriented Halbach array, with periodicity aligned with X as in Figure 2-3, the position in 2-DOF, X and Z, can be calculated using three sensor column outputs. The sensor row outputs are unaffected by the presence of the Halbach array.

2.5 6-DOF Principle

The mover consists of four 1-D Halbach arrays: two X-oriented arrays, and two Y-oriented arrays.

The sensor column outputs are only sensitive to the X and Z position of the X-oriented Halbach arrays. The sensor row outputs are only sensitive to the Y and Z position of the Y-oriented Halbach arrays. Therefore, there is no interference between arrays oriented perpendicular to one another. Arrays oriented parallel to one another are spaced one λ apart (from edge to edge), such that the significant portion of the magnetic field does not overlap. The position of each array is therefore decoupled.

The position in two DOF for each Halbach array can be calculated, so there are eight measurements total. Specifically, there are two X measurements, two Y measurements, and four Z measurements. To calculate the six DOF for the mover, x_M , y_M , z_M , θ_X , θ_Y , and θ_Z , these eight measurements are used.

To calculate x_M , two X measurements are averaged. To calculate y_M , two Y measurements are averaged. To calculate z_M , the four Z measurements are averaged. To calculate θ_Z , the distance between the X position of two X-oriented Halbach arrays is used to calculate the angle. The same is done using the Y position for two Y-oriented Halbach arrays, and the two results are averaged. To calculate θ_X , the distance between the Z position of the Y-oriented Halbach arrays is used. To calculate θ_Y , the distance between the Z position of the X-oriented Halbach arrays is used.

2.6 Error Modelling

There are several sources of error for calculating position. Equations 2-19 through 2-34 show where they are introduced. The equations can be used to calculate or simulate the position error due to different sources.

B_{ra} , B_{rb} , and B_{rc} represent the true magnetic remanence, which may vary from what we expect it to be, B_r^* . Typically, B_{ra} , B_{rb} , and B_{rc} should be equal, but the magnetic remanence of the individual magnet pieces in the array may vary.

The sensor X positions x_a , x_b , and x_c may vary from the expected positions x_a^* , x_b^* , and x_c^* and may not be exactly $\lambda/3$ apart. As well, the sensor Z positions z_a , z_b , and z_c may vary from the expected positions z_a^* , z_b^* , and z_c^* , and therefore the vertical distances z_{ra} , z_{rb} , and z_{rc} between the sensors and magnet array may vary from the expected distance z_r^* . $B_{a,error}$, $B_{b,error}$, and $B_{c,error}$ may include external magnetic interference, magnetic field harmonics, edge effects, magnet array fabrication error, magnet array field strength variation, or other error in the

magnetic field. λ_c , the characteristic spatial wavelength of the magnet array, may vary from the expected characteristic spatial wavelength λ_c^* , if the geometry of the magnet array is different. Equations 2-19, 2-20, and 2-21 show the calculation of B_{az} , B_{bz} , and B_{cz} considering these sources of error.

$$B_{az} = 0.71B_{ra} \cos\left(\frac{x_a - x_m}{\lambda_c}\right) e^{\frac{z_{ra}}{\lambda_c}} + B_{a,error} \quad 2-19$$

$$B_{bz} = 0.71B_{rb} \cos\left(\frac{x_b - x_m}{\lambda_c}\right) e^{\frac{z_{rb}}{\lambda_c}} + B_{b,error} \quad 2-20$$

$$B_{cz} = 0.71B_{rc} \cos\left(\frac{x_c - x_m}{\lambda_c}\right) e^{\frac{z_{rc}}{\lambda_c}} + B_{c,error} \quad 2-21$$

The sensors may also be tilted slightly with angles ϕ_a , ϕ_b , and ϕ_c , resulting in reduced sensitivity to the vertical component B_z and increased sensitivity to the horizontal component B_x .

$$B_a = B_{az} \sin\phi_a + B_{ax} \cos\phi_a \quad 2-22$$

$$B_b = B_{bz} \sin\phi_b + B_{bx} \cos\phi_b \quad 2-23$$

$$B_c = B_{cz} \sin\phi_c + B_{cx} \cos\phi_c \quad 2-24$$

V_a , V_b , and V_c are the voltage measurements for each sensor. The sensor gains k_a , k_b , and k_c may vary from the expect gain k^* . As well, the gain could saturate at high magnetic fields. Similarly,

the current through the Hall elements I_a , I_b , and I_c may vary from the expected current I^* . As well, there may be offsets, $V_{a,offset}$, $V_{b,offset}$, and $V_{c,offset}$, and nonlinearities.

$$V_a = k_a I_a B_a + \sum_{i=2}^n k_{ai} I_a B_a^i + V_{a,offset} \quad 2-25$$

$$V_b = k_b I_b B_b + \sum_{i=2}^n k_{bi} I_b B_b^i + V_{b,offset} \quad 2-26$$

$$V_c = k_c I_c B_c + \sum_{i=2}^n k_{ci} I_c B_c^i + V_{c,offset} \quad 2-27$$

As a result of these errors, the magnetic field measurements B_a^* , B_b^* , and B_c^* may vary from the true Z component of the magnetic field, B_{az} , B_{bz} , and B_{cz} .

$$B_a^* = \frac{V_a}{k^* I^*} \quad 2-28$$

$$B_b^* = \frac{V_b}{k^* I^*} \quad 2-29$$

$$B_c^* = \frac{V_c}{k^* I^*} \quad 2-30$$

Equations 2-31 and 2-32 show the calculation of B_x and B_y using the magnetic field measurements including error.

$$B_x = \sqrt{\frac{2}{3}} \left(B_a^* + \cos\left(-\frac{2\pi}{3}\right) B_b^* + \cos\left(\frac{2\pi}{3}\right) B_c^* \right) \quad 2-31$$

$$B_y = \sqrt{\frac{2}{3}} \left(-\sin\left(-\frac{2\pi}{3}\right) B_b^* - \sin\left(\frac{2\pi}{3}\right) B_c^* \right) \quad 2-32$$

Including error, x_m^* and z_m^* are the resulting calculated X and Z magnet array position.

$$x_m^* = x_a^* - \lambda_c^* \operatorname{atan}\left(\frac{B_y}{B_x}\right) \quad 2-33$$

$$z_m^* = z_a^* - \frac{\lambda_c^*}{2} \ln\left(\frac{1.32}{B_r^{*2}} (B_a^{*2} + B_b^{*2} + B_c^{*2})\right) \quad 2-34$$

The effect of summing the Hall sensors is to average random error, reducing the error if the mean is zero. As well, further averaging occurs when the position of the mover in 6-DOF is calculated.

2.6.1 Magnetic Interference from Stator

A likely source of magnetic interference is magnetic field created by the stator coils themselves.

The strength of the magnetic field generated by current in an infinitely long wire is:

$$B = \frac{\mu_0 I}{2\pi R} \quad 2-35$$

Where μ_0 is the magnetic permeability of free space, I is the current in the wire, and R is the distance from the wire.

For example, a current of 20 A at a distance of 1 mm results in a magnetic field strength of 4 mT.

As shown in Figure 2-5, the direction of the magnetic field is tangential to a circle around the wire.

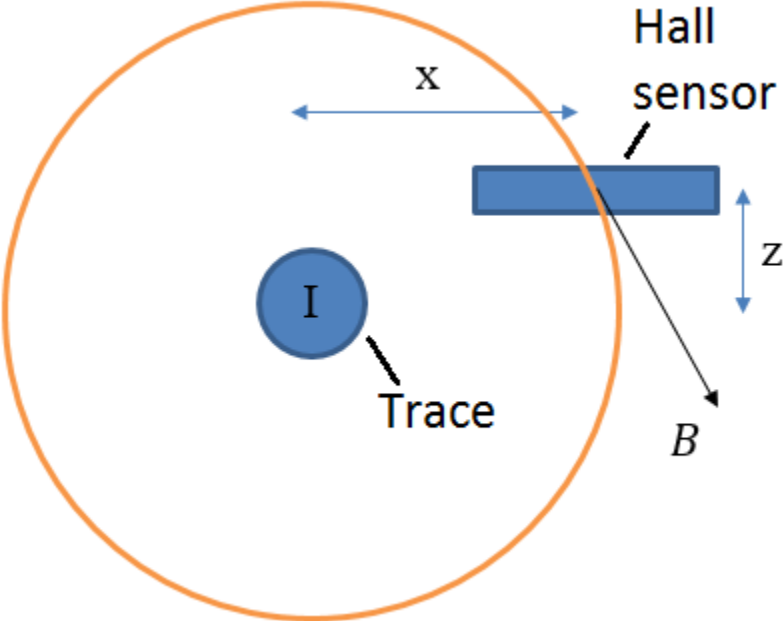


Figure 2-5 – Direction of magnetic field generated at Hall sensor location by stator trace

Therefore, directly above or below a trace in the stator, the magnetic field generated does not affect the Z component of the magnetic field measurable by the Hall sensor. For a trace offset in the X direction x mm from the sensor, the magnetic field component in Z is, assuming a vertical distance of 1 mm:

$$B_z = \frac{x}{\sqrt{(x^2 + 1)}} |B| \quad 2-36$$

For a current of 20 A at an X offset of between 1 and 5 mm, the magnetic field in Z is approximately 2 mT, and decreasing for larger offsets. This is not completely negligible after summing multiple traces, but is manageable and can be compensated because the current is controlled.

2.6.2 Magnetic Field Temperature Dependence

Temperature affects the output of the Hall sensors due to the temperature dependence of the Hall sensor gain, magnetic field strength, and resistor values used in the circuit. It is also possible the temperature could affect the position of the sensors or magnet geometry due to thermal expansion. The sensor gain temperature dependence depends on the sensor chosen, and the error due to sensor gain is discussed separately. Here the magnetic field temperature dependence is discussed.

The magnet has an intrinsic temperature coefficient. The magnet grade N45SH has a reversible temperature coefficient of induction, $\frac{\Delta B_r}{\Delta T}$, of -0.12%/°C [31]. If the magnet changes temperature uniformly, the effect will be a position error in Z due to the change in the magnetic field strength.

The magnetic remanence changes due to a temperature change ΔT in degrees Celsius as follows, assuming B_{ra} , B_{rb} , and B_{rc} are the same and equal to B_r .

$$B_r = B_r^*(1 - 0.0012\Delta T) \quad 2-37$$

If the expected and actual magnetic remanences are not equal, it can be shown that the error in Z is equal to:

$$e_z = z_m^* - z_m = -\lambda_c \ln\left(\frac{B_r}{B_r^*}\right) \quad 2-38$$

Combining these equations, the error in Z is equal to:

$$e_z = -\lambda_c \ln(1 - 0.0012\Delta T) \quad 2-39$$

For example, for a temperature change of 10°C, and $\lambda_c = \frac{30}{2\pi}$ mm, the error in Z is 0.058 mm. For a change of 50°C, the error is 0.30 mm. Note that $\ln(1 + \epsilon) \approx \epsilon$ for small ϵ . Therefore:

$$e_z \approx 0.0012\lambda_c\Delta T \quad 2-40$$

The error is linear with temperature, for small temperature changes.

2.6.3 Gain Error

Hall sensor gain can vary significantly, typically +/-15% to +/-30%. As well, the current source or voltage source may have error, which affects the gain as current-driven Hall sensor output depends on current and voltage-driven Hall sensors are typically ratiometric, which means the

output varies with the supply voltage. If the sensor gains k_a , k_b , and k_c vary from the expected gain k^* , the measured magnetic field will vary from the true magnetic field as follows:

$$B_a^* = \frac{k_a}{k^*} B_a \quad 2-41$$

$$B_b^* = \frac{k_b}{k^*} B_b \quad 2-42$$

$$B_c^* = \frac{k_c}{k^*} B_c \quad 2-43$$

If the gain varies +/- 10%, the worst case for X position error is when $k_a/k^* = 1.1$, $k_b/k^* = 1.1$, and $k_c/k^* = 0.9$. The worst case for Z position error is when $k_a/k^* = 0.9$, $k_b/k^* = 0.9$, and $k_c/k^* = 0.9$, but this is a DC error. For a position dependent error in Z, the worst case is when $k_a/k^* = 1.1$, $k_b/k^* = 1.1$, and $k_c/k^* = 0.9$, similar to the X position error.

The position dependent error is plotted in Figure 2-6.

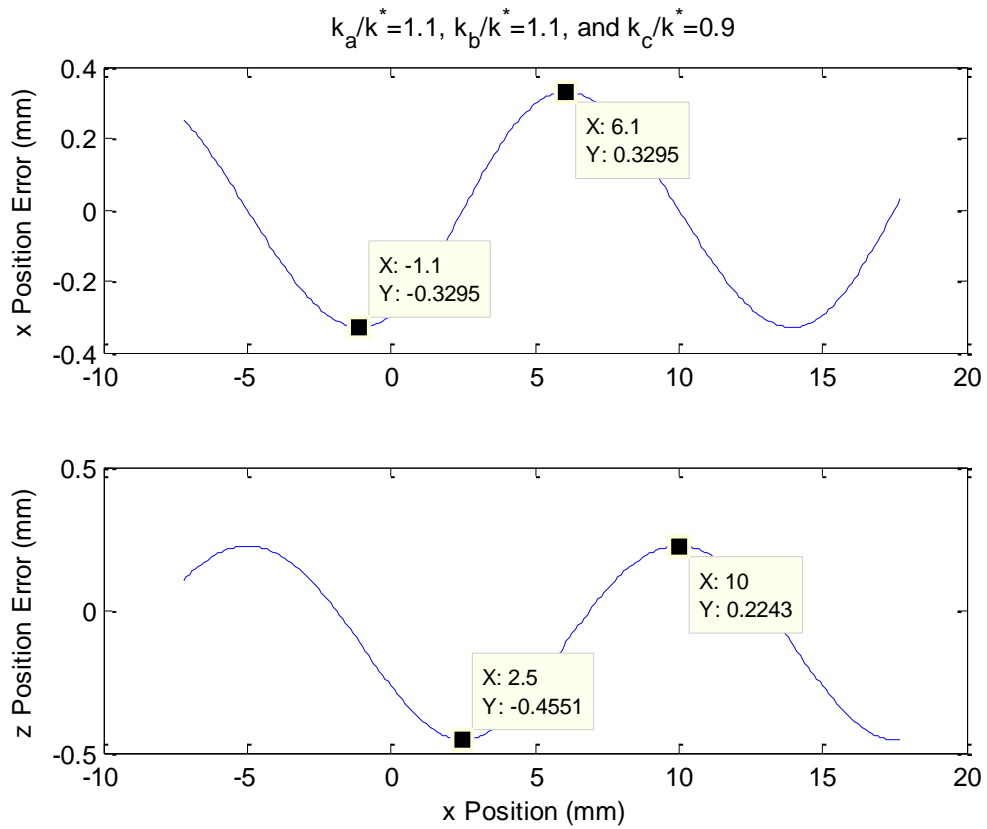


Figure 2-6 – Plot of maximum position error possible due to +/- 10% gain variation

The error in X is 0.66 mm peak-to-peak. The error in Z is 0.68 mm. Both errors have a spatial period of 15 mm.

Chapter 3: Prototype Design

The initial prototype used Analog Devices AD22151, a linear Hall sensor. A PCB was designed with an 8x12 array of sensors spaced 10 mm apart in both directions. The outputs of the sensors are summed over each row and column using a summing amplifier with an Analog Devices OP27. The sums are read by 4-channel Analog Devices AD7606-4 ADC's and processed by a Xilinx Spartan-6 FPGA for serial transfer to a computer.

3.1 Hall Effect Sensor Selection

The selection criteria for the Hall sensor to use for the prototype included: (1) integrated instrumentation for easy prototyping; (2) large magnetic range, ideally +/-1 T, to sense full magnetic field of magnet array; (3) uniform gain; (4) good linearity; (5) high bandwidth, several kHz; (6) compact sensor, to fit in an array with 10 mm spacing; and (7) minimal temperature dependence.

The AD22151 is a linear Hall sensor, combining a Hall element, current source, and instrumentation in a single 8-lead SOIC package. It operates on a 5 V supply. The gain is set at 0.4 mV/G, the lowest gain possible, in order to maximize the magnetic range. The gain error is +/- 1% over the temperature range of -40 to 150°C. The nonlinearity is 0.1% over the linear output range, which is from 10 to 90 % of the supply voltage, or 0.5 V to 4.5 V. The linear magnetic range is therefore +/- 0.5T, deemed sufficient for prototyping. The zero offset is 2.5 V. The 3 dB bandwidth is 5.7 kHz. The important specifications are listed in Table 3-1.

Table 3-1 – AD22151 sensor specifications

Gain	4 V/T
Gain Error	+/- 1%
Nonlinearity	0.1%
Linear range	+/- 0.5 T
3 dB Bandwidth	5.7 kHz
Package	5x6 mm 8-lead SOIC

The AD22151 has a built-in temperature sensor utilizing a thermistor. This can be used for compensation of temperature dependence of the Hall element, package induced stress, and magnetic field. An external resistor, R1 in Figure 3-1, acts as a voltage divider to complete the temperature compensation circuit and determines the amount of compensation depending on the temperature dependence of the magnetic field. See the datasheet for AD22151 for more information [32].

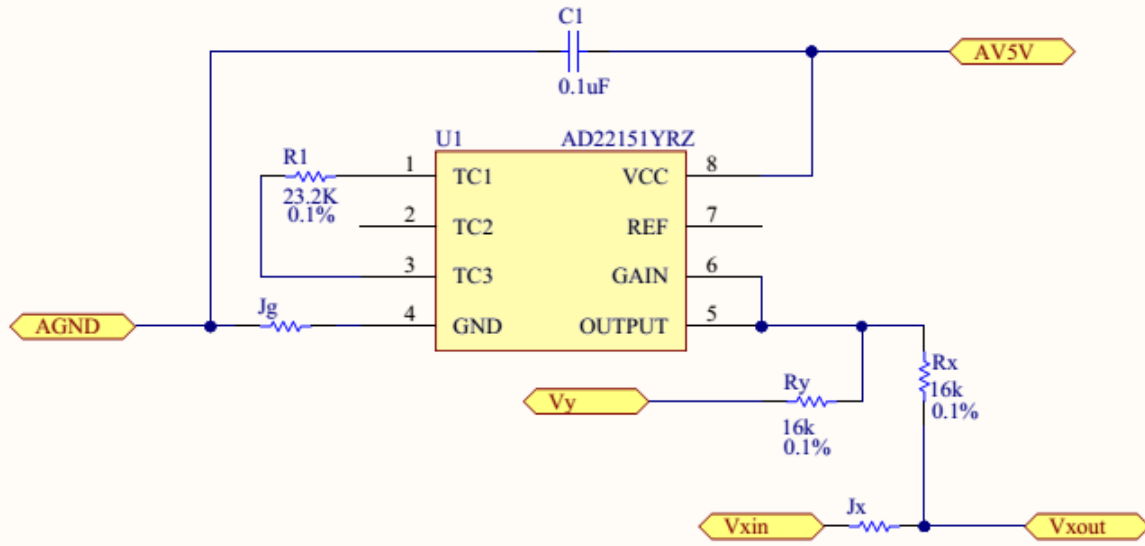


Figure 3-1 – AD22151 and external components

3.2 Summing Amplifier

The schematic for the summing amplifier for a single column of a 3x3 Hall sensor array is shown in Figure 3-2.

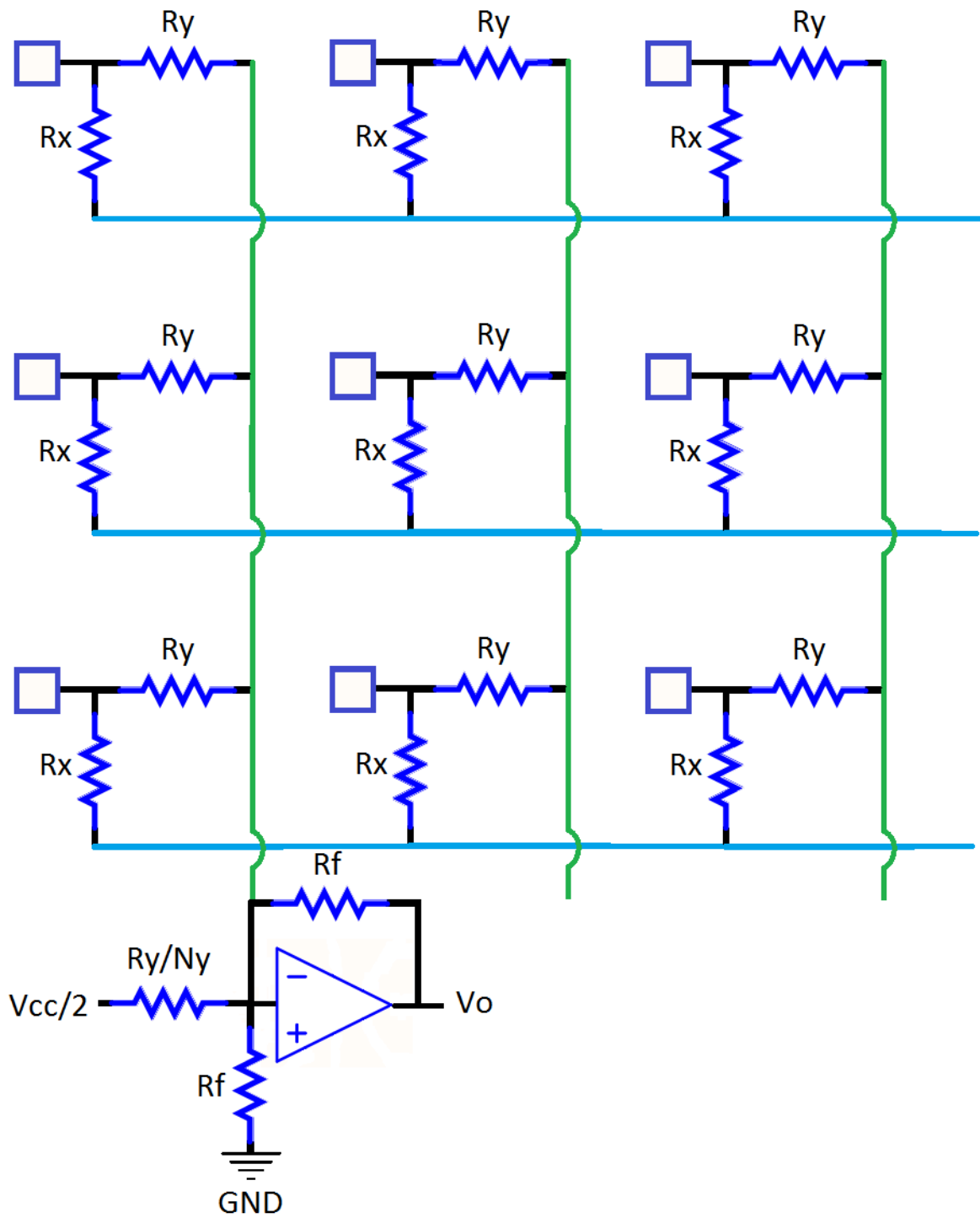


Figure 3-2 – 3x3 Hall sensor array with summing amplifier for one column

Equation 3-1 can be used to calculate the output voltage of the summing amplifier for a column with N_y sensors. R_f and R_y are resistor values shown in Figure 3-2. V_{cc} is the Hall sensor supply voltage. V_{ok} is the output voltage of the k^{th} Hall sensor. The output voltage of the summing amplifier for a row is similar, with R_x and N_x substituted for R_y and N_y .

$$V_o = \frac{R_f}{R_y} \sum_{k=1}^{N_y} \left(\frac{V_{cc}}{2} - V_{ok} \right) \quad 3-1$$

3.3 PCB Layout

The PCB layout was designed using multi-channel design in Altium Designer, which allows the layout for each 10 mm by 10 mm cell to be patterned for each sensor, while maintaining the netlist for a nested schematic.

Electroless nickel immersion gold surface plating was used for a flat surface to ensure the positional accuracy of the sensors. During reflow soldering, the sensors will float on the molten solder. The surface tension of the leaded solder will pull the sensor into position. The pads for the sensor were designed with minimal clearance so the final position of the sensor is deterministic.

Each column of eight Hall sensors is connected by a supply voltage trace and ground trace. Power and ground planes are not used because the large moving magnet (the mover) above the PCB will result in an induced voltage in the supply voltage and ground. The supply voltage trace

and ground trace are routed next to each other to minimize the area and therefore induced voltage.

The output of the AD22151 is ratiometric to the supply voltage. Therefore, for a uniform gain for all sensors, the voltage supplied to each sensor must be uniform. The resistive voltage drop along the supply voltage and ground traces is minimized by maximizing the trace width.

The prototype PCB is shown in Figure 3-3.

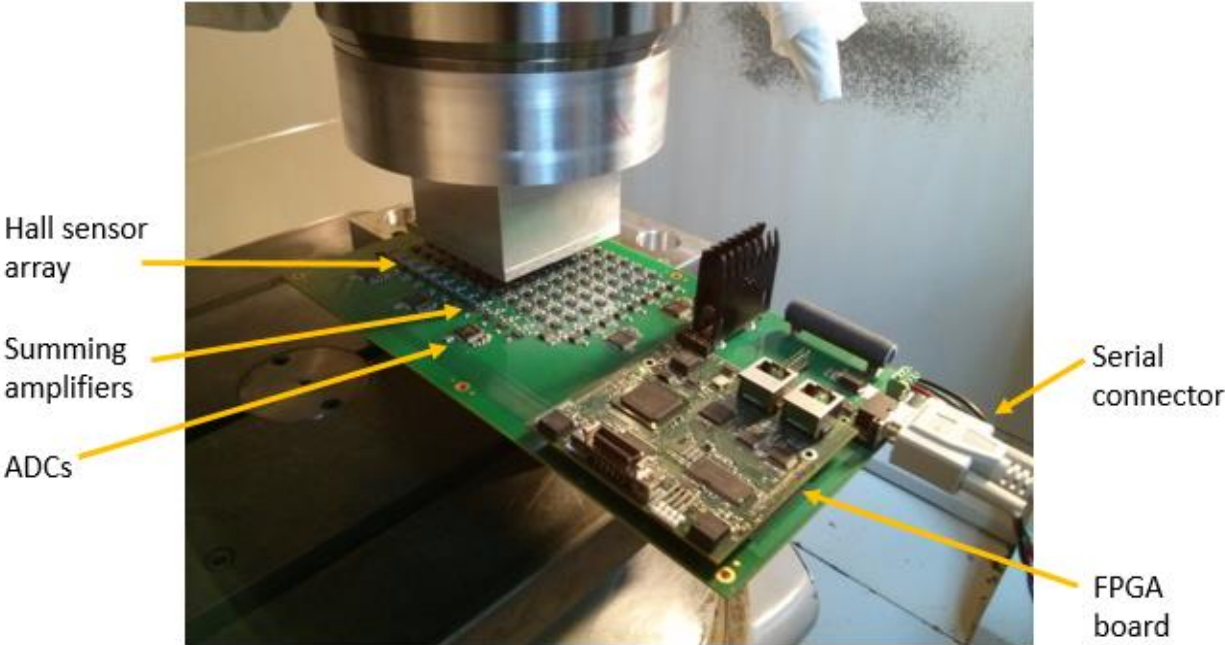


Figure 3-3 – Hall sensor array prototype (fixed to CNC table for testing)

Chapter 4: Experiment

The prototype was tested using a CNC machine to move the magnet array to discrete locations in X, Y, and Z.

4.1 Experiment Set Up

The experiment set up is shown in Figure 4-1.

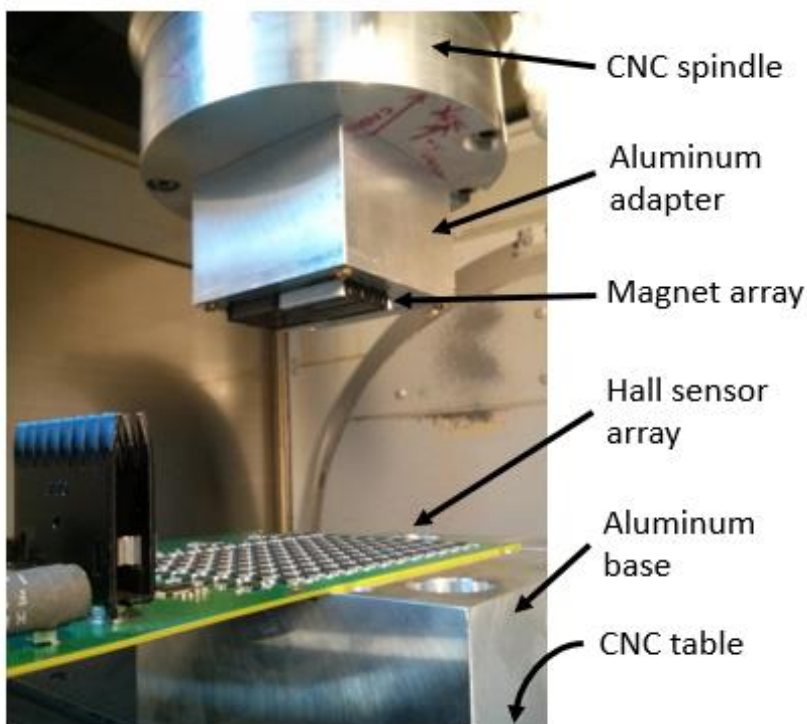


Figure 4-1 – Prototype fixed to CNC table with magnet array positioned using CNC spindle

The PCB was bonded with epoxy on an aluminum base machined to have a flat top surface parallel to the bottom surface and perpendicular to the side surfaces. The base was high enough to ensure no distortion of the magnetic field by the steel CNC table. The PCB was oriented on

the aluminum base by pushing the edge of the PCB against dowel pins inserted into precisely located holes.

The magnet array tested was 2λ long by 2λ wide. An aluminum spacer was placed between the magnet array and the steel spindle, in order to avoid distorting the magnetic field. The top and side surfaces of the aluminum PCB base were used as references to orientate the magnet array. Specifically, a dial gauge was mounted on the CNC spindle and ran along the sides of the aluminum block, before bolting the aluminum block to the CNC work table. Shims were used to measure the distance between the bottom of the magnet array and the top of sensors.

This test was unable to measure effects of a moving magnet such as eddy current and inductive loops. These effects will be explored in future work.

The CNC machine used for the test is a Mori Seiki NMV5000. The CNC position error is expected to be less than $10\ \mu\text{m}$ and the resolution is $1\ \mu\text{m}$.

4.2 Experiment Results

The error in X and Z is shown in Figure 4-2 for a sweep of discrete, stationary points in X.

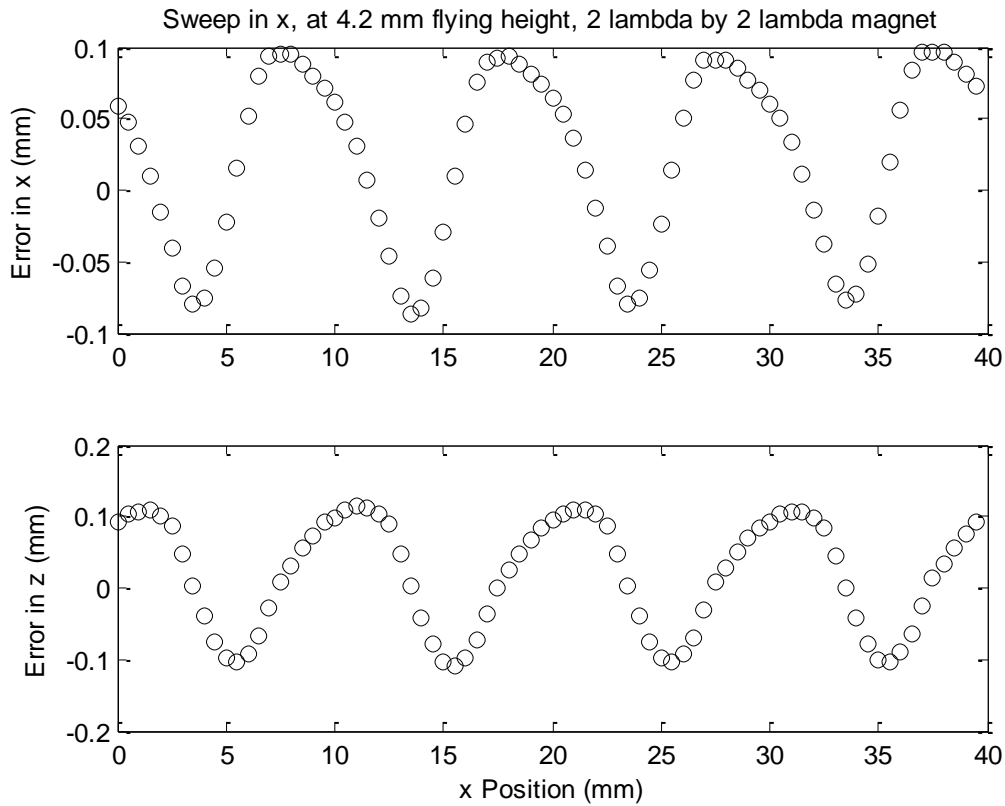


Figure 4-2 – Error in X and Z for sweep in X at 4.2 mm flying height

This is for a 2λ by 2λ magnet array. The height is approximately 4.2 mm from the top of the sensor package to the bottom of the magnet array. The distance from the top of the sensor package to the sensor die is 0.51 to 0.64 mm (per correspondence with Analog Devices). For all of the following plots, the error is manually centred around zero, because a DC error can be easily compensated. The error in X is less than 200 μm peak to peak. The error in Z is approximately 200 μm . Both errors have a period of 10 mm and are mostly independent of position relative to the sensor array (greater than the period of 10 mm). The error is likely due to

fabrication error of the magnet array and variation in the magnetic strength, resulting in harmonics not expected for an ideal four-segment-per-period Halbach array. This error is likely not due to gain variation in the Hall sensors because the Hall sensors have a gain error of +/-1%.

The test is repeated to show the repeatability. The error for two runs is shown in Figure 4-3.

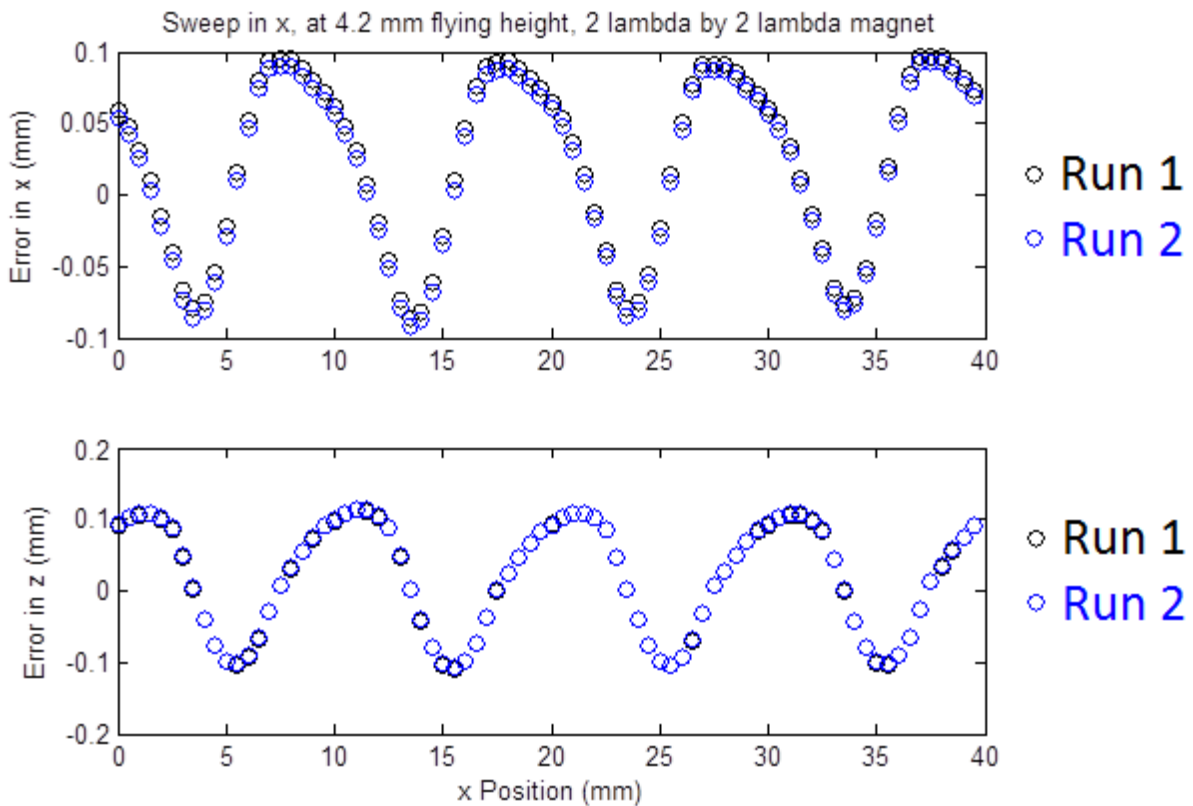


Figure 4-3 – Error in X and Z for two sweeps in X to show repeatability

The repeatability is approximately 5 μm in X and 2 μm in Z. This shows that the repeatable, periodic position error can be compensated.

The voltage output of a decoupled sensor row is shown in Figure 4-4 for the same sweep in X.

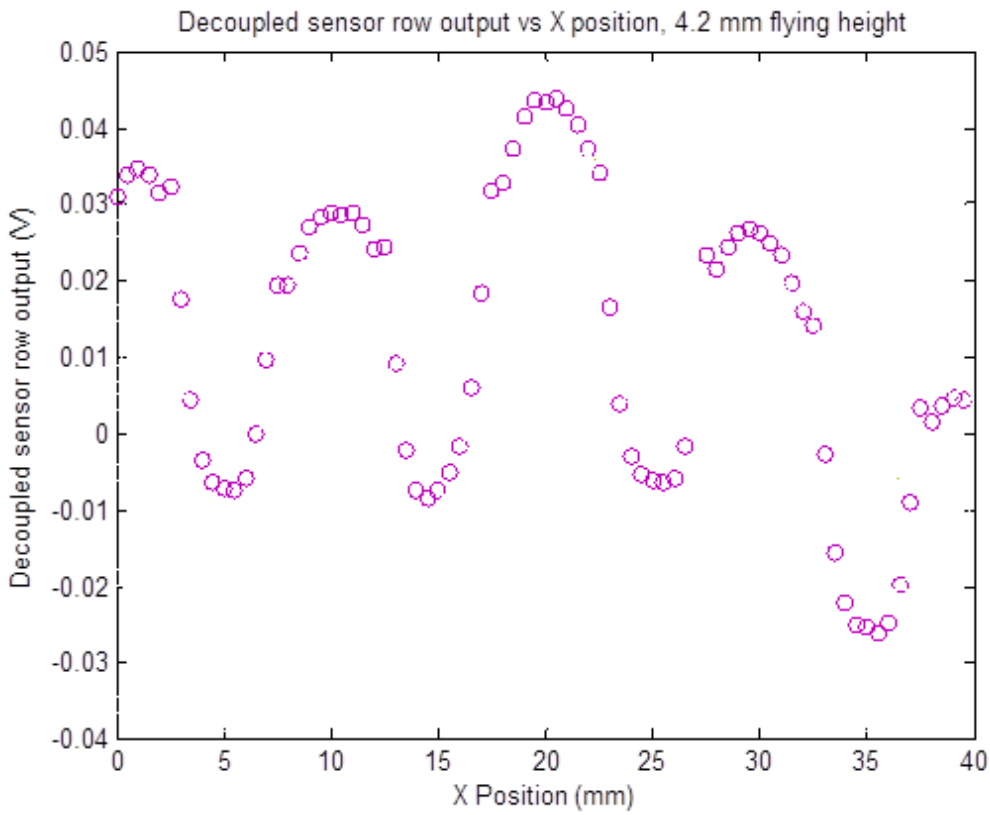


Figure 4-4 – Voltage output for decoupled sensor row during sweep in X

The maximum voltage is less than 50 mV. This is less than 1% of the voltage range. The other sensor rows have similar or lower voltage outputs.

At a height of 5.2 mm, the error is slightly less, because the magnetic field harmonics are weaker at a greater distance. The error is plotted in Figure 4-5.

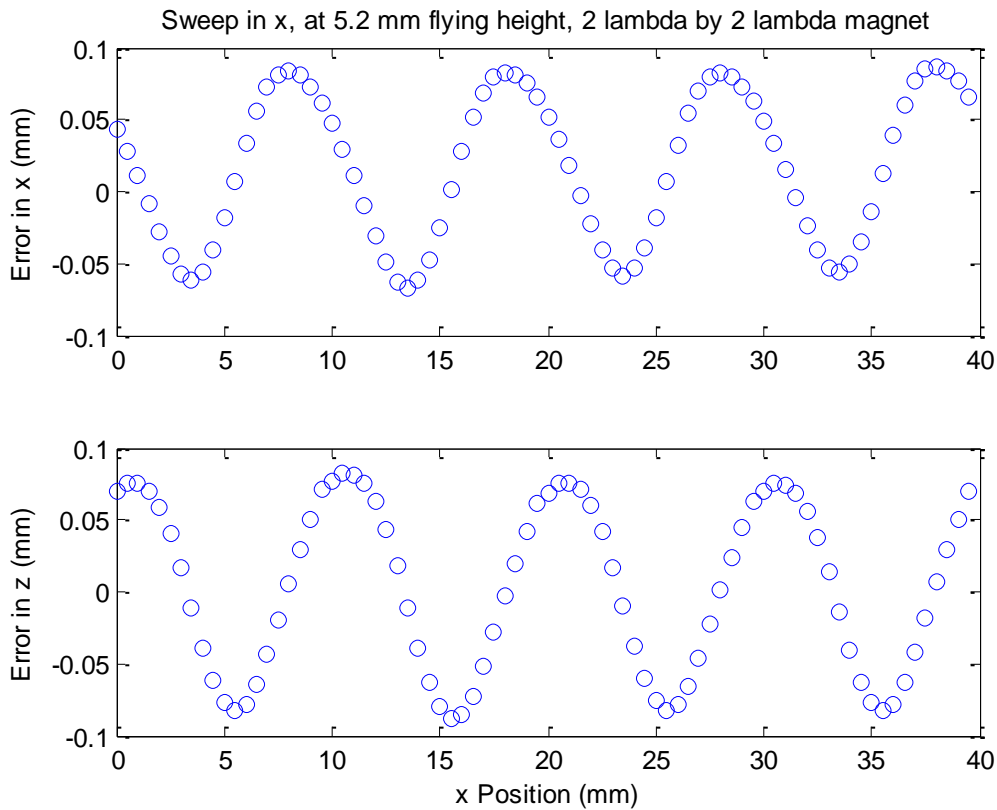


Figure 4-5 – Error in X and Z for sweep in X at 5.2 mm flying height

The error is also more sinusoidal. This is likely due to the same reason. The error in X is approximately 150 μm . The error in Z is also approximately 150 μm .

The measured X position and Z position is mostly insensitive to the magnet array Y position, as shown in Figure 4-6.

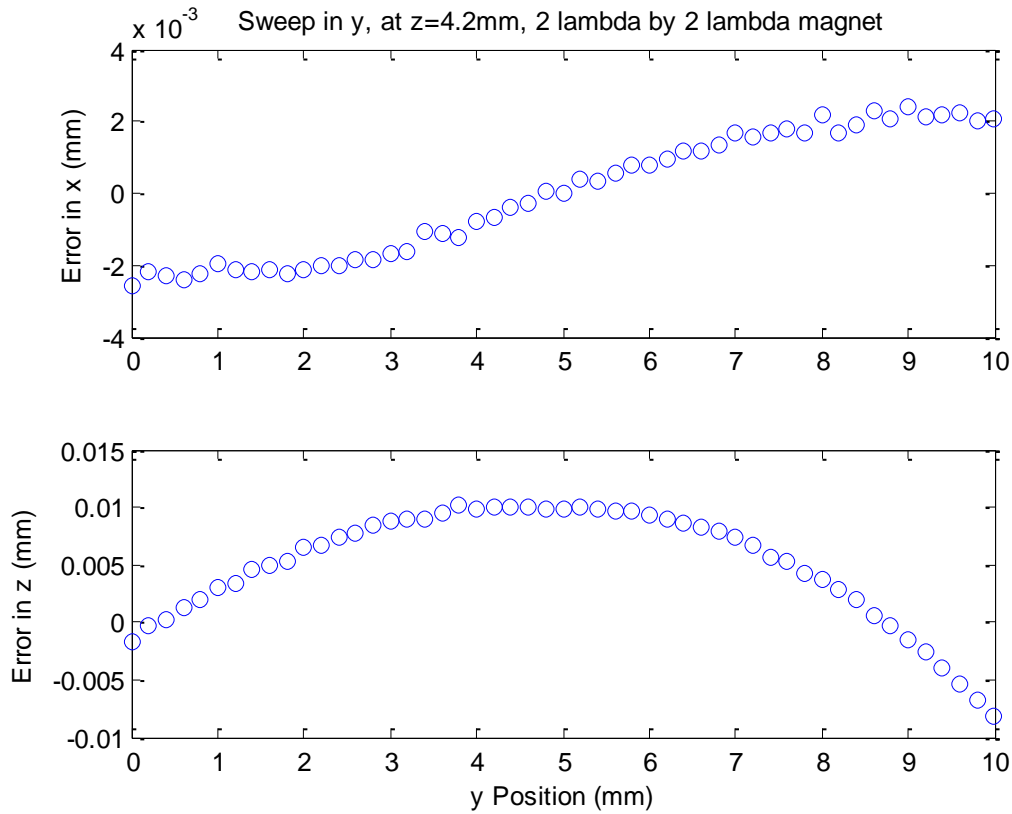


Figure 4-6 – Error in X and Z for sweep in Y at 4.2 mm flying height

For a 10 mm sweep in Y, the X position varies approximately 4 μm . The measured Z position varies approximately 20 μm . The error may be due to misalignment in the experimental set up, or variation in the sensor gain or sensor position.

For a sweep in Z, there is significant error below a height of 4 mm, as shown in Figure 4-7.

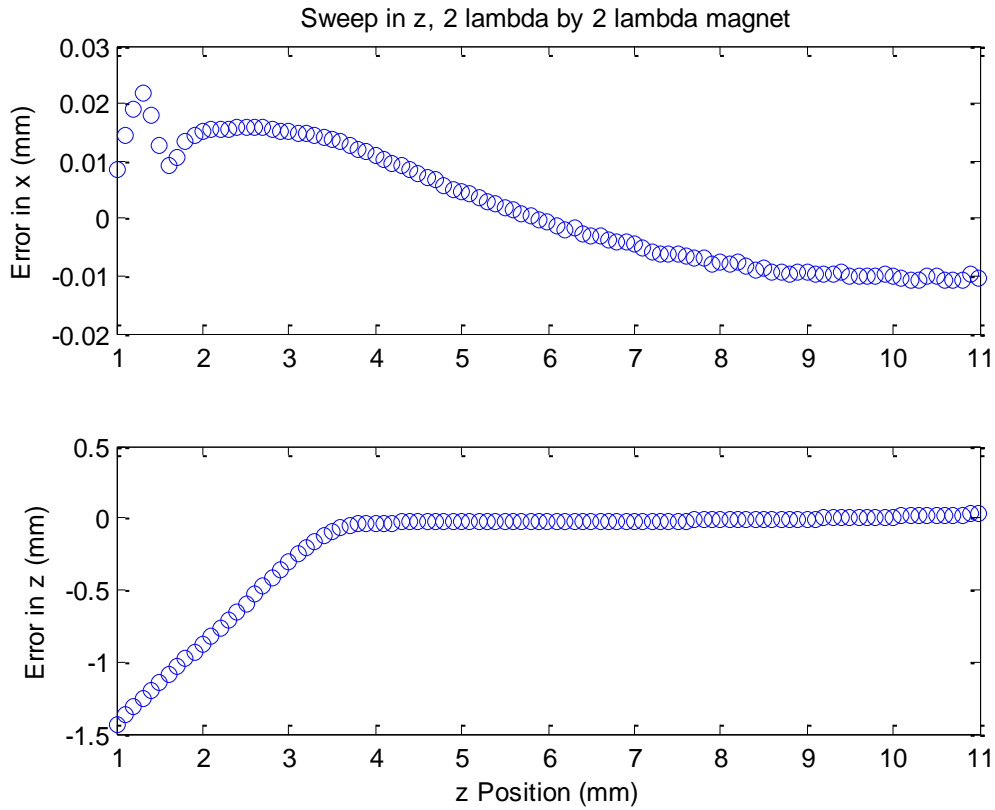


Figure 4-7 – Error in X and Z for sweep in Z, showing saturation

The significant error below 4 mm is because the sensor is saturating as the magnetic field exceeds the magnetic range of the sensor. A sensor array using a Hall sensor with a larger magnetic range will be used for future work.

The error in X and Z is plotted in Figure 4-8 for a sweep in Z above 4 mm height.

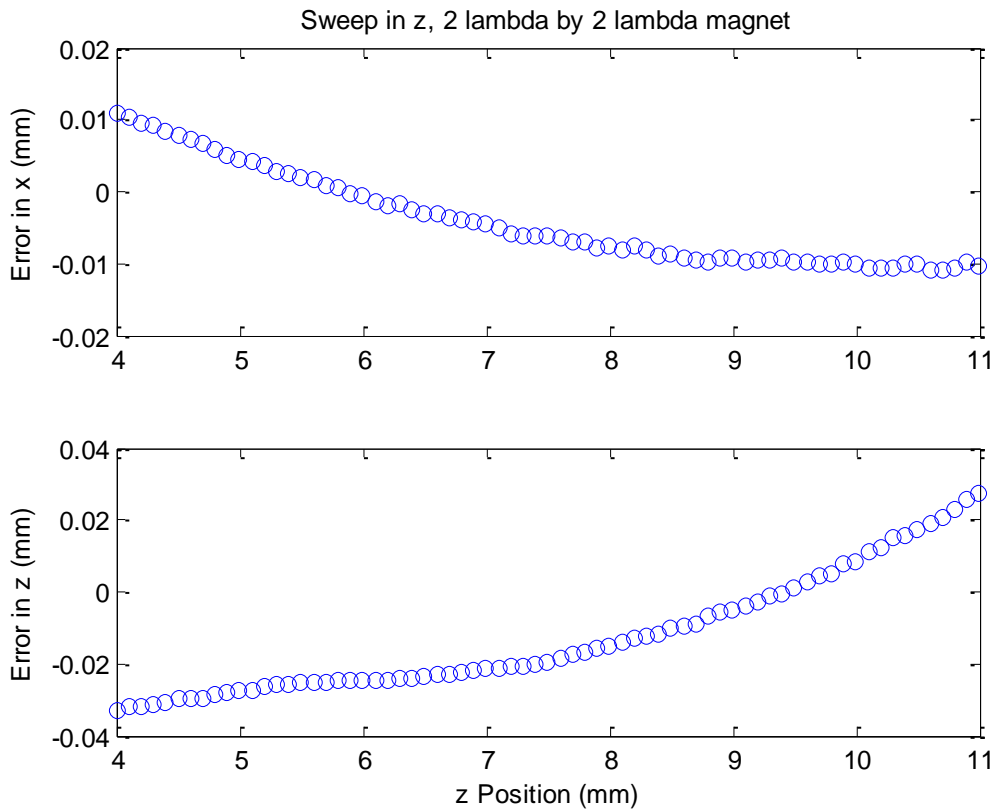


Figure 4-8 – Error in X and Z for sweep in Z

Over 7 mm in Z, the measured X position varies 20 μm , and the measured Z position varies 60 μm . The variation in error is likely due to decay of magnetic harmonics.

At each location, 20 voltage measurements were recorded for each row and column output. By calculating position with each of the 20 measurements, we can estimate the position resolution of the sensor. This is for a flying height of 5.2 mm where the signal-to-noise ratio is lower and hence the resolution is worse. The variation in X position for 20 measurements is plotted in Figure 4-9. For X, the position resolution is approximately 5 μm .

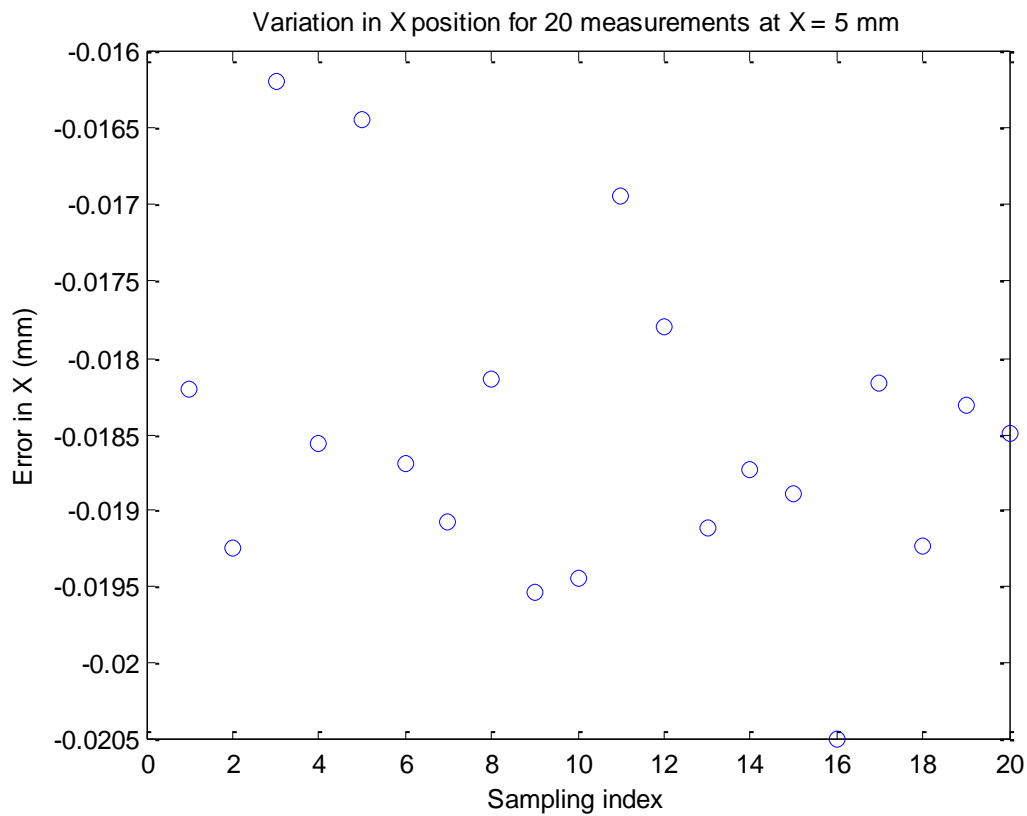


Figure 4-9 – Variation in X position for 20 measurements to show X position resolution

The variation in Z position for 20 measurements is plotted in Figure 4-10. For Z, the position resolution is approximately 4 μm .

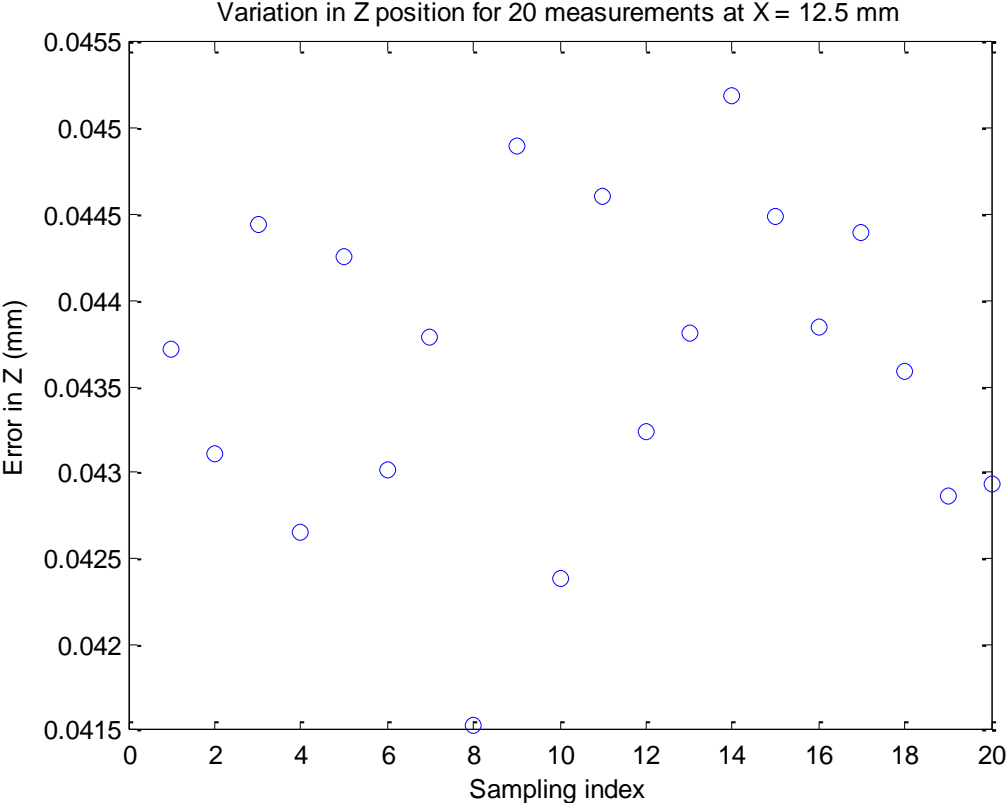


Figure 4-10 – Variation in Z position for 20 measurements to show Z position resolution

Chapter 5: Sensor Sorting

5.1 Motivation

Previous research using Hall sensor arrays for position sensing, not including the prototype in this thesis, resulted in significant error due to Hall sensor gain variation. This was demonstrated in Section 2.6.3. Many commercially available Hall elements have a large sensor gain variation, typically +/- 15% to +/- 30%. Using summing amplifiers makes it difficult to calibrate the sensors, because the gain of each individual sensor is not adjustable, and the output of each individual sensor is not provided. Frissen and Compter used individual differential amplifiers for each sensor so as to vary the gain. A calibration scheme such as the error-mapping technique done by Kawato and W.-J. Kim can also be used to account for the resulting error in position. The experiment results in Section 4.2 demonstrate that the position error can be reduced using sensors with a uniform gain.

Instead of individual differential amplifiers or error-mapping techniques, the sensors can be sorted based on gain, and sensors with a uniform gain used together in batches. The gain for an entire batch can be varied simultaneously, whether in hardware or software. The gain of the sensor can be determined by exposing the sensor to two known magnetic reference fields as shown in Figure 5-1, assuming a linear relationship. One of the known magnetic fields can also be a zero field.

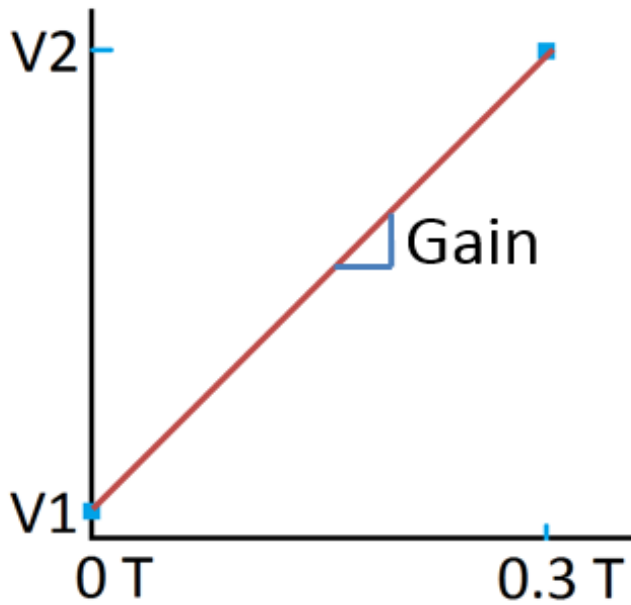


Figure 5-1 – Gain determined by sampling the sensor voltage in two known magnetic reference fields

A set up utilizing this principle was designed and built to sort more than twelve thousand Hall sensors with +/- 15% gain error. These are more compact, lower cost sensors than the AD22151 sensor, allowing a thinner and lower cost Hall sensor array to be built.

5.2 Test Circuit Design

A printed circuit board was designed for sampling the Hall sensor while inside the known magnetic reference fields.

A non-magnetic sensor socket allows the sensor to be temporarily held in place and electrically connected to the circuit. It uses a clamshell lid and spring pins to connect between the sensor pads and the PCB. The sensor is driven with a 3-mA constant current source. The differential output of the sensor to be sorted is connected to an instrument amplifier (Texas Instruments INA826) with a gain of 35.

In series with the sensor to be sorted are multiple non-sorted sensors. A second instrument amplifier can be connected with wires to one of the non-sorted sensors as a reference sensor during sorting. The software can check the value of the reference sensor to ensure the sensor is located in the correct location in the magnetic field. Since the reference sensor is located where the magnetic field is less uniform than the sensor to be sorted, it is more sensitive to positional error.

The outputs of the INA's are connected by two cables to a dSPACE for recording the sensor outputs.

The PCB was mounted on an aluminum PCB base, which the user holds and inserts into the magnetic field. The socket, PCB, and PCB base are shown in Figure 5-2.

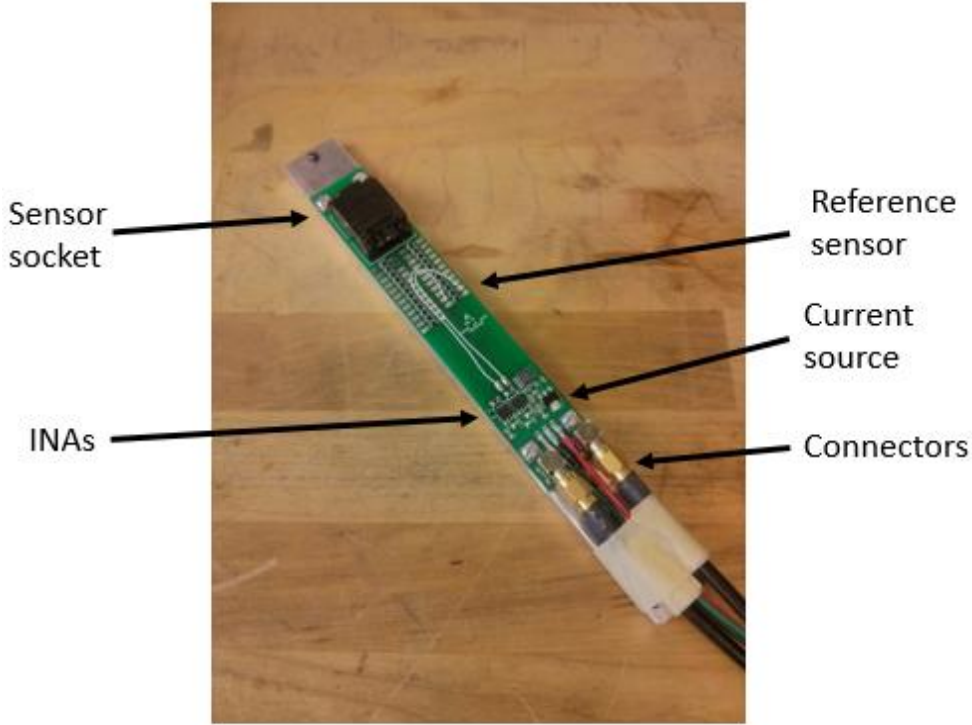


Figure 5-2 – Sensor sorting PCB attached to aluminum base

5.3 Zero Magnetic Reference Field

Mu-metal was wrapped around a plastic tube, as shown in Figure 5-3, to attenuate a magnetic field inside the tube in the radial direction.



Figure 5-3 – Zero magnetic reference field consisting of mu-metal wrapped around a plastic tube

Mu-metal has a high permeability making it a suitable magnetic shield. Gauss meter measurements were made near a magnet source with and without a shielded tube. Without shielding, the magnetic field was 0.5 mT. With mu-metal shielding, the magnetic field was 0.07 mT. This is approximately 0.2% of the magnetic range used for calculating gain. This

demonstrates that the mu-metal will attenuate magnetic interference to maintain a stable reference field. However, care is still needed to ensure a large magnet is not placed too close.

5.4 Magnetic Reference Field

For the known magnetic field, a strong, uniform, stable magnetic field was desired. A permanent magnet source was designed as a reference field. An electromagnet was not used as a cooling system would need to be implemented and care would be needed to ensure a stable temperature. A fluctuating temperature could change the geometry of the electromagnet and affect the strength of the magnetic field.

5.4.1 Design

A magnetic circuit consisting of permanent magnets, steel yokes, and an air gap was designed. The socket containing the sensor is inserted into an aluminum receptacle in the air gap, and the air gap was set as 1.5” tall, to allow space for the aluminum receptacle.

Different magnetic circuits were considered and compared using Finite Element Method Magnetics (FEMM) [33] and then the geometry of the final magnetic circuit was optimized using COMSOL Multiphysics [34], constrained by off-the-shelf magnet sizes. Typical hand calculation methods were inadequate since the large air gap results in significant leakage. One would need to consider all the leakage paths.

FEMM is a 2-D finite element electromagnetic software suite. Results can be obtained quickly, and it is useful for comparing different geometries, but the results are less accurate than a 3-D program, as leakage paths out of plane are not considered.

The AC/DC Module of COMSOL Multiphysics is useful for 3-D finite element electromagnetic problems. Being 3-D, it is more computationally intensive than FEMM, but results in a more accurate solution and considers leakage in all directions. For example, the magnetic field for the magnetic circuit shown in Figure 5-4 is not identical for varying circuit thicknesses out of plane, but the results in FEMM are the same.

The most promising configurations considered were the following:

a) magnet-opposite-gap (Figure 5-4)

b) magnet-near-gap (Figure 5-6)

Both configurations consists of permanent magnets, yokes, and a gap. The magnetic flux in the magnet-opposite-gap configuration begins at the permanent magnets, passes through the first yoke, the gap, and the second yoke in sequence, then returns to the permanent magnets. The magnetic flux in the magnet-near-gap configuration passes from the first magnet through the gap to the second magnet, and returns from the second magnet through the yoke to the first magnet.

Figure 5-4 through Figure 5-9 are obtained using FEMM. For the FEMM simulations, the yokes are a fictional high-permeability material.

The magnet-opposite-gap configuration has the advantage of a more uniform magnetic field in the gap due to the yokes. The magnetic flux lines are shown in Figure 5-4, and the magnetic flux density distribution is shown in Figure 5-5. The magnetic flux density in the middle of the gap is 0.475 T. From -5 to 5 mm in a horizontal line, the normal magnetic flux density varies 0.05%.

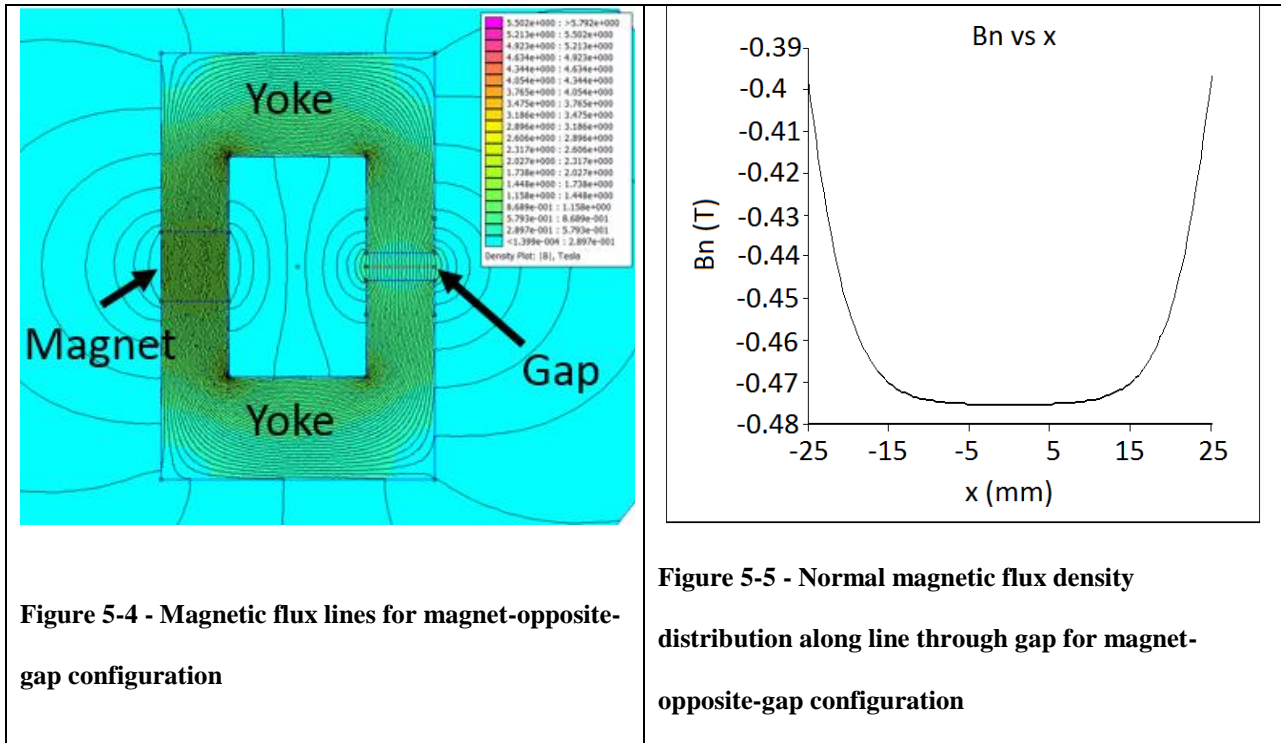


Figure 5-4 - Magnetic flux lines for magnet-opposite-gap configuration

Figure 5-5 - Normal magnetic flux density distribution along line through gap for magnet-opposite-gap configuration

The magnet-near-gap configuration has the advantage of a stronger magnetic field in the gap. The magnetic flux lines are shown in Figure 5-6, and the magnetic flux density distribution is shown in Figure 5-7. The magnetic flux density in the middle of the gap is 0.937 T. From -5 to 5 mm in a horizontal line, the normal magnetic flux density varies 1%.

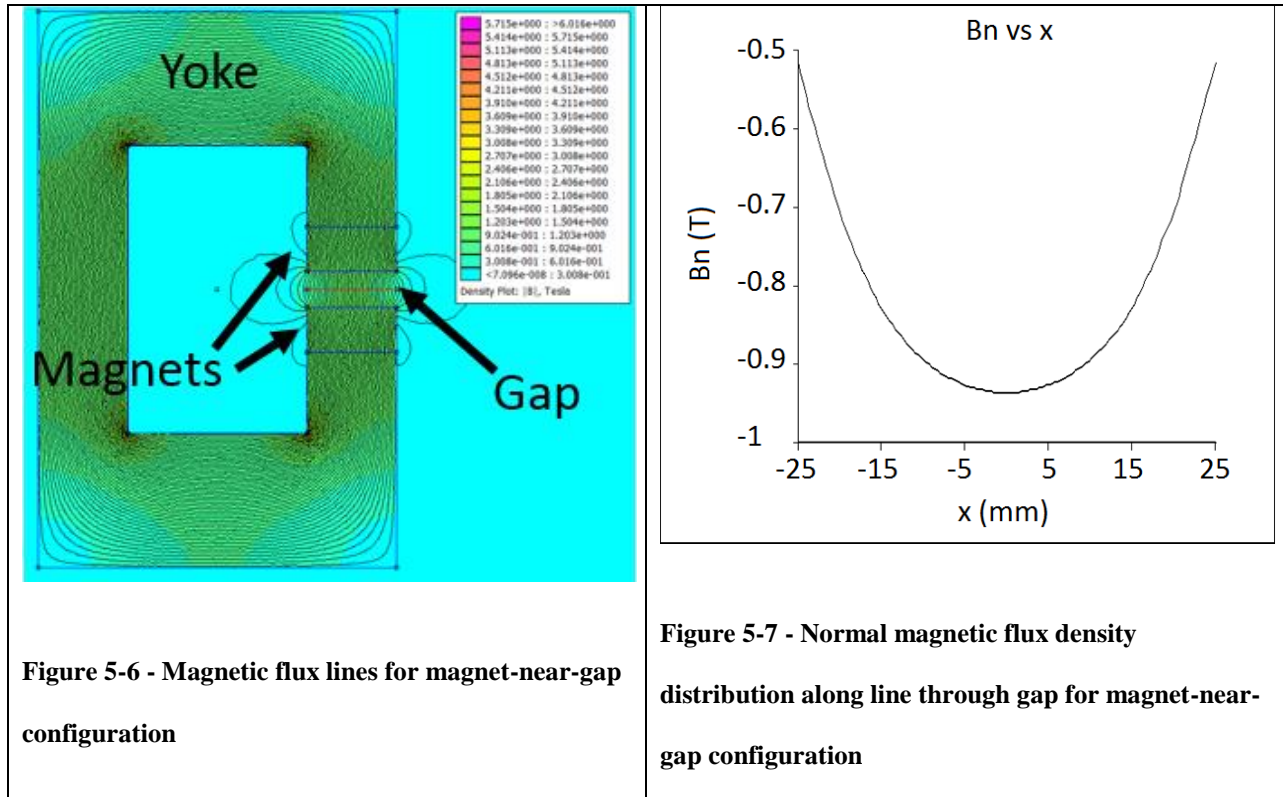


Figure 5-6 - Magnetic flux lines for magnet-near-gap configuration

Figure 5-7 - Normal magnetic flux density distribution along line through gap for magnet-near-gap configuration

The difference in magnetic field strength is due to leakage, which is ignored in a simple hand calculation. The magnet-opposite-gap configuration results in two prominent leakage paths, one around the magnet, and one around the gap. The magnet-near-gap configuration only has a single prominent leakage path around the gap.

High-permeability sheets inserted gap-side for the magnet-near-gap configuration resulted in a more uniform field and yet still maintained a stronger magnetic field than the magnet-opposite-gap configuration. The geometry and magnetic flux lines are shown in Figure 5-8. The magnetic flux density distribution is shown in Figure 5-9. The magnetic flux density in the middle of the gap is 0.752 T. From -5 to 5 mm in a horizontal line, the normal magnetic flux density varies 0.04%.

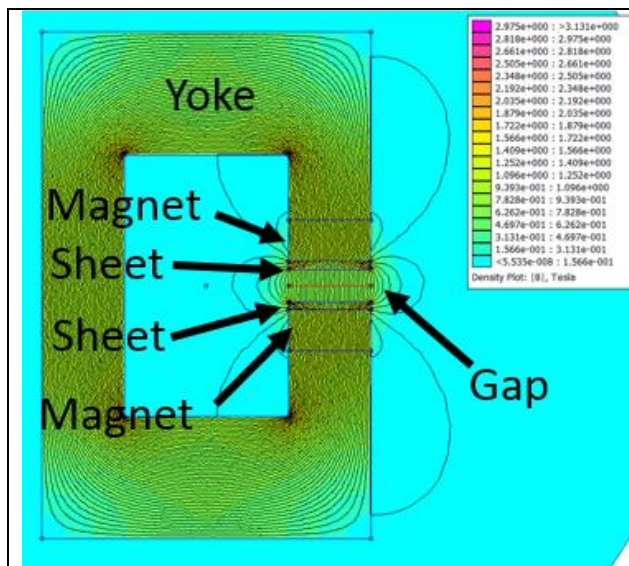


Figure 5-8 - Magnetic flux lines for magnet-near-gap configuration with high-permeability sheets

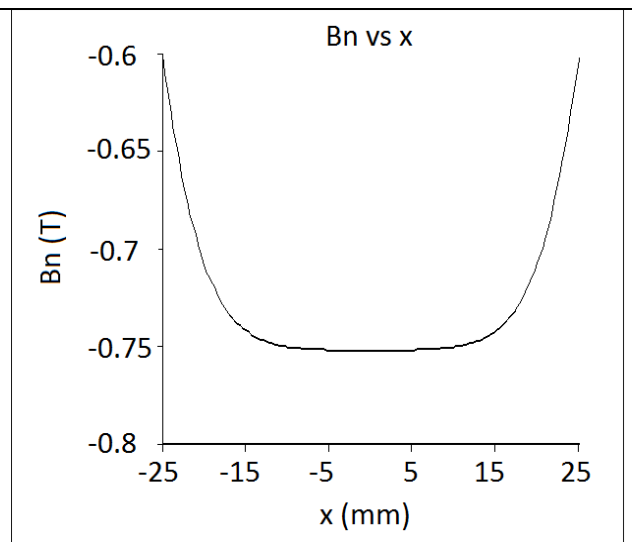


Figure 5-9 - Normal magnetic flux density distribution along line through gap for magnet-near-gap configuration with high-permeability sheets

In the end, the magnet-opposite-gap configuration was chosen due to the superior magnetic field uniformity and because assembly was expected to be easier. The geometry was optimized in COMSOL, varying dimensions of the steel yokes, while constrained by off-the-shelf magnet

sizes. The intent was to maximize the magnetic field strength and uniformity, while maintaining a reasonable cost for materials and machining. 1018 steel and two 4"x3"x1" N42 magnets were used. The COMSOL model geometry is shown in Figure 5-10.

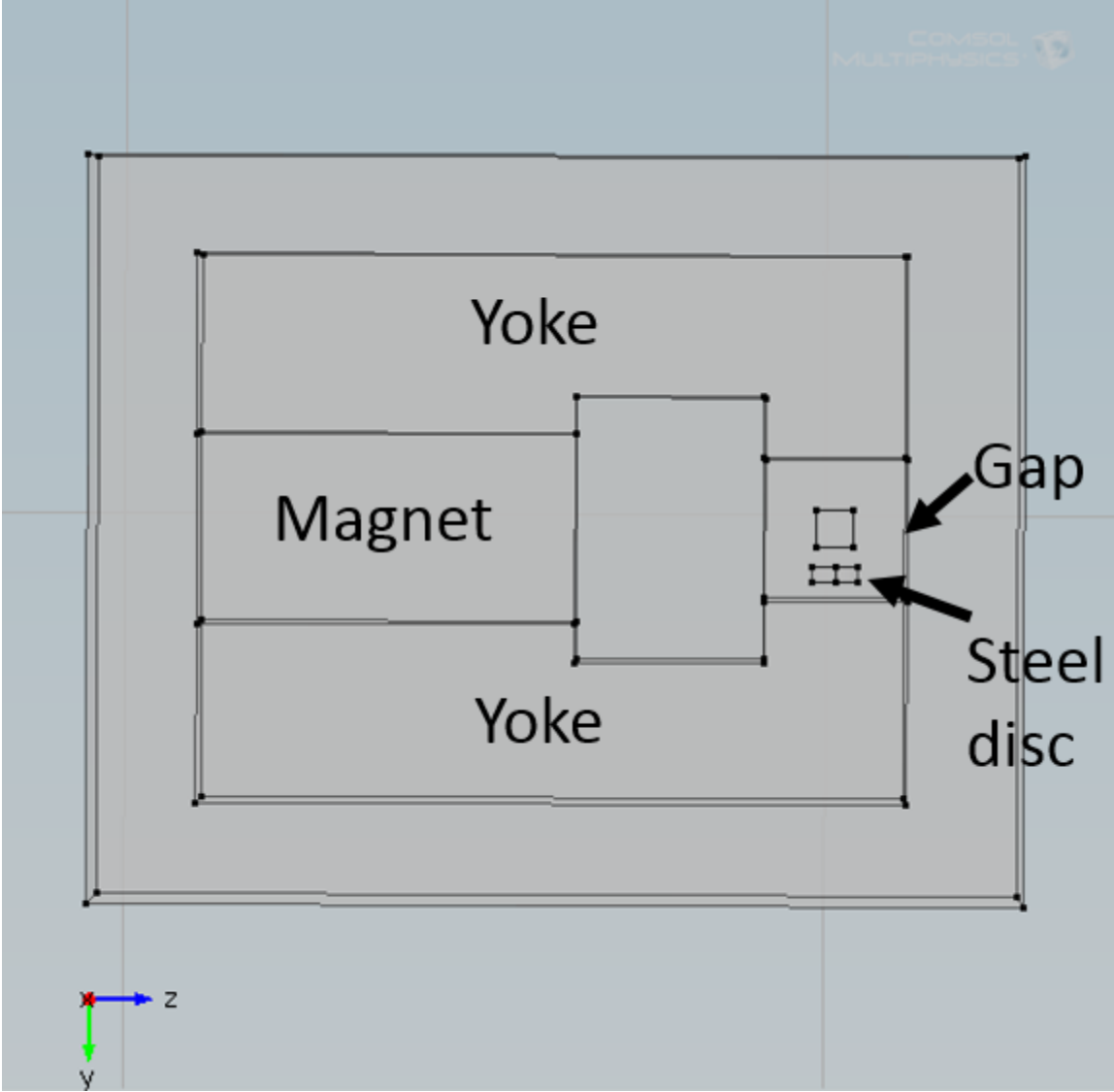


Figure 5-10 - COMSOL model of magnetic field source

A steel disc, 12 mm diameter and 4 mm thick, was included in the COMSOL model, to be embedded in the socket assembly. This served two purposes: 1) it created a preload for the

kinematic coupling as explained later, and 2) it resulted in a magnetic field strength at the sensor location which is less sensitive to the position of the socket assembly.

Figure 5-11, Figure 5-12, and Figure 5-13 show the strength of the vertical component of the magnetic field near the centre of the gap, where the sensor is located, along X, Y, and Z respectively. For these plots, the steel disc is fixed relative to the magnet assembly. Note that the Y direction is vertical.

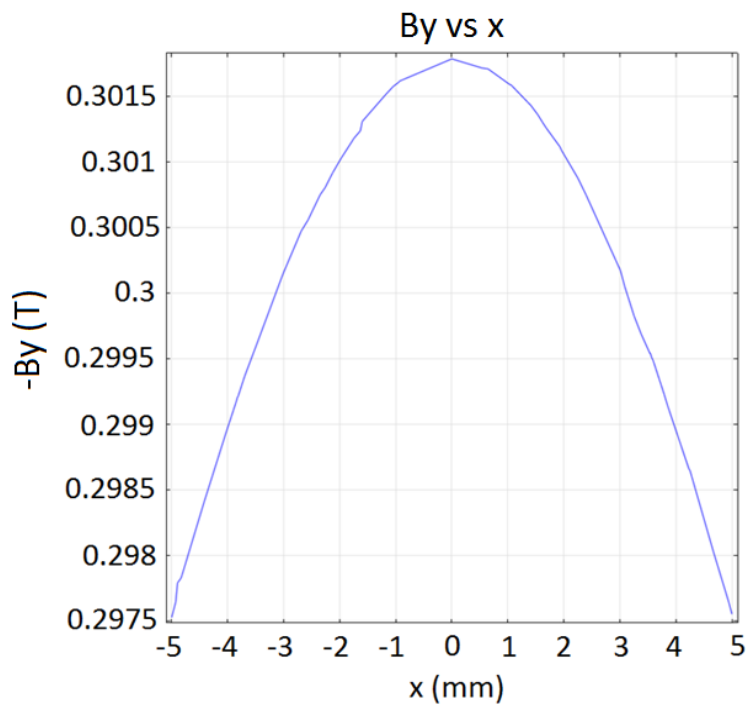


Figure 5-11 - Vertical component of magnetic field in the gap along X

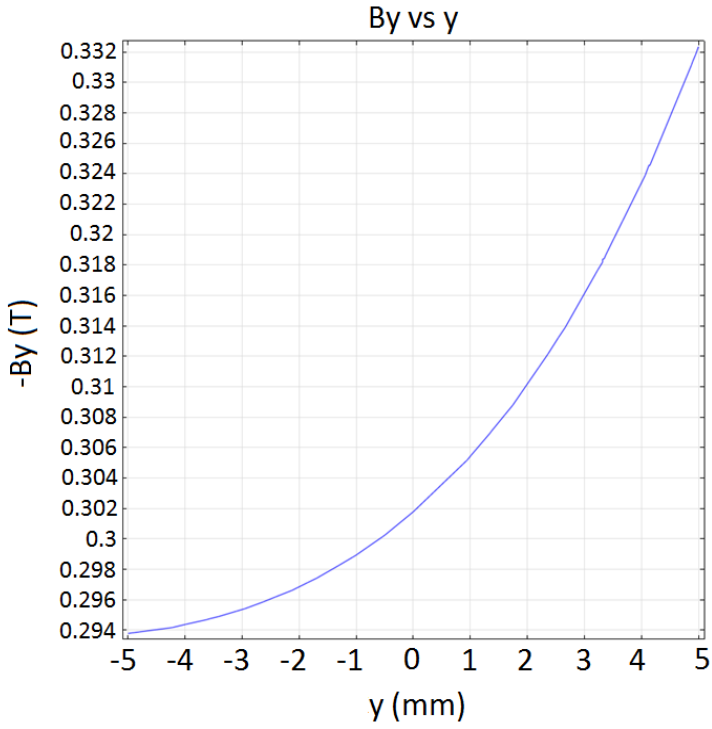


Figure 5-12 - Vertical component of magnetic field in the gap along Y

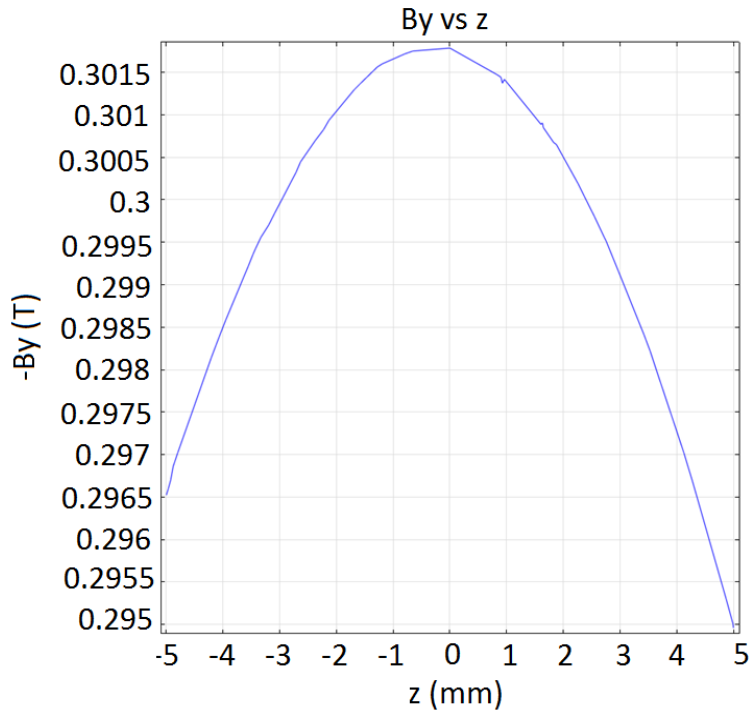


Figure 5-13 - Vertical component of magnetic field in the gap along Z

If the entire socket assembly moves, so that the steel disc moves with the sensor, the variation in the magnetic field at the sensor location is even less, less than 0.2 mT over 1 mm in X and Z, and 1 mT over 1 mm in Y. Figure 5-14, Figure 5-15, and Figure 5-16 show the strength of the vertical component of the magnetic field at the sensor location for different socket positions in X, Y, and Z respectively. Note again that the Y direction is vertical.

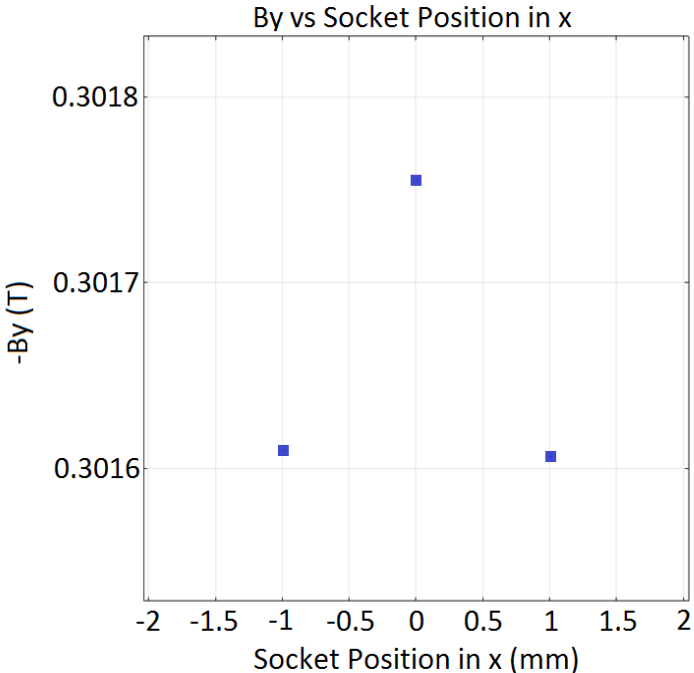


Figure 5-14 - Vertical component of magnetic field at the sensor location for different socket positions in X

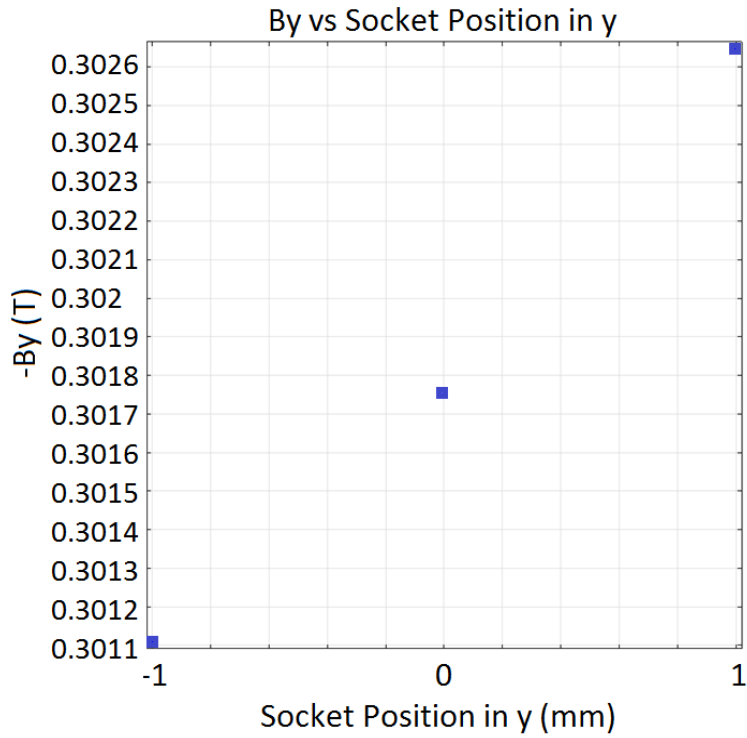


Figure 5-15 - Vertical component of magnetic field at the sensor location for different socket positions in Y

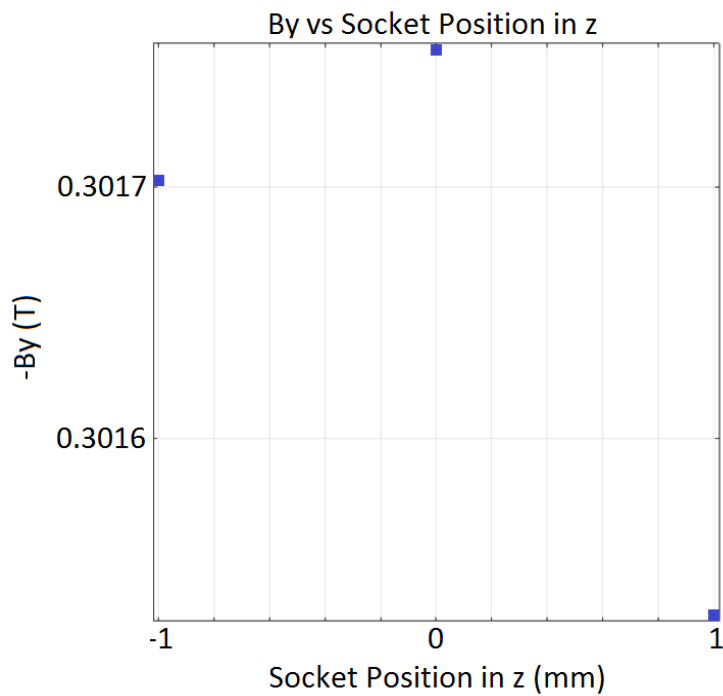


Figure 5-16 - Vertical component of magnetic field at the sensor location for different socket positions in Z

5.4.2 Assembly

Steel yokes and aluminum parts were machined prior to assembly of the magnetic circuit. Shown in Figure 5-17 are the steel yokes and the aluminum receptacle, support, moving blocks, and back plate.

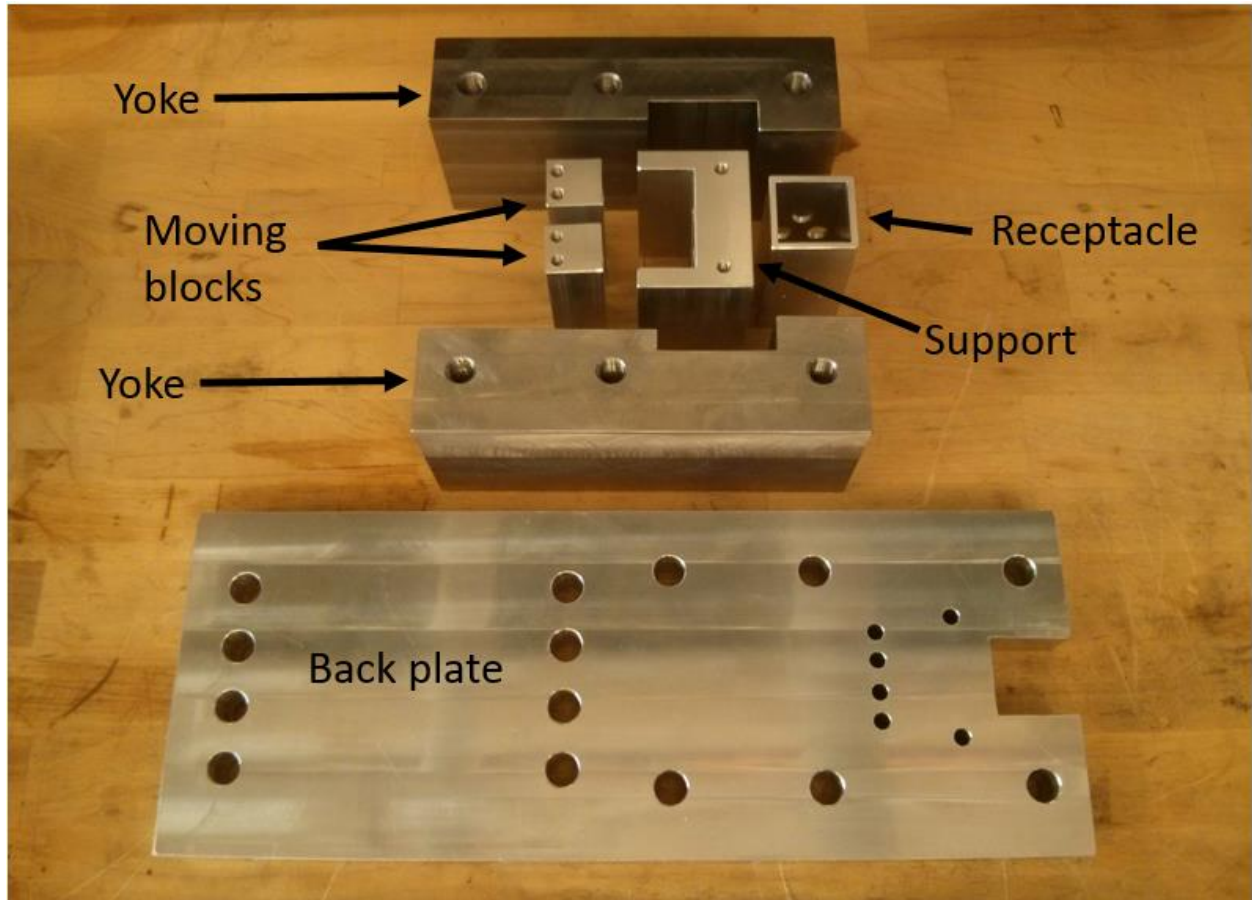


Figure 5-17 - Machined components for magnetic field source

Figure 5-18 shows the magnetic circuit assembly prior to inserting the magnets.

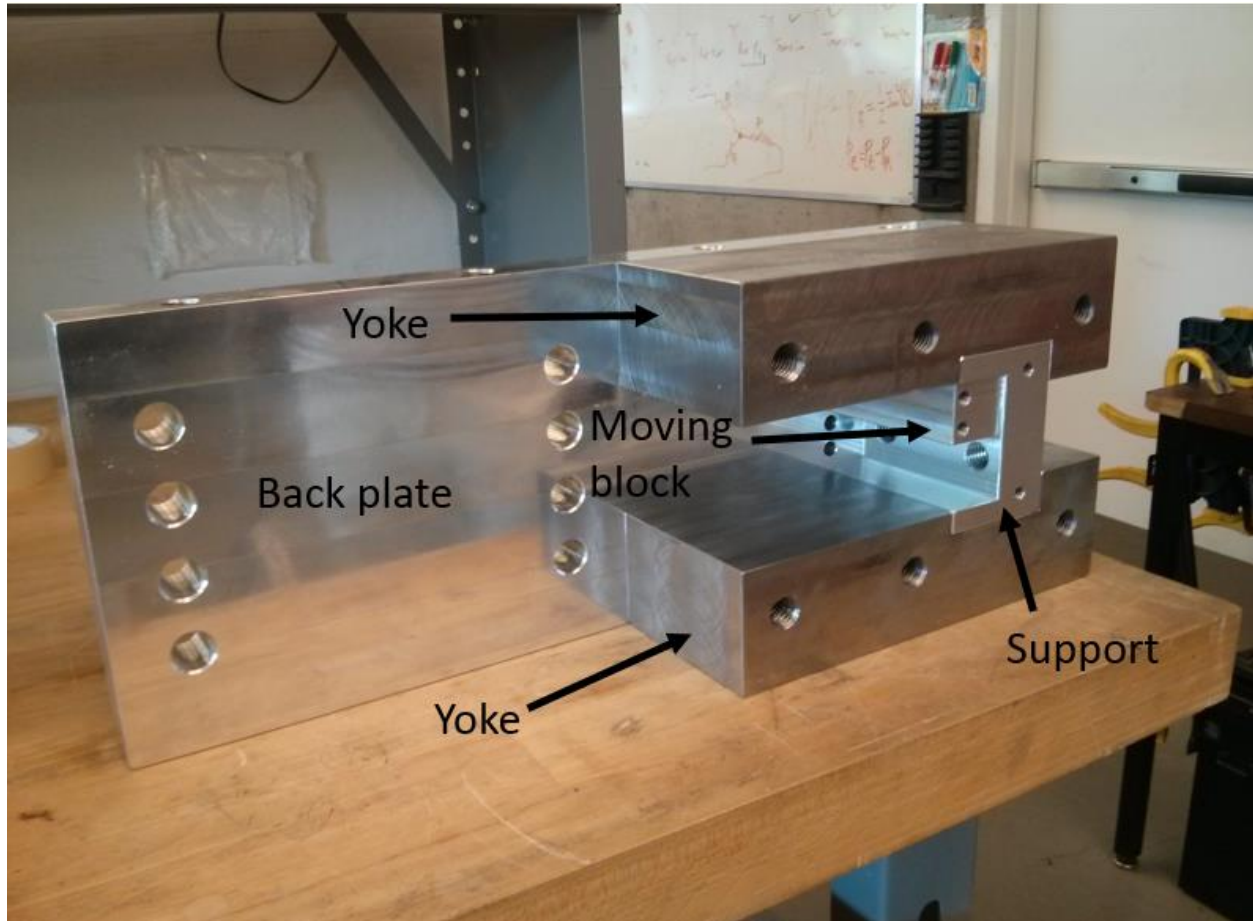


Figure 5-18 - Magnetic field source prior to inserting magnets

The steel yokes are fastened to the back plate to hold them in place. There is an attraction force between them once the magnets are inserted. The aluminum support also helps support the yokes and acts as a nut for the threaded rods (not shown).

The magnets were slid into place using temporary wooden guides clamped to the aluminum back plate, as shown in Figure 5-19.



Figure 5-19 - Temporary wooden guides for inserting the magnets into the magnetic field source

There is a strong attraction force for the magnet to enter the magnet assembly. The moving block acts as a restraint for the magnet and is slowly backed up using threaded rods, as shown in Figure 5-20.

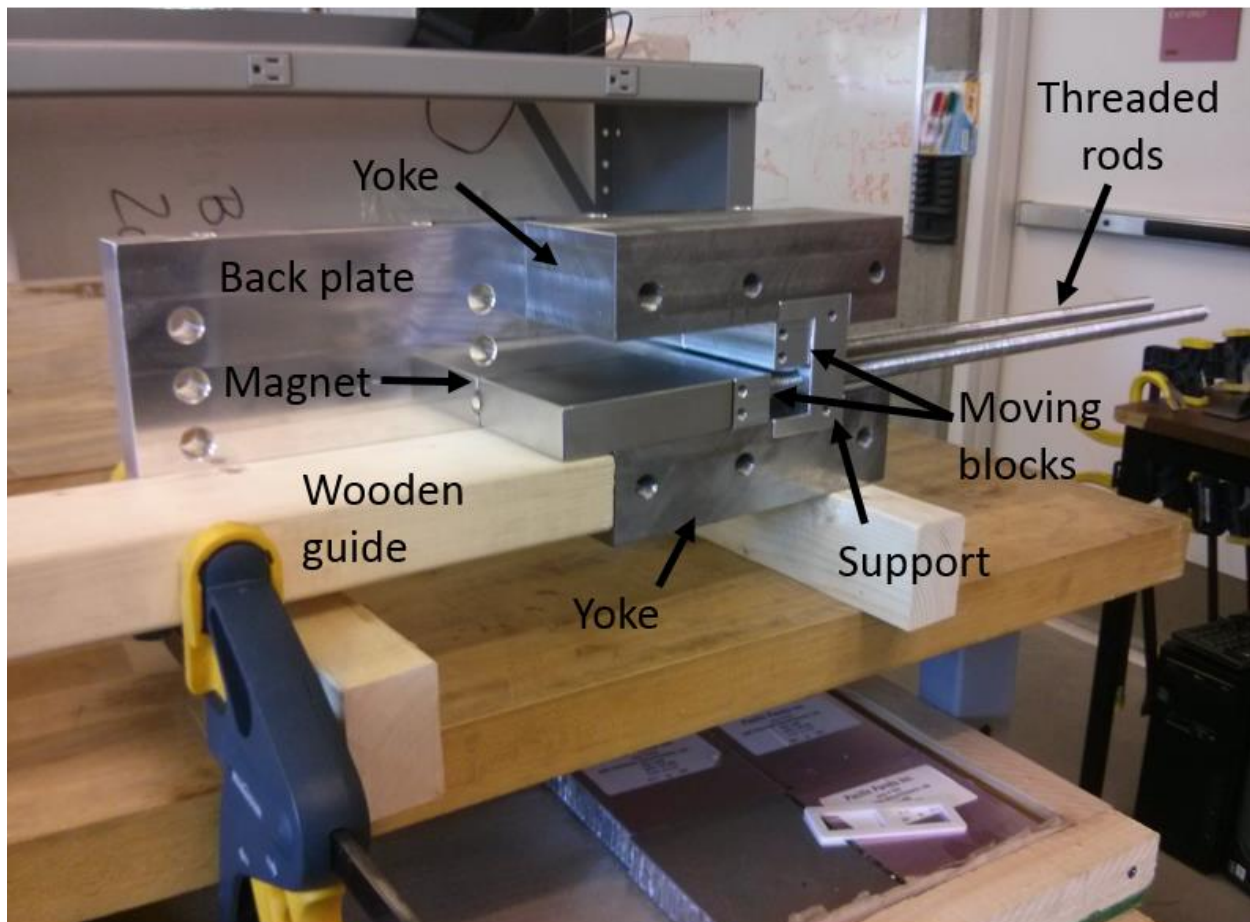


Figure 5-20 - First magnet approaching the final resting place

Brass balls are used inside a blind hole for the contact between the moving block and threaded rod. As the magnet approached its final position, the normal force between the magnet and steel yoke increased and the resulting friction meant a rubber hammer was needed to continue moving the magnet. Once the magnet was in place, the moving block was bolted into place as it was also used as a spacer to maintain the position of the magnet.

Wooden guides were used for inserting the second magnet after the first magnet was positioned, as shown in Figure 5-21. A second moving block was used to guide the magnet in, similar to the first magnet.

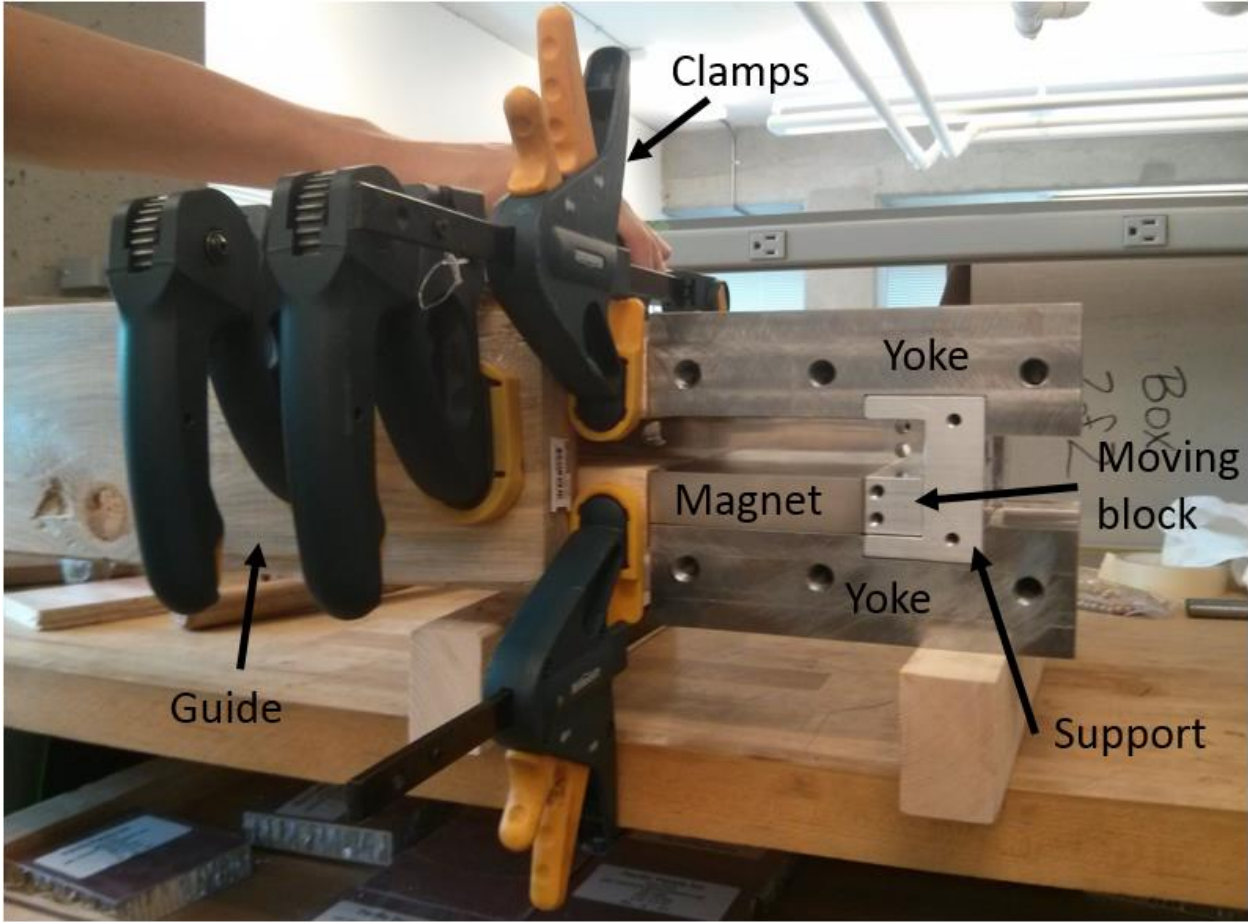


Figure 5-21 - Wooden guides in place for second magnet insertion

Once the second magnet was inserted, the second moving block was fastened into place and the threaded rods and brass balls removed. The fasteners for the steel yokes were temporarily loosened to allow the steel yokes to clamp to the magnets. Figure 5-22 shows the magnetic circuit after insertion of the magnets and prior to insertion of the receptacle. The receptacle was inserted and epoxied to maintain the position.

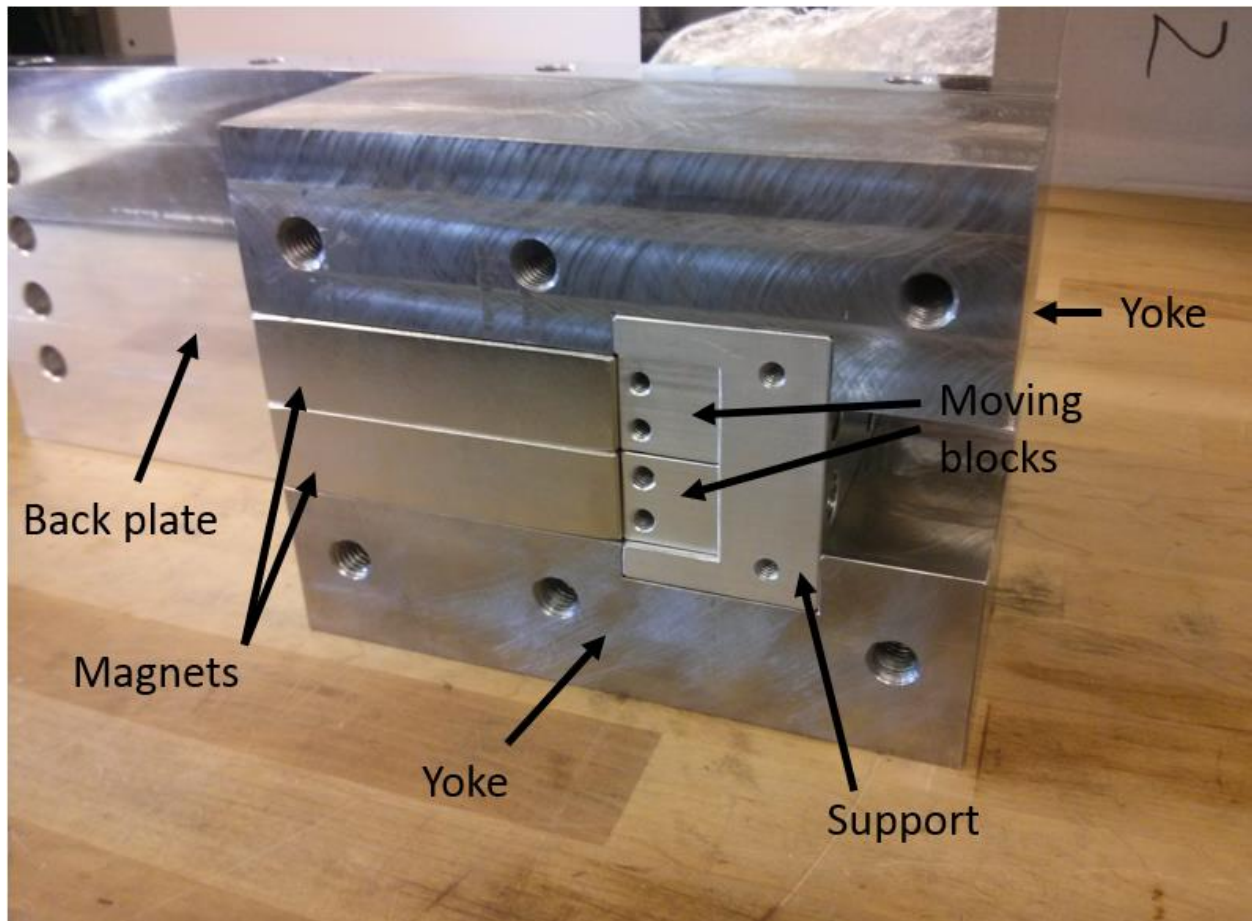


Figure 5-22 - Magnets fully inserted into the magnetic field source

5.5 Kinematic Coupling

The position of the sensor in the magnetic field needs to be repeatable, in case the actual magnetic field is not as uniform as designed. A kinematic coupling using three balls in three vee grooves is a minimum constraint design that is very repeatable.

Initially the grooves were placed on the bottom of the PCB base and the ceramic balls placed in an equilateral triangle in the aluminum housing, as shown in Figure 5-23.

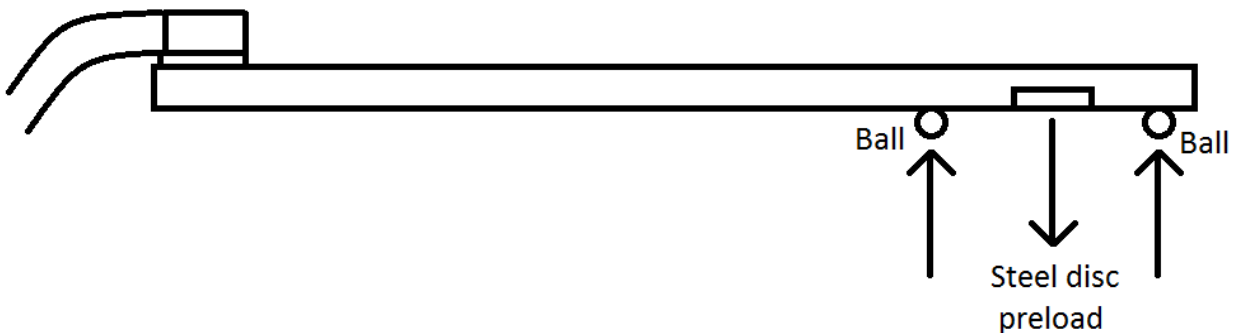


Figure 5-23 - Original kinematic coupling geometry, using magnetic attraction of steel disc for preload

A preload was obtained by inserting a steel disc in the PCB base below the centre of the sensor. Because the magnetic field varies slightly with vertical position, there is a net force downwards on the steel disc.

However, this turned out to be too close together such that the PCB base would not stay seated; the weight of the base and the cables tipped the base off the coupling. To fix this, the forward groove was moved to an aluminum block farther away from the other two grooves, and the ball placed on the top of the base, such that gravity provided the preload, as shown in Figure 5-24.

The steel disc was retained for the benefit mentioned in Section 5.4.1 regarding magnetic field uniformity.

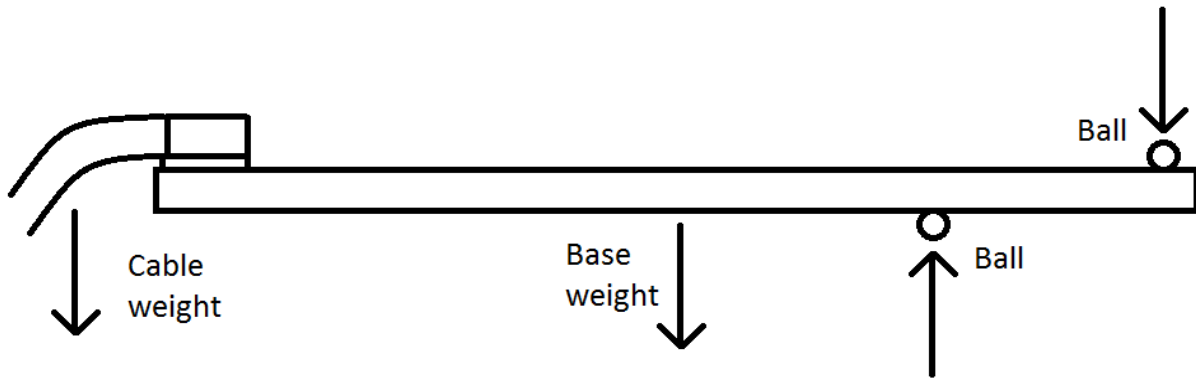


Figure 5-24 - Improved kinematic coupling geometry, using gravity for preload

Figure 5-25 is a bottom view of the PCB assembly showing vee grooves #1 and #2 and the steel disc in the PCB base. Figure 5-26 is a side view of the PCB base showing ball #3 and groove #1 for the kinematic coupling. Figure 5-27 shows inverted vee groove #3 and balls #1 and #2 for the kinematic coupling inside the receptacle. Balls #1, #2, and #3 mate with vee grooves #1, #2, and #3 respectively. Figure 5-28 shows the PCB assembly inserted into the aluminum receptacle.

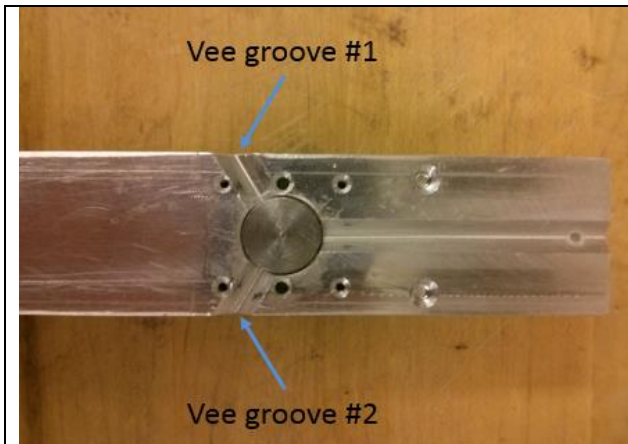


Figure 5-25 - Bottom view of PCB assembly showing vee grooves and steel disc in PCB base



Figure 5-26 - Side view of PCB base showing ball and grooves for kinematic coupling

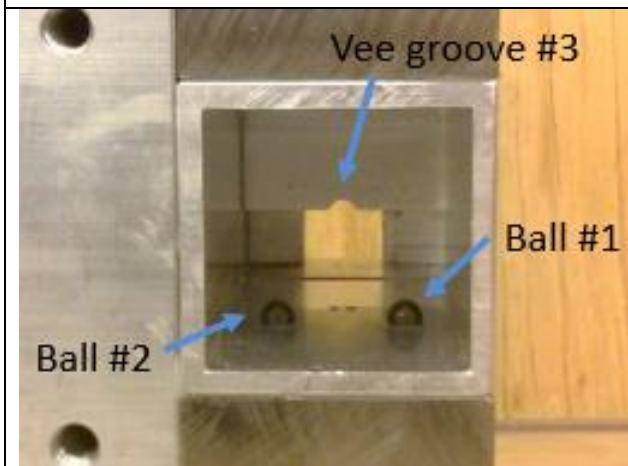


Figure 5-27 - Inverted vee groove and two balls for kinematic coupling inside receptacle



Figure 5-28 - PCB assembly inserted into aluminum receptacle

5.6 Software

Displaying the sensor output can be done on an oscilloscope, but dSPACE was utilized so that the output could be more intuitively displayed for easy sorting. As well, the reference sensor was sampled as a check to ensure the kinematic coupling mated properly, as described in Section 5.2.

The GUI was implemented with ControlDesk and the software designed with Simulink and Stateflow.

5.7 Work Flow

The user inserts a sensor into the socket with plastic tweezers. The PCB is placed into the zero magnetic field, and a button pressed to sample the value. If the reference signal is incorrect or the sensor output excessive, an error message is displayed and the value not recorded. If the correct value is recorded, the user is prompted to insert the sensor into the magnetic field and sample the value. Once again, if the reference signal is incorrect, an error message is displayed and the value not recorded. The difference between the two measurements is calculated and the corresponding bin ID is displayed. The possible bins are positioned sequentially in a row with a coloured label ID. The colouring makes it faster for the user to differentiate between the different bins. The sensor bins were divided into 0.5% groups.

The work station layout for sensor sorting is depicted in Figure 5-29.

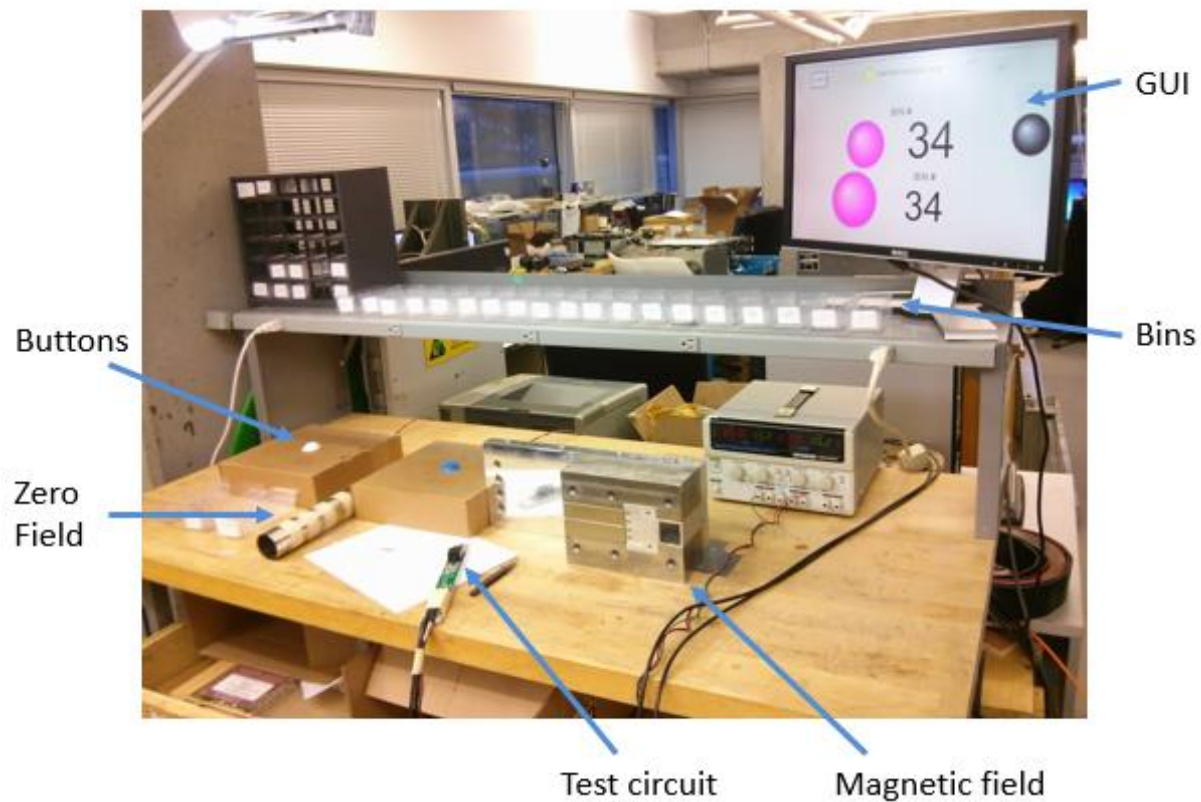


Figure 5-29 - Work station layout for sensor sorting

5.8 Results

The sensors have a uniform gain of $\pm 0.25\%$ plus the repeatability error shown in Section 5.8.1.

A Hall sensor array made with these uniform, sorted sensors will have minimal position error due to gain error, similar to the prototype results in this thesis.

The sensor sorting can be as fast as 20 seconds per sensor, with 25 seconds per sensor being an approximate average time. 12,700 sensors were sorted in less than 3 weeks.

The spring pins in the socket wear over time and need to be replaced. If dust or dirt gets inside the socket, or the sensor is not inserted properly, the spring pins can be damaged. A clean environment and careful insertion can avoid this problem. Should automation of the sensor sorting method be implemented, automatic insertion of a sensor could be checked with optical inspection.

The gains for sensors on the same reel vary about 8%. The gains for sensors on different reels have more variation, up to 12%. It is expected that sensors from the same production batch have similar gains. It may be possible to keep sensors from the same batch grouped so they do not need to be sorted.

5.8.1 Repeatability

A bin of sensors was resampled to check the repeatability and to assess the likelihood of any errors, especially human error. The results are in Table 5-1, which shows the quantity of sensors that changed bins, and by what percentage gain.

Table 5-1 - Results of repeatability test for sensor sorting

Change in Gain	Quantity of Sensors
-1%	1
-0.5%	144
0%	588
+0.5%	66

Two sensors were measured multiple times at different times of day on different days. The sensor voltage and reference sensor voltage changed together, which shows that it was likely not the sensors that changed. A likely possibility is the magnetic field strength changed with temperature. The sensor voltage changed less than 0.4%. This explains why the gain for some of the re-sorted sensors changed between 0.5% bins. The voltage difference for the two sensors, A and B, are plotted versus time in Figure 5-30 and Figure 5-32 respectively. Voltage difference is the difference between the voltages in the two magnetic fields. The reference sensor voltage measured simultaneously with sensor A and B voltage difference measurements is plotted in Figure 5-31 and Figure 5-33 respectively.

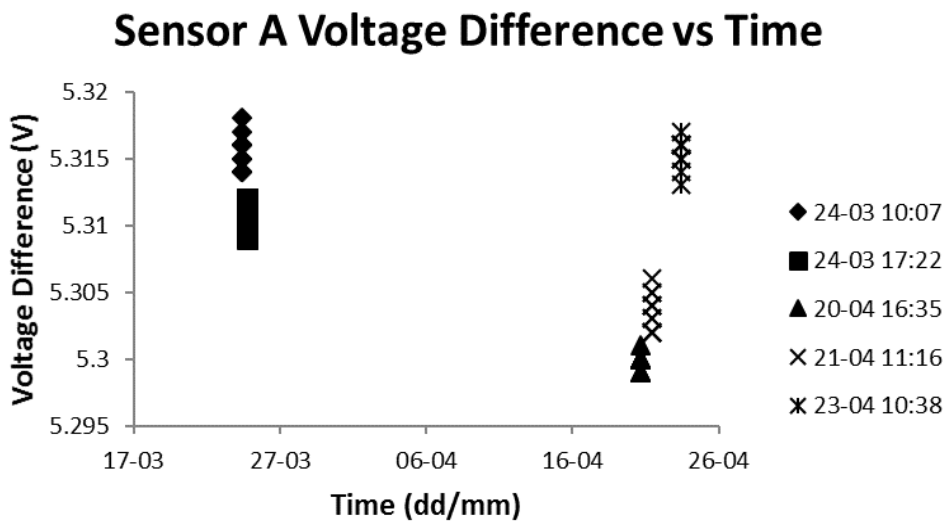


Figure 5-30 - Sensor A voltage difference measured at different times

Reference Sensor Voltage vs Time

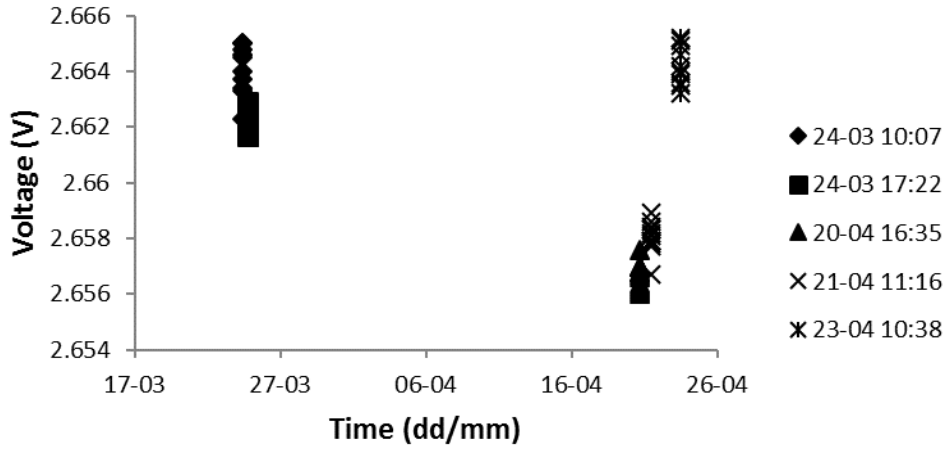


Figure 5-31 - Reference sensor voltage measured simultaneously with sensor A voltage

Sensor B Voltage Difference vs Time

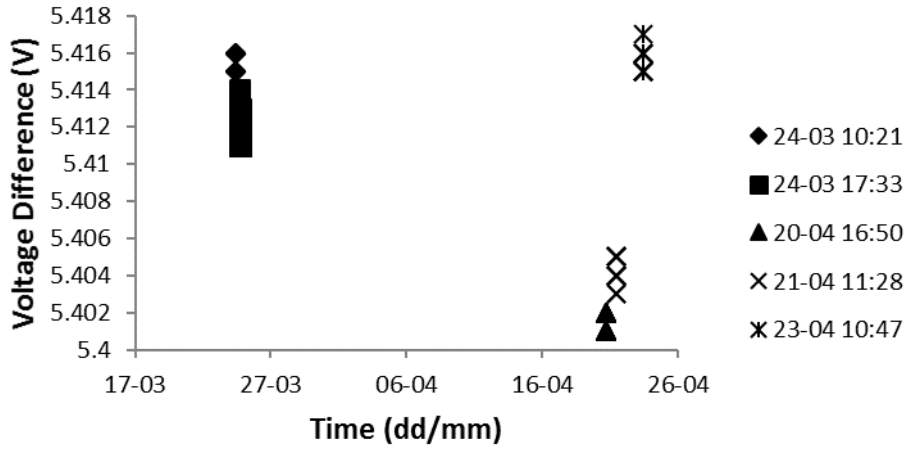


Figure 5-32 - Sensor B voltage difference measured at different times

Reference Sensor Voltage vs Time

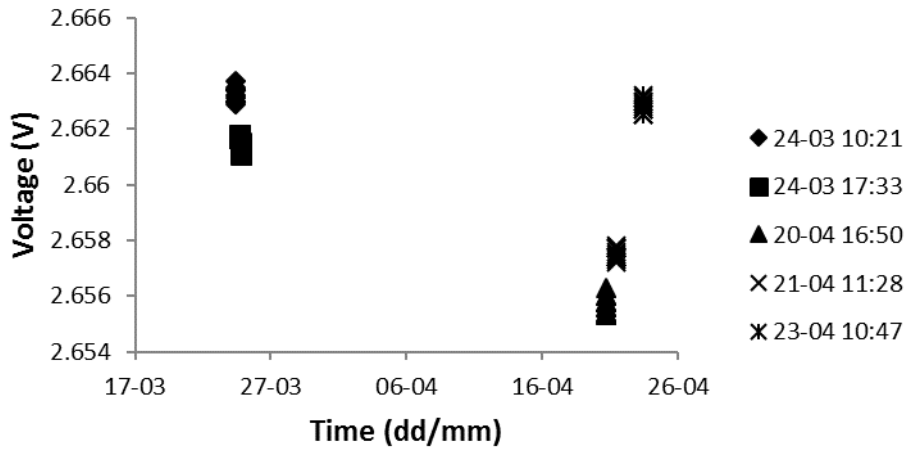


Figure 5-33 - Reference sensor voltage measured simultaneously with sensor B voltage

Chapter 6: Conclusions

This thesis presents the development and verification of a multi-degree of freedom (DOF), non-contact position sensor for a magnetically levitated planar motor. The position sensor consists of a 2-D Hall sensor array to sense 2-DOF for orthogonal 1-D Halbach magnet arrays simultaneously, and thus 6-DOF for a planar motor mover consisting of four Halbach arrays.

This thesis began by introducing planar motor technology, the planar motor of interest for this position sensor, existing sensor solutions, and the motivation for a new position sensor.

The sensor principle was described. There are three sensors per wavelength of the magnetic field, which decouples the sensor outputs for orthogonal magnet arrays. This is done by cancelling the X or Y directional fundamental Z component of the magnetic field when the sensor outputs are summed along the same direction. The calculation of X and Z position, and insensitivity to the Y position, for an X-oriented 1-D Halbach array is presented. The position in 6-DOF can be calculated for a mover composed of four orthogonal 1-D Halbach arrays. Sources of error and the effect on position were identified and examined, including magnetic interference from the stator, magnetic field temperature dependence, and gain error.

A prototype sensor array was designed with Analog Devices AD22151 Hall sensors. The Hall sensors, summing amplifiers, signal processing electronics, and key aspects of the PCB layout were described.

The setup and results of an experiment with the prototype were presented. The prototype was tested using a CNC to move the magnet array to discrete points. Position error above 4 mm

flying height is approximately 200 μm peak to peak. The repeatability is shown to be less than 5 μm , which means the periodic error is systemic and can be compensated. Position resolution is 5 μm . With a magnet array present, the decoupled sensor row output is less than 1% of the voltage range. Due to redundancy and averaging, improved accuracy and resolution is expected for 6-DOF sensing of the planar motor mover.

Lastly, the design and assembly of a sensor sorting set up was presented, including PCB, kinematic coupling, magnetic field, zero field, and software. The repeatability of the process was also demonstrated. This was used to sort 12,700 compact sensors based on gain, at an average speed of 25 seconds per sensor. The result is the ability to make a sensor array with uniform sensor gain for micrometre-level accuracy, especially useful when sensor outputs are summed in hardware and calibration is not easy. Variation in sensor gain is a common cause of position error in past Hall sensor arrays for planar motors. Previous Hall sensor arrays have only achieved good accuracy by using laser interferometers for error mapping or individual differential amplifiers to control each sensor's gain. The experiment results for the Hall sensor array prototype in this thesis demonstrate the reduced error achievable with uniform gain.

The sensor requirements which have been achieved are summarized in Table 6-1.

Table 6-1 - Requirements achieved

#	Requirement	Achieved?
1.	Non-contact	Yes
2.	6-DOF capable	Yes, but not tested
3.	Absolute measurement	Yes
4.	Metre-level range in X and Y range	Theoretically possible in X and Y
5.	10 mm range in Z	Prototype limited by sensor magnetic range in Z, but higher range sensors available
6.	Sense multiple movers	Possible if sensors not summed in hardware
7.	Require no unobstructed space overhead	Yes
8.	Require no power or communications supplied to the mover	Yes
9.	High bandwidth, several kHz	Yes, 5.7 kHz
10.	No performance degradation at high speed/acceleration (m/s, dozens of m/s ²)	Not tested, future work
11.	Cost-effective	Yes, but increases with area
12.	Micrometre-level resolution and error, or better	5 μm resolution. 200 μm error peak-to-peak. 5 μm repeatability, hence error is systemic and can be calibrated. Better accuracy expected for mover due to averaging and redundancy.

The presented Hall sensor array has been shown to be a good choice for applications requiring a cost-effective, compact, absolute sensor with long range and micrometre accuracy. The results are promising for many manufacturing applications, including assembly, conveying, and

machining. For high precision applications, the Hall sensor array can be used as a back-up sensor in case laser interferometers or other higher precision sensors fail. As well, the Hall sensor array can be used for positioning movers over a long stroke between work stations where a higher precision sensor is located. In addition to planar motor position sensing, the sensor principle could be applied to position sensing of other actuator types using Halbach arrays or other periodic magnet arrays.

6.1 Future Work

Future work includes a larger Hall sensor array for integration with the stator for longer stroke measurement, which can use more compact, lower cost sensors than the AD22151. Six degree of freedom position sensing and control with the Hall sensor array needs to be tested, including the characterization of the sensor with a dynamic mover. Work is required on calibrating or reducing the repeatable and systemic position error, which is likely due to fabrication error of the magnet array and variation in the magnetic field strength.

Bibliography

- [1] X. Lu and I.-u.-r. Usman, "6D direct-drive technology for planar motion stages," *CIRP Annals - Manufacturing Technology*, no. 61, pp. 359-362, 2012.
- [2] X. Lu and I.-U.-R. Usman, "Displacement devices and methods for fabrication, use and control of same". United States of America Patent US2014/0285122 A1, 25 September 2014.
- [3] W.-j. Kim and D. L. Trumper, "High-precision magnetic levitation stage for photolithography," *Precision Engineering*, vol. 22, no. 2, pp. 66-77, 1998.
- [4] M. Holmes, R. Hocken and D. Trumper, "The long-range scanning stage: a novel platform for scanned-probe microscopy," *Journal of the International Societies for Precision Engineering and Nanotechnology*, vol. 24, no. 3, pp. 191-209, 2000.
- [5] X. Shan, S.-K. Kuo, J. Zhang and C.-H. Menq, "Ultra precision motion control of a multiple degrees of freedom magnetic suspension stage," *IEEE/ASME Transactions on Mechatronics*, vol. 7, no. 1, pp. 67-78, 2002.
- [6] K. S. Jung and Y. S. Baek, "Precision stage using a non-contact planar actuator based on magnetic suspension technology," *Mechatronics*, vol. 13, no. 8, pp. 981-999, 2003.
- [7] W.-J. Kim, N. Bhat and T. Hu, "Integrated multidimensional positioner for precision manufacturing," in *Proceedings of the Institution of Mechanical Engineers, Part B: Journal of Engineering Manufacture*, 2004.
- [8] Z. Zhang and C.-H. Menq, "Laser interferometric system for six-axis motion measurement," *Review of Scientific Instruments*, vol. 78, no. 8, p. 083107, 2007.
- [9] W. Gao, S. Dejima, H. Yanai, K. Katakura, S. Kiyono and Y. Tomita, "A surface motor-driven planar motion stage integrated with an XYθZ surface encoder for precision positioning," *Precision Engineering*, vol. 28, no. 3, pp. 329-337, 2004.
- [10] A. Kimura, W. Gao, W. Kim, K. Hosono, Y. Shimizu, L. Shi and L. Zeng, "A sub-nanometric three-axis surface encoder with short-period planar gratings for stage motion measurement," vol. 36, no. 4, pp. 576-585, 2012.
- [11] W. Gao, S. Dejima, Y. Shimizu, S. Kiyono and H. & Yoshikawa, "Precision measurement of two-axis positions and tilt motions using a surface encoder," *CIRP Annals-Manufacturing Technology*, vol. 52,

no. 1, pp. 435-438, 2003.

- [12] X. Li, W. Gao, H. Muto, Y. Shimizu, S. Ito and S. Dian, "A six-degree-of-freedom surface encoder for precision positioning of a planar motion stage," *Precision Engineering*, vol. 37, no. 3, pp. 771-781, 2013.
- [13] T. Castenmiller, F. van de Mast, T. de Kort, C. van de Vin, M. de Wit, R. Stegen and S. van Cleef, "Towards ultimate optical lithography with NXT: 1950i dual stage immersion platform," in *Proc. SPIE 7640, Optical Microlithography XXIII*, 2010.
- [14] X. Li, Y. Shimizu, S. Ito and W. Gao, "Fabrication of scale gratings for surface encoders by using laser interference lithography with 405 nm laser diodes," *International Journal of Precision Engineering and Manufacturing*, vol. 14, no. 11, pp. 1979-1988, 2013.
- [15] D. B. Leviton, J. Kirk and L. Lobsinger, "Ultra-high resolution Cartesian absolute optical encoder," in *Proc. SPIE 5190, Recent Developments in Traceable Dimensional Measurements II*, 2003.
- [16] P. S. Huang, T. Kai and X. Qiang, "An active encoder for precision position measurement," in *ASPE Annual Meeting Proceedings*, 2013.
- [17] J. Gao and P. S. Huang, "A planar motor with an active encoder," in *ASPE Annual Meeting Proceedings*, 2013.
- [18] M. Bonse, F. Zhu and J. Spronck, "A new two-dimensional capacitive position transducer," *Sensors and Actuators A: Physical*, vol. 41, no. 1, pp. 29-32, 1994.
- [19] H. Furuichi and R. S. Fearing, "A planar capacitive micro positioning sensor," in *Micro Machine and Human Science, 1996., Proceedings of the Seventh International Symposium*, 1996.
- [20] P. W. Kolb, R. S. Decca and H. D. Drew, "Capacitive sensor for micropositioning in two dimensions," *Review of Scientific Instruments*, vol. 69, no. 1, pp. 310-312, 1998.
- [21] J.-p. Yu, W. Wang, K.-q. Lu, D.-q. Mei and Z.-c. Chen, "A planar capacitive sensor for 2D long-range displacement measurement," *Journal of Zhejiang University SCIENCE C*, vol. 14, no. 4, pp. 252-257, 2013.
- [22] H.-J. Ahn, J.-H. Park, C.-Y. Um and D.-C. Han, "A disk-type capacitive sensor for five-dimensional motion measurements," *Measurement Science and Technology*, vol. 19, no. 4, p. 045202, 2008.
- [23] X. Lu, N. Rao and I.-u.-r. Usman, "Six-axis position measurement system for levitated motion stages," *CIRP Annals - Manufacturing Technology*, no. 62, pp. 507-510, 2013.

- [24] P. C. M. Frissen, J. C. Compter, M. J. M. Renkens, G. A. J. De Fockert and R. J. M. Coolen, "Displacement Device". United States of America Patent US 2004/0017116 A1, 29 January 2004.
- [25] J. C. Compter, "Electro-dynamic planar motor," *Precision Engineering*, pp. 171-180, 2004.
- [26] Y. Kawato and W.-j. Kim, "Multi-degree-of-freedom precision position sensing and motion control using two-axis Hall-effect sensors," *Journal of Dynamic Systems, Measurement, and Control*, pp. 980-988, 2006.
- [27] H.-J. Ahn, "Apparatus for Measuring Displacement". United States of America Patent 2014/0285184 A1, 2014.
- [28] H. J. Ahn and K. R. Kim, "2D Hall sensor array for measuring the position of a magnet matrix," *International Journal Of Precision Engineering And Manufacturing-Green Technology*, vol. 1, no. 2, pp. 125-129, 2014.
- [29] D. L. Trumper, M. E. Williams and T. H. Nguyen, "Magnet arrays for synchronous machines," in *Conference Record of the 1993 IEEE Industry Applications Conference Twenty-Eighth IAS Annual Meeting*, 1993.
- [30] I.-U.-R. Usman and X. Lu, "Force ripple attenuation of 6-DOF direct drive permanent magnet planar levitating synchronous motors," *IEEE Transactions on Magnetics*, 2015.
- [31] Arnold Magnetic Technologies, [Online]. Available: www.arnoldmagnetics.com/WorkArea/DownloadAsset.aspx?id=5049. [Accessed 17 August 2015].
- [32] Analog Devices, "Linear Output Magnetic Field Sensor - AD22151," 2003.
- [33] D. C. Meeker, *Finite Element Method Magnetics*, 4.2 ed., 2013.
- [34] M. COMSOL, *AC/DC Module; Version 4.3b (x64 Build)*, COMSOL, 2013.
- [35] Y. Kawato and W.-j. Kim, "A novel multi-DOF precision positioning methodology using two-axis Hall-effect sensors," in *American Control Conference*, Portland, OR, USA, 2005.